Growth, Structure And Physical Properties Of Strained $NdNiO_3$ Films

Thesis submitted for the degree of

Doctor of Philosophy (Science)

in

Physics (Experimental)

by

PARUSHOTTAM MAJHI

Department of Physics

University of Calcutta

2023

Growth, Structure And Physical Properties Of Strained $NdNiO_3$ Films

Abstract

In this thesis we have investigated a selected range of physical properties in films of correlated oxide $NdNiO_3$ that undergo metal-insulator (M-I) transition from a high temperature metallic phase to a low temperature insulating phase. The transition though has different features, is close to a temperature driven Mott type transition, which is a first order transition. The MI transition, being first order shows an important aspect that there are co-existing phases as established by the spatially resolved imaging techniques. The co-existing phases are the high temperature metallic phases and low temperature insulating phases. The existence of such phases shows up in a number of physical properties which in turn can be tuned by strains in films or residual strains and quenched disorder has happens when the strain is relaxed. In general, the NiO_6 octahedra in $NdNiO_3$ controls the physical properties, like the electrical transport, through the packing of the NiO_6 octahedron.

The films investigated were grown by Pulsed Laser Deposition (PLD) technique on various crystalline substrates with different lattice constants in order to vary the extent of strain and strain related issues.The films were grown on $SrTiO_3$, $LaAlO_3$ and $BaTiO_3$. The films grown were characterized by a number of techniques. In the thesis we investigated the following specific issues.

We have made an important observation that there is onset of electronic Griffiths phase in $NdNiO_3$ film grown on $BaTiO_3/SrTiO_3$ with quenched disorder. The Griffith phase occurs as a consequence of Mott transition in disordered system. It is an electronic state with slow dynamics that near or above the transition region. Using noise and impedance spectroscopes, we found a characteristic temperature $T_G \approx 230K$ well above $T_{MI}(= 160K)$ where large low-frequency correlated fluctuations appear, signifying the appearance of Griffiths phase with slow dynamics. This is noted as a first observation of such a phase in a correlated oxide.

In $NdNiO_3$, co-existing phases near and below the MI transition leads to hysteretic resistivity vs temperature curves, when the samples are cycled through the metal-insulator at a fixed ramp rate. The investigation was carried out with precisely controlled thermal program that consists of uniform cooling/heating rates varying from 0.2 K/min to 15 K/min in the temperature range 9K to 300K.

Also, in the context of co-existing mixed phases (metal and insulator) it has been observed that below the transition temperature (T_{MI}) there is a finite time of kinetics of transformation of the metastable high temperature phase to the low temperature insulating phase. We have used resistivity measurement as a tool to study relaxation where the relative change in metallic and insulating volume fraction was obtained from the resistivity data using effective medium theory. The kinetics of relaxation was studied by isothermal annealing below T_{MI}. The average relaxation time, obtained from the isothermal annealing experiment ($< \tau >$), decreases on cooling, contrary to the expectation of relaxation through a fixed barrier. This can happen when the barrier to relaxation/transformation changes with temperature. This leads to identification of a temperature T^* as the limit of metastability for supercooled metallic phase where $< \tau > \rightarrow 0$.
One novel experiment was carried out where the $NdNiO_3$ film was strained reversibly by an electric bias applied on a piezo-electric substrate (like $BaTiO_3$) on which the film is grown. The bias generated strain although by a small adds a new dimension because the strain and allied issues are fixed when the film is grown on a substrate with lattice mismatch. The reversible voltage-controlled strain can tune the physical properties like resistivities and the transition temperature (T_{MI}) in the $NdNiO_3$ film. The bias-controlled strain adds incrementally to the existing strain level. The strain so generated was measured by performing X-Ray diffraction on the $NdNiO_3$ film with a bias applied on the substrate. Shift in the diffraction pattern (i.e., the diffraction line) gives an absolute measure of the strain in the film.
In summary, the main observations of the thesis are - (a) emergence of slow kinetics and electronic Griffiths like phase close to the metal-insulator transition temperature (T_{MI}), a new observation (b) kinetics of resistivity relaxation as well as hysteresis on temperature cycling, occurring below T_{MI} and signature of supercooling nature of on metallic phases and (c) resistivity and T_{MI} tuning with piezo-straining effect in context of crystallographic parameters like disorder, grain, strain etc.

Dedicated to My Baba & Maa

Acknowledgements

I would like to express my sincere gratitude to my supervisors Prof. Arup Kumar Raychaudhuri & Dr. Barnali Ghosh(saha) for their constant guidance and help in all aspects of the thesis.Their expertise and insights have improved not only myself but also my works. Words will not adequately express my gratitude for their constant support and faith in me.

I received a lot of advice from Dr. R. S. Bisht (Ravi da), who mentored me at the start of my PhD career. I would like to express my gratitude to Dr. Bisht and Mr. Sudipta Chatterjee, Mr. Saikat Mitra who acted as my research partner. I would like to thank Mr. Anirban Goswami, Dr. Subhamita Sengupta and Dr. Ankita Ghatak for their suggestion regarding material growth and characterization.I am grateful to Dr. Raghavendra Reddy, UGC-DAE-CSR Indore for enabling us to use Reciprocal space map (RSM) technique. I thank to Dr. Dipten Bhattacharya, CGCRI-Kolkata for allowing us to utilize the P-E loop measurement set-up. I will cherish the memories with lab seniors Dr. Shaili Sett, Dr. Samik Roy Moulik,Dr. Arnab Ghosh, Dr. Arun Bera, Dr. Mustaque ali khan and my other lab mates Chandan da, Avisek da, Vishal, Snehamoyee, and Saikat.

I appriciate the technical help of Mr. Sohel Siraj in LabView code writing. I admire the technical skills of our S.N. Bose Center's Technical Cell.Special appreciation to Mr. Shaktinath Das for maintaining the Pulsed Laser Deposition equipment and producing high-quality samples, Mr. Sourav Sinha for putting in extra effort to comcplete an HRXRD experiment along with Mrs.Urmi Charkraborty, Mr. Amit Das, Mr. Joy Bandhopadhyay and other technical cell members.

I thankfully acknowledge to my centre S.N. Bose National Centre for Basic sciences (SNBNCBS), DST, GOI for proving me the opportunity to work and the fellowship.

P. Majhi

List of Publications

1. Diffused metal-insulator transition in $NdNiO_3$ film grown on BaTiO3:Likely evidence of electronic Griffiths phase **P. Majhi, S. Chatterjee, R. S. Bisht, V. R. Reddy, B. Ghosh and A. K. Raychaudhuri** *Phys. Rev. Matt.* **5** 085005 (2021).

2. Phase co-existence, super-cooling and resistance relaxation kinetics in $NdNiO_3$ films below the Metal-Insulator Transition Temperature **P. Majhi, S. Mitra, B. Ghosh and A. K. Raychaudhuri** *(Communicated)*

3. Tuning of in-plane resistivity & metal-insulator transition temperature (T_{MI}) using voltage controlled reversible strain on $NdNiO_3$ film **P. Majhi et al.** *(Manuscript under preparation)*

List of Figures

Contents

Chapter 1

Introduction

Abstract:
In this chapter, we discuss the relevant physical features and the electronic properties of the rare earth nickelate system, $NdNiO_3$. We describe the phenomena, the Metal-Inulator (M-I) transition in the presence and effects of such perturbations like strain, strain relaxation and resulting disorder in $NdNiO_3$ thin film. The discussion sets forth the salient features that we need for the present thesis. This has been followed by outline of the thesis. We also have an introductory section in each of the chapters to bring out the important physics.

1.1 Introductory remarks and orientation of the thesis

The underlying physics of oxide perovskite thin film has attracted significant interests of researchers. Extensive research works had been done on electrical and magnetic properties of strained metal oxide films, particularly films of 3d transition metal oxides [1–3]. The specific material that has been investigated in this thesis is $NdNiO_3$ (NNO), which is a correlated oxide perovskite material. Though the material has been investigated by researchers for a long time, still there is no universally accepted coherent explanations that can account for the majority of the observable phenomena like temperature (T) driven Metal-Insulator(MI) transition. MI transition in these oxides have a significant component of Correlation. However, it has not yet been accepted whether the MI transition can be described cleanly by a Mott-Transition or a Charge transfer transition.

The growth of a film on crystalline substrate is significantly impacted by strain that can arise from the lattice match or mismatch between the film and substrate. A film is coherently strained (either compressive or tesnile) by the substrate only when it is very thin. When the thickness (t) of the film deposited is enhanced, the built-in strain is large (grows as $\sim t^2$) it crosses the limit set by the yield strength of the film , leading to strain relaxation that creates dislocations (disorder) that can thread the film and also leads to creation of disorder at the interfacial region that allows for strain relaxation.

The substrate induced strain, influence significantly various properties of transition metal oxide thin films such as structural properties (crystallographic phases), resistance, M-I transition [4], magnetoresistance [5], magnetic transitions and magnetic anisotropy [6], phase eparation [7], charge and orbital ordering [8]. Substrate induced strain arises from mismatch in lattice constants of the films and the substrates and are generally limited to within few percentages. In general, but not necessarily always, the strain changes the metal-oxygen-metal bond angle and packing and shape of the metal -oxygen octahedra that in turn changes the band width of electrons, band gaps and magnetic exchange interactions.

The temperature driven MI transition is a first order transition. Such a transition shows phase-coexistence (electronic phase separation of high temperature metallic phase and low temperature insulating phase). [9]. Presence of strain (both homogeneous and inhomogeneous) and disorder can change the nature of the transition. It can also change the nature and extent of phase-coexistence like kinetics of phase relaxation and even can lead to new phenomena. In this thesis we did look into these issues and added new observations and understanding.

The occurrence of phase-coexistence around the M-I transition in NNO and the associated physics have being studied since long. The thesis deals with the phenomena of phase co-existence of metallic and insulating phases and surrounded physics of NNO thin film. The phase co-existence has an important consequence, in particular, when dynamic aspects and kinetics of co-existing phases are considered around T_{MI}. In the presence of adequate crystal disorder, we have explored the NNO metal-insulator phase transition . We looked at how the texture of NNO films with different grain sizes affected the kinetics of relaxation at low T where we may have persistence of metastable high temperature metallic phase.

In general, the investigations on films with strain of varying degree are carried out by growing them on crystalline substrate of different lattice constants. In this method relative large strain $\leq 3\%$ can be produced. However, the starin is "frozen" at growth and cannot be changed at will in a reversible fashion. If the film is not coherently strained, it can lead to strain relaxation, as mentioned earlier, that leads to inhomogeneous straining. In this thesis we also used a different and unconventional method, that can homogeneously strain a film reversibly by an applied bias. Voltage controlled reversible strain can be produced by growing the film on a piezo-electric crystal/film and applying a bias on the piezo-electric substrate. This limits the extent of straining but the strain produced is homogeneous and reversible.

Physical investigations on strained films is a large topic. In this thesis , we explored a cross-section of the questions that have not been investigated before.

1.2 Introduction to perovskite: Nickelate: $NdNiO_3$

The oxide perovskite is a class of materials that belong to family of oxides with general structural formula ABO_3 where A and B are cations and O is the anion. Another type of Halogen based perovskites, like (ABX_3 (with X= halogen like Cl,Br.I) have also attracted recent attention for energy related applications. The journey of perovskite started with the discovery of $CaTiO_3$ as a mineral in 1839 by G. Rose and it was named after Russian minerologist L. A. Perovski [10]. In the crystal structure of ABO_3 the B site atom is surrounded by six oxygen atom and form the BO_6 octahedra which controls all the physical phenomena associated with it. In general, ideal oxide perovskite is cubic in crystal system where the super exchange angle $B-O-B \approx 180^oC$ and the A site atom is found to be larger compare to B site atom. The $SrTiO_3$ is most common example of ideal cubic perovskite crystal. However, in reality the oxide perovskite observes in orthorhombic or tetragonal form due to the presence of distortion. The main source of distortion in perovskites is tilting or stretching in BO_6 octahedra. The degree of distortion and stability of perovskite phase content can be estimated with the 'Goldschmidt tolerance factor ($\tilde{t}$)' which is expressed by-

$$\tilde{t} = \frac{r_A + r_O}{\sqrt[2]{2}(r_B + r_O)} \tag{1}$$

where r_A, r_B and r_O are the ionic radius of A, B sites atom and oxygen atom respectively. For stability the typical values of $\tilde{t}$ ranges between 0.75 to 1.

The rare earth nickelate ($RNiO_3$) oxide perovskite is interesting due to its fascinating structural, electronic and temperature or pressure driven M-I transition phenomena.Nickelate was synthesized in 1971 [11], the earlier works on nickelates mainly based on bulk material then people have explored gradually the origin of M-I transition and its tuning with rare earth cationic size [11, 13–16, 23]. The nickelate with series of rare earth ions like R = La, Pr, Nd, Sm, Eu show the MIT phenomena except $LaNiO_3$ which is metallic. A schematic

diagram of unit cell of nickelate with the NiO_6 and $< Ni - O_2 - Ni$, $< Ni - O_2 - Ni$ angle are shown in Fig. 1.1 [12].

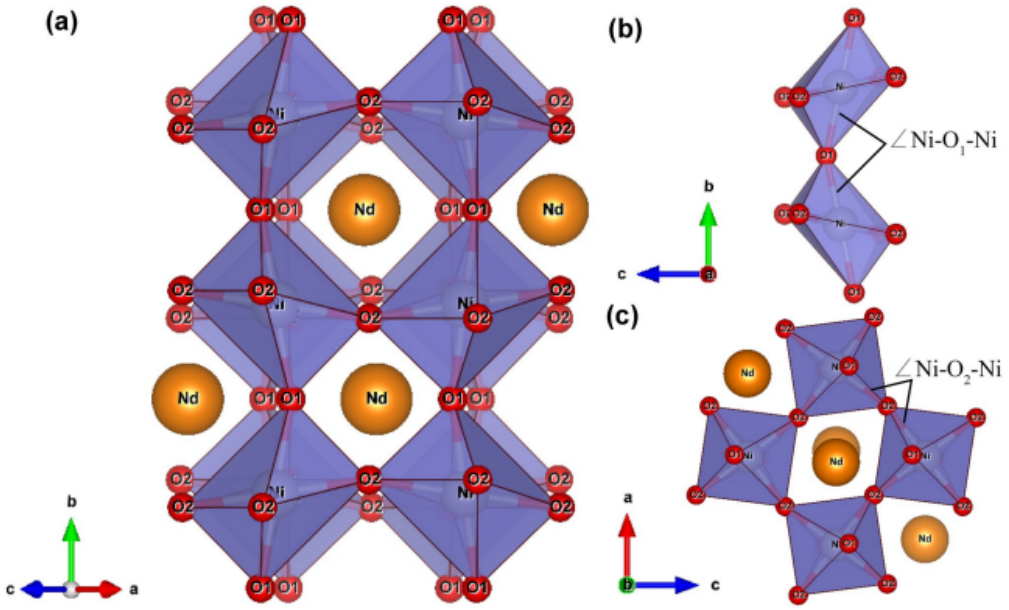

Figure 1.1. Schematic diagram of unit cells,(a) NiO_6 **octahrdra and (b)** $< Ni - O_1 - Ni$ **(c)** $< Ni - O_2 - Ni$ **angle of** $NdNiO_3$ **material.The Figure is adapted from [12], with permission.**

1.2.1 Structural and electronic properties of bulk $NdNiO_3$

In general the family of rare-earth nickelates are represented by the general formula $RNiO_3$. where R belongs to the Lanthanide series. To understand the structural and electronic properties of family of nickelate one need to explore the nickelate phase diagram (Fig. 1.2) [18]. The complete structural, magnetic, and metal-insulator phase transition of various nickelates starting from A site atom, Lanthanum (La) to Lutetium (Lu) have been shown together in the single-phase diagram. The tolerance factor ($\tilde{t}$), temperature (T) and Ni-O-Ni bond angle (ϕ) are shown for individual nickelates by mentioning the proper magnetic and structural zone in different colors. The tolerance factor ($\tilde{t}$) enhances with the atomic size of A site atom (r_A). The Ni-O-Ni super exchange angle (ϕ) is distorted more from ideal NiO_6 octahedra ($\phi = 180^o$) for the nickelates with less tolerance factor ($\tilde{t}$). The evolution M-I transition is associated with tolerance factor and cationic radius, i.e., M-I transition is found to be observed at higher T for the cases of smaller ($\tilde{t}$) or r_A where the ϕ deviates more from 180^0.

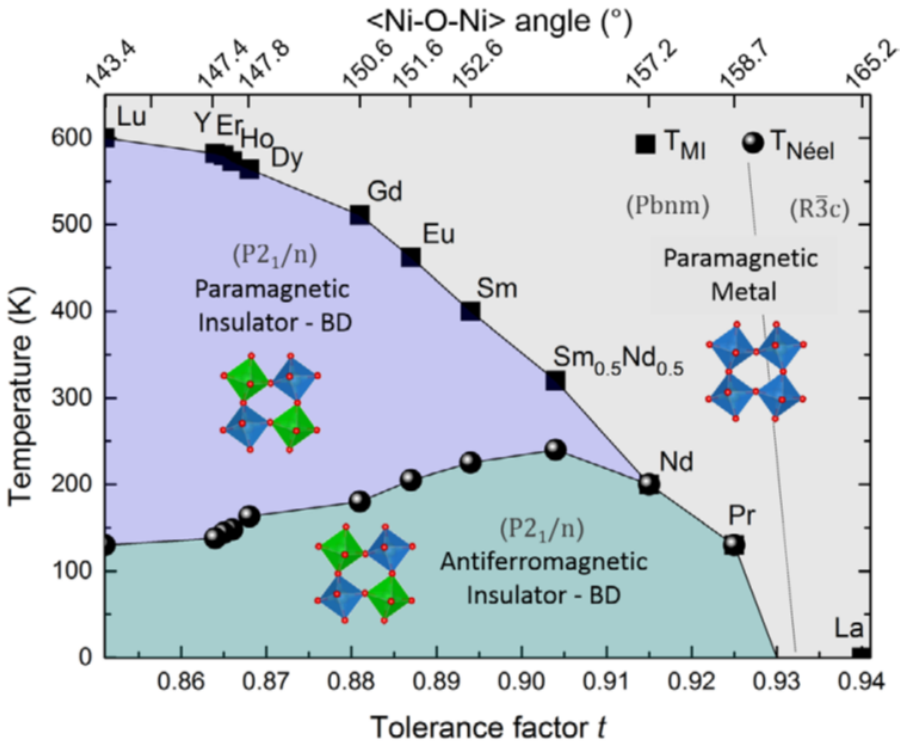

Figure 1.2. The Phase diagram of the $RNiO_3$ family showing the variation of the structure as well as the M-I and Neel transition temperatures as a function of the tolerance factor (bottom x axis) and Ni–O–Ni angle, ϕ (top x axis). adapted from [18], with permission.

The conversion from orthorhombic ($Pbnm$) to monoclinic ($P21/n$) symmetry occurs during MI transition except in $LaNiO_3$ which is rhombohedral ($R3C$).

The low T state is antiferromagnetic insulating state and the high T state is paramagnetic metallic for $NdNiO_3$ and $PrNiO_3$ where Neel and M-I transitions are observed simultaneously. But for the cases where, $r_A \leq r_{Sm}$ (r_{Sm}- ionic radius of Samarium) Neel transition is separated from M-I transition.We have observed good hysteretic resistivity variation on thermal cycling around T_{MI} in $NdNiO_3$, which arises from first order phase transition where T_N is close to T_{MI}. In contrast, for the nickelates ($r_A \leq r_{Sm}$), clear separation between T_N and T_{MI} is observed and the hysteretic behavior of resistivity is rare.

1.2.2 Temperature driven metal-insulator (M-I) transition

The physical origin of M-I transitions in strongly correlated system like nickelate is still an issue of debate. There are several causes like band width control, magnetic ordering, charge ordering, orbital ordering, lattice distortion, JT distortion or combination of above which may be responsible behind M-I transition. The ideally metal and insulator should have the nonzero and zero conductivity at $T \to 0$. Prof. N. Mott proposed the initial idea of

insulating state in M-I transition in the context of localization of electronic wave-function. Further Hubbard improved the model known as Mott-Hubbard model [19]. This model deals with electron hopping from i^{th} to j^{th} sites which makes the i^{th} site empty and doubly occupancy at j^{th} site [20]. As a result, Coulomb interaction energy (U) comes in. The U is split into two bands, upper Hubbard band (UHB) and lower Hubbard band (LHB) which creates charge transfer gap (Δ). For nickelate system, charge transfer takes place between the O 2p band and Ni 3d band.

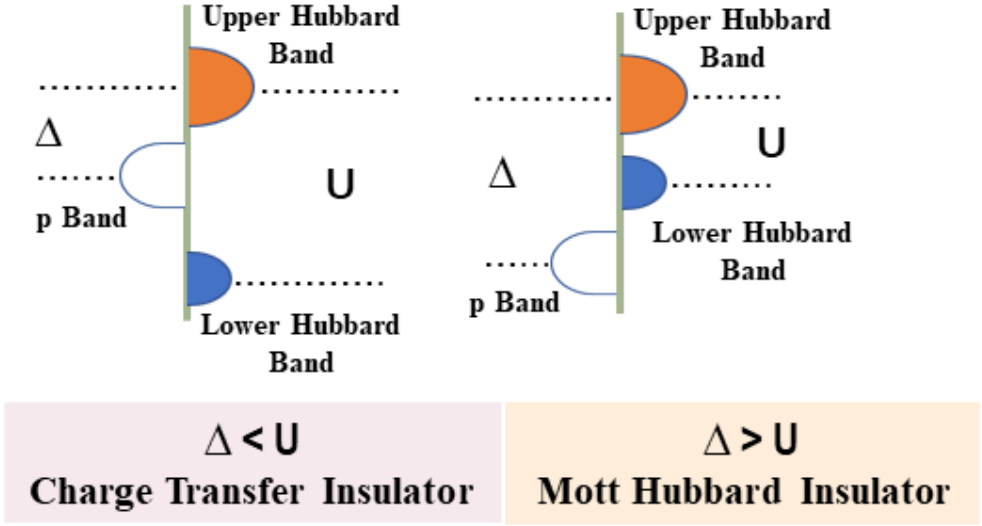

Figure 1.3. The schematic of energy band diagram showing the classification of Mott-hubbard and charge transfer insulator according to ZSA framwork.

J. Zaanen, G. A. Sawatzky and J. Allen (ZSA) proposed a famous framework [21] in 1985 to explain the phenomena which is known as ZSA framework valid for correlated oxide perovskite system. In Fig. 1.3, the UHB and LUB along with oxygen 2p band shown for Mott-Hubbard insulator and charge transfer insulator. In charge transfer insulator, condition is $U > \Delta$ but for Mott-Hubbard insulator $U < \Delta$. The driven force in T dependent M-I transition is thermal energy exchange, The T dependent transfer integral or hopping integral is h_{ij} given by-

$$h_{ij} = \int_r dr \phi_j^*(r)[-\frac{\hbar^2}{2m} + U(r)]\phi_j(r) \tag{2}$$

Where ϕ_j is atomic orbital at j^{th} site. For metallic state $\frac{U}{<h>} \ll 1$ and for insulating state $\frac{U}{<h>} \gg 1$, where $< h >$ is the average hopping integral.

The NiO_6 Octahedra is very crucial which plays an important role in M-I transition. The crystal symmetry changes from orthorhombic to monoclinic during the M-I transition. In low T region, monoclinic crystal structure is observed where, the Ni-O bond length is tuned and Ni-O-Ni angle reduces which results in reduction of Ni 3d and O 2p bands overlap. It helps in localizing the electronic wave-function and the system behaves like an insulator [22].

1.2.3 Why $NdNiO_3$ (NNO)

The reason behind, choosing $NdNiO_3$ (NNO) from nickelete family because of its interesting M-I transition properties.The MI transition occurs around 150 K to 200K which is below room temperature. In this thesis, we planned to explore the physics near and about the 1st order M-I phase transition region in NNO, particularly in presence of disorder. It motivated us to study the slow dynamics region where both the high T metallic and low T insulating phases exist simultaneously near and below the transition region.In NNO, the M-I transition is associated with para to antiferromagnetic transition (Neel temperature, T_N) and orthorhombic to monoclinic (T_{O-M}) structural transition [18, 23, 24].

1.3 Physics of $NdNiO_3$ thin film

Physical properties of poly-crystalline bulk nickelates materials have been investigated extensively [25]. The study on nickelate thin films is also not very old but the challenges involved in thin film synthesis is to grow good quality thin films with desired stoichiometry.The poly-crystalline bulk, highly oriented crystalline film can show more sensitive and sharp electronic behavior specially M-I phase transition in nanoscopic level. Mainly various physical vapor deposition (PVD) techniques like molecular beam epitaxy (MBE), pulse laser deposition (PLD), Radio frequency magnetron sputtering etc. are being widely used to grow NNO thin film [3, 18, 26].

1.3.1 Substrate dependent structural modification in film

The substrate plays a crucial role in thin film growth. Crystallographic growth orientation, strain, structural disorder in the grown films mainly dependent on substrate and hence controls the physical properties of the material. The lattice mismatch between film and substrate generates strain in the film and this strain is irreversible.

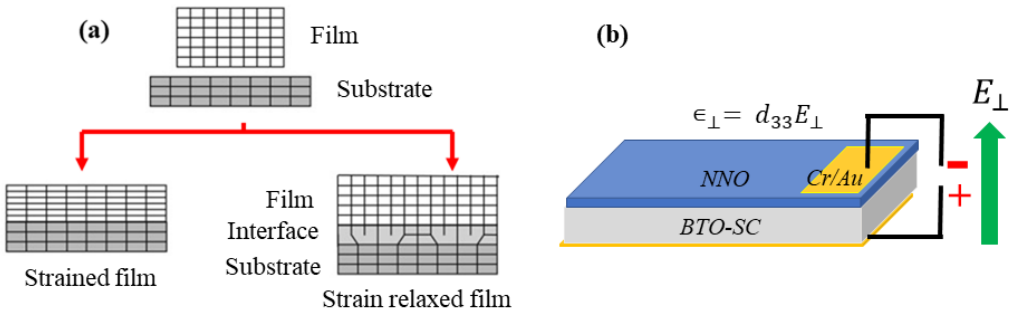

Figure 1.4. (a) Schematic diagram of strain formation in thin film during deposition (b) Schematic diagram of bias-controlled strain in NNO film grown on piezo-electric $BTO-SC$.

The mis-match of different unit cells at interface (substrate/film) leads to strain (distortion of unit cell lattice constant, c(Å)). The lattice mismatch (Δc) estimated by the equation-

$$\Delta c = \frac{c_{film} - c_{sub}}{c_{film}} \times 100\% \tag{3}$$

Where c_{film}, c_{sub} are the lattice constant for film and substrate respectively. The strain governed by lattice mismatch is widely used but the produced strain is irreversible. If the film is elongated along the interfacial plane (in-plane), then the strain is called tensile strain and in another case film's compression along interfacial plane called compressive strain .

Another important way a film can be strained is voltage controlled reversible strain using piezo-electric crystals/film. The strain generation due to application of electric field in piezoelectric substrate followed by the equation-

$$\epsilon_\perp^{sub} = d_{33} \times E_\perp \tag{4}$$

Where $\epsilon_\perp^{sub}$ - out of plane strain, d_{33} - piezo-coefficient, $E_\perp$ - out of plane electric field. In Fig. 1.4 (a), the schematic diagram of strain generation in thin film during film deposition shown.Two types of film can be formed strained film and strain relaxed film. Another type of strain creation in thin film shown in Fig. 1.4(b) which is biased controlled piezo-strain.

1.3.2 M-I transition, presence of mixed phases around T_{MI} and appearance of slow dynamics in NNO film

In several correlated oxide systems like NNO, the observation of phase co-existence between two phases at a finite well-defined temperature range close to T_{MI} has been explored. Investigation around the M-I phase transition temperature (T_{MI}) in NNO where both the phases exist simultaneously and make an inhomogeneous cluster is interesting to study. The physics in the mixed phase cluster zone is associated with phase conversion /transformation phenomena. In this thesis, we have observed the phase coexistence and their transformation to each other with the thermal energy as driving force. In this thesis, the inhomogeneous

phase coexistence and its effects on carrier carrier movements and associated things below the T_{MI} have been investigated. We would like to discuss here a few previous observations by our group which are related to this particular topic.

Observation-I [27] The dynamic phase coexistence between metal and insulator was observed on VO_2 epitaxial film grown on TiO_2 substrate. The phase coexistence leads to a strong inhomogeneity in the MIT region.The Noise measurement established the correlated fluctuations exist at two distinct temperatures T_{C1} and T_{C2} close to T_{MI} whihc are related to the underlying crystallograpihc transition. The phase coexistence observed around a small but particular T range $T_{C1} < T < T_{C2}$ where the electrons loose thermal equilibrium from the phonon thermal bath.

Observation-II [28] Here they observed a large thermal and flicker noise observed near the metal-insulator phase coexistence region in $NdNiO_3$ thin film grown on $SrTiO_3$ substrate with different crystallographic orientation. The value of correlated noise fluctuations reaches maximum at T^* rather than at T_{MI} where the electronic phase separation exists. T^* is situated either above or below the T_{MI}. So a well established mixed phases cluster zone of metal and insulator phase at $T_{C1} < T < T_{C2}$ in observation-I and $T^* \leftrightarrow T_{MI}$ in observation-II have been seen with high value of low frequency correlated fluctuations in noise spectroscopy.

Many groups have investigated the particular phenomena of inhomogeneous mixed phases exclusively in various solid-state systems like VO_2, V_2O_3, $NdNiO_3$ etc. including observations from our group mentioned above. Most of them in VO_2 [29] used the Scattering-type scanning near-field infrared microscopy to probe the local electronic changes which evolve the journey from insulator to metallic phase in the temperate between 300 K to 360K. In V_2O_3 [30], the observation resolved spontaneously nanotextured coexistence of metal and correlated Mott insulator phases near the insulator–metal transition (160–180 K) associated with percolation and an underlying structural phase transition with the help of cryogenic near-field infrared microscopy. In $NdNiO_3$ [31] thin film, the electronic phase separation and percolative phase transition observed by nano-infrared imaging where they have explored the close view of transition region which contains the mixed phases. In Fig. 1.5, The evolution of inhomogeneous mixed phases in $NdNiO_3$ with varying T are shown .

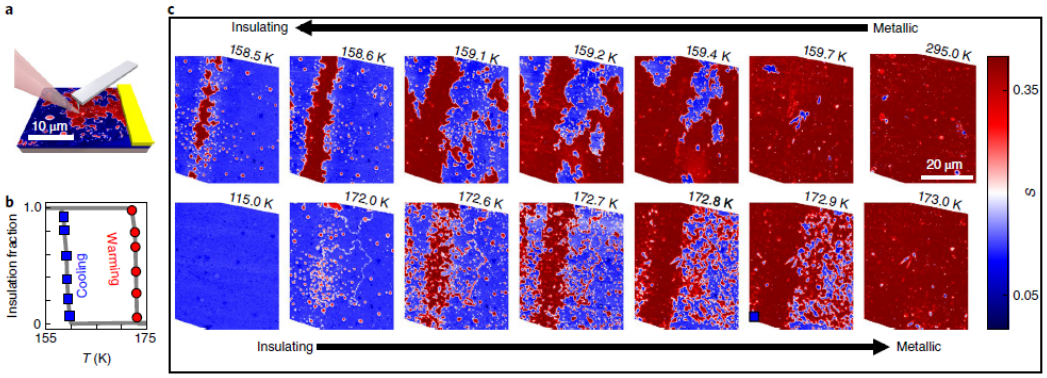

Figure 1.5. Electronic phase separation and percolative phase transition in the $NdNiO_3$ thin film revealed by nano-infrared imaging. (a) Schematic of the nano-IR experiment infrared laser. (b) The Insulating fraction of within nano-IR images (shown in c) across the M-I transition.(c) Images of normalized nano-IR signal acquired while cooling (top) and warming (bottom) through the transition. All images were acquired in a co-localized field of view, except for panels at 115 K and 295 K.The image is adopted from [31] with permission.

Crystal disorder and electronic Griffiths phase

The first theoretical concept [32] of occurrence of "Griffiths Phase" in disordered magnetic systems was proposed in. In presence of crystal disorder, the system becomes inhomogeneous which affects the ferromagnetic transition region. The idea of magnetic Griffiths phase is well established and it is seen in several magnetic system-like manganites [33–38]. In the context of electronic Griffiths Phase, the experimental evidence is not well established barring a recent work on polymeric system although theoretical investigations predicted occurrence of electronic Griffith Phase. It has been theoretically proposed that Griffith phase occurs as a natural consequence of Mott transition with disorder [40]. The electronic Griffiths phase is an analog of magnetic Griffiths phase. It is an electronic state with slow dynamics under two conditions:

- Electronic system in on the metal-Mott insulator boundary that is near or above the Mott transition region.

- The system subject to disorder.

The detail concept of Griffiths phase (in context of ferromagnetic system) can be understood by a report [36] in doped magnetic systems $La_{0.7}Ca_{0.3}MnO_3$ and $La_{0.7}Sr_{0.3}MnO_3$. The Ca doped system has sufficient level of magnetic ions disorder (at random) from their sites (Fig.1.6(a)). In schematic diagram Fig. 1.6(b), the evolution of ferro-paramagnetic transition temperature (T_C) in the range $T_C < T < T_G$ with probability (p) of existence of ferromagnetic cluster in paramagnetic matrix has been shown. The figure indicates $T_C \approx T_G$ for Sr doped system which has less spin dislocation. But in Ca doped system there is definite probability(p) of existence of the new inhomogeneous phase i.e, the ferromagnetic clusters in paramagnetic matrix with singularities in the T span of $T_C < T < T_G$ which is referred as

magnetic 'Griffiths phase'.

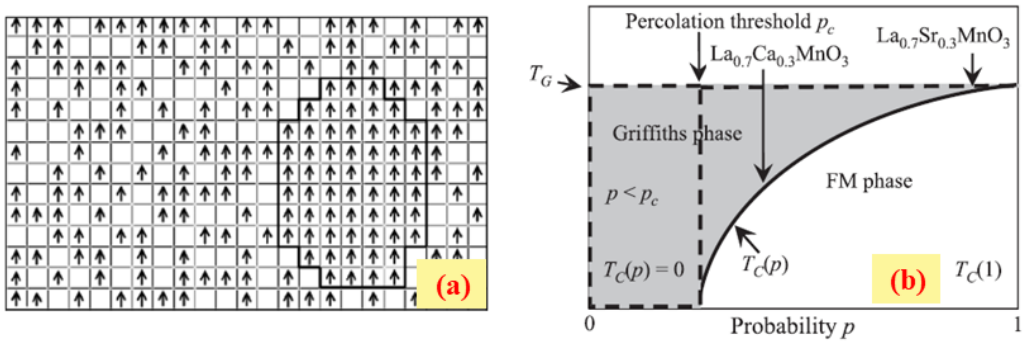

Figure 1.6. (a) Schematic diagram of some of magnetic ions missing (at random) from their sites for $La_{0.7}Ca_{0.3}MnO_3$ (b) The p-T schematic diagram for for a dilute ferromagnetic Ising model.The Figure is adapted from [36], with permission.

Supercooled metallic phase and consequence of M-I transition

In systems like nickelate, supercooled metallic phases exist in the form of metastable state below the transition temperature (T_{MI}) which converts into a stable insulating phases over cooling and during isothermal annealing at $T_a < T_{MI}$. Another type of phenomena can be seen if system have metastable kinetically arrested (or glassy) state, but it is different from the former. The relaxation time for the transformation of the phase, τ, decreases in cooling for the system which has supercooled phase whereas for system with kinetically arrested glassy state τ increases with the decrease in T [39]. The phase transition from water to ice is the best example of 1st order phase transition where supercooled water can be seen down to -42^oC below freezing temperature, which is the limit of supercooling.

1.4 Thesis outline

In this thesis, we have studied the M-I phase transition region of $NdNiO_3$ (NNO) thin film grown on different substrates and explore the mixed phase temperature that occurs close and below T_{MI} , region where the slow kinetics of relaxation sets in. We have grown NNO thin film on various crystalline substrates using Pulse Laser Deposition (PLD) system which is widely used as a physical vapor deposition technique.

We have made an important observation namely, occurrence of electronic Griffiths like phase in NNO system with quenched disorder [40]. The Griffiths phase occurs as a natural consequence of Mott transition with disorder in a system. It is an electronic state with slow dynamics appears in disordered electronic system in on the metal-Mott insulator boundary that is near or above the Mott transition region. The $NNO/BTO/STO$ multilayer is a potential candidate for likey observation of electronic Griffiths phase, as quenched disorder is

present in this system. Using Noise and impedance spectroscopy, it was observed that in addition to the M-I transition at $T_{MI} = 160$ K, there exists a characteristic temperature $T_G \approx 230$ K well above T_{MI} where large low-frequency correlated fluctuations appear, signifying the appearance of phase with slow dynamics.

We exclusively studied the slow kinetics, resistivity relaxation and its temperature dependency in NNO thin films grown on three different substrates below the M-I transition temperature (T_{MI}).The metastable high temperature metallic phase that has its persistence below T_{MI} in the stable low temperature insulating matrix transforms into stable insulating phase over cooling. Two different sets of experiments were carried out. A ramp dependent resistivity measurement in cooling and heating cycles which give us hysteresis with uniform ramping . Other related experiment was isothermal annealing below T_{MI} at a fixed temperature T_a , which has been conducted to study the kinetics. The investigation was carried out in the temperature range 10 K to 300 K with precisely controlled thermal program . For the iosthermal annealig experiment, the cooling was stopped at different anneaing temperatures T_a below T_{MI} and the time evolution of resistiviy was measured. The resistivity was used as a tool to study evolution of the phases. The important observation come out from isotehrmal annealing that the average relaxation time $< \tau >$ decreases on cooling, contrary to the expectation of relaxation through a fixed barrier. As a result, a temperature T^* has been included as the temperature dependence of the barrier, which indicates as "limit of supercooling" or the "limit of metastability." The experimental data was analysed using a Monte Carlo simulation, which is done with a set of physical of parameters including the temperature T^* where relaxation time, $< \tau > \rightarrow 0$ and the energy scale of the transformation E^*.

Reversible voltage-controlled strain can tune the physical properties and the T_{MI} in nickelate system [41] like other ABO_3 perovskite oxides. We used strongly polar substrate ferroelectric and piezoelectric material Barium Titanate (BTO) on which the NNO thin films were grown. The bias controlled strain effect on NNO film grown on of $PMN-PT$ substrate has been reported previously [41, 42]. Here we have used mainly straining effect of BTO layer in $NNO/BTO/Nb:STO$ multilayer and $BTO-SC$ in $NNO/BTO/SC$ film to study the physical properties on NNO under bias unduced strain.

To summarize, the main motivation of the thesis is investigation of several physical properties of $NdNiO_3$ films such as: **(a) Emergence of slow kinetics and electronic Griffiths like phase close to the T_{MI} (b) Kinetics of resistivity relaxation occurring below T_{MI} and signature of supercooling nature of on metallic phases and effects of crystallographic parameters like disorder, grain size, strain etc. ion such relaxation and (c) In-plane resistivity and T_{MI} tuning by piezo-straining effect**. Novelty of the thesis is to use two methods of straining: the irreversible built-in strain that occurs in films due to lattice mismatch and reversible strain generated and controlled by applying bias to a piezo-electric substrate. A new observation, not reported before, was made namely observation of electronic Griffiths phase near and above Mott boundary in presence of quenched disorder.

This thesis has been arranged in following main sections:

1. Introduction
2. Sample preparation, characterization and measurement technique
3. Observation of electronic Griffiths like phase in $NdNiO_3$ film grown on $BaTiO_3/SrTiO_3$ with quenched disorder
4. Phase co-existence, super-cooling and resistance relaxation kinetics in $NdNiO_3$ films below the M-I Transition temperature
5. Effect of voltage controlled reversible strain on M-I transition and other physical properties in $NdNiO_3$ film
6. Conclusions and future directions

- Appendix 1: Synthesis,characterization and transport measurement of $CaPd_3O_4$ material
- Appendix 2: LabView master code for time, temperature and voltage dependent resistance measurement
- Appendix 3: Low temperature transport and bias dependent resistivity tuning of $NNO/STO/PMN-PT$

References

[1] C. Thiele, K. Dörr, O. Bilani, J. Rödel, and L. Schultz, Phys. Rev. B, 75, 054408 (2007)

[2] R. S. Bisht, G. N. Daptary, A. Bid, and A. K. Raychaudhuri, Phys. Rev. B 95, 115147 (2017).

[3] E J Moon, B A Gray, M Kareev, J Liu, S G Altendorf, F Strigari, L H Tjeng, J W Freeland and J Chakhalian, New J. of Phys, 13, 073037 (2011).

[4] P.H. Xiang, N. Zhong, C.G. Duan, X. D. Tang, Z. G. Hu, P. X. Yang, Z. Q. Zhu, and J. H. Chu, J. Appl. Phys. 114, 243713 (2013).

[5] R. K. Zheng, Y. Jiang, Y. Wang, H. L. W. Chan, C. L. Choy and H. S. Luo, Phys. Rev. B 81, 104427 (2010).

[6] F. Tsui, M. C. Smoak, T. K. Nath, and C. B. Eom, Appl. Phys.Lett. 76, 2421 (2000).

[7] D. Preziosi, L. Lopez-Mir, Xiaoyan Li, Tom Cornelissen, J. H. Lee, F. Trier, K. Bouzehouane, S. Valencia, A. Gloter, A. Barthel, Manuel Nano Lett. 7b 04728 (2018).

[8] R. Schmidt, Phys. Rev. B 77, 205101 (2008).

[9] A. M. Alsaqqa, S. Singh, S. Middey, M. Kareev, J. Chakhalian, and G. Sambandamurthy, phys. Rev. B, 95, 125132 (2017)

[10] H. R. Wenk, and A. Bulakh, Minerals: Their Constitution and Origin, Cambridge University Press, 2004.

[11] J.B. Torrance, P. Lacorre, A.I. Nazzal, E.J. Ansaldo, and C. Niedermayer, Phy. Rev. B 45,8209 (1992).

[12] H. Yang, Z. Wen, Y. Cui, Y. Chen, Y. Zhao J. of Superconductivity and Novel Magnetism 34:2339–2347 (2021)

[13] J. Garcia-Munoz, J. Rodriguez-Carvajal, P. Lacorre, and J.B. Torrance, Phys. Rev. B 46,4414–4425 (1992).

[14] J.A. Alonso, M.J. Martı´nez-Lope, M.T. Casais, J.L. Garcia-Munoz, and M.T. Fernandez- Diaz, Phys. Rev. B 61, 1756–1763 (2000).

[15] R. D. Shannon, Acta Cryst. A 32(5) 751(1976).

[16] F. Capon, P. Ruello, J.-F. Bardeau, P. Simon, P. Laffez, B. Dkhil, L. Reversat, K. Galicka, and A. Ratuszna, J. Phys. Condens. Matter 17, 1137–1150 (2005).

[17] M. Medarde, P. Lacorre, K. Conder, F. Fauth, and A. Furrer, Phys. Rev. Lett. 80, 2397,(1998).

[18] S Catalano, M Gibert, J Fowlie, J Íñiguez, J-M Triscone and J Kreisel, Rep. Prog. Phys. 81, 046501(2018)

[19] H. A. GERscH And G. C. KNoLLMAN, Phys. Rev. 129, 959(1963)

[20] A. L. Efros and M. Pollak, Electron-Electron interaction in disordered systems (1985)

[21] J. Zaanen, G. A. Sawatzky and J. W. Allen, Phys. Rev. Lett. 55, 418, (1985).

[22] S. J. Kim, G. Demazeau, J.A. Alonso, and J.H. Choy, J. Mater. Chem. 11, 487 (2001).

[23] M.L. Medarde J. Phys, Condens. Matter. 9 1679 (1997)

[24] G. Catalan, Phase Transit. 81 729 (2008)

[25] P. Lacorre, J.B. Torrance, J. Pannetier, A.I. Nazzal, P.W. Wang, and T.C. Huang, J. Solid State Chem. 91, 225, (1991).

[26] E. Mikheev, A. J. Hauser, B. Himmetoglu, N. E. Moreno, A. Janotti, C. G. Van de Walle, S. Stemmer, Sci. Adv.1, e1500797 (2015).

[27] S. Samanta, A. K. Raychaudhuri, X. Zhong, and A. Gupta, Phys. Rev. B 92, 195125 (2015).

[28] S. Chatterjee, R. S. Bisht, V. R. Reddy and A. K. Raychaudhuri, Phy. Rev. B, 104, 155101 (2021).

[29] M. M. Qazilbash, A.Tripathi, A. A Schafgans, B.J. Kim, H.-T. Kim,Z. Cai, M. V. Holt,J. M. Maser, F. Keilmann,O. G. Shpyrko, and D. N. Basov, Phys. Rev. B, 83, 165108 (2011)

[30] A. S. McLeod, E. van Heumen, J. G. Ramirez, S.Wang, T. Saerbeck, S. Guenon, M. Goldflam, L. Anderegg, P. Kelly, A. Mueller, M. K. Liu, Ivan K. Schuller, and D. N. Basov, Nature Phys 13, 80–86 (2017).

[31] K. W Post, A. S. McLeod, M. Hepting, M. Bluschke, Yifan Wang, G. Cristiani, G. Logvenov, A. Charnukha, G. X. Ni, Padma Radhakrishnan, M. Minola, A. Pasupathy, A. V. Boris, E. Benckiser, K. A. Dahmen, E. W. Carlson, B. Keimer and D. N. Basov, Nature Phys 14, 1056–1061 (2018).

[32] R. B. Griffiths, Phys. Rev. Lett. 23, 17 (1969).

[33] J, Burgy, M. Mayr, V. Martin-Mayor, A. Moreo, E. Dagotto, Phys. Rev. Lett. 87, 277202 (2001)

[34] M. B. Salamon, P. Lin and S. H. Chun, Phys. Rev. Letts 88, 197203 (2002)

[35] J. Deisenhofer, D. Braak, H.-A. Krug von Nidda, J. Hemberger, R. M. Eremina, V. A. Ivanshin, A. M. Balbashov, G. Jug, A. Loidl, T. Kimura, and Y. Tokura, Phys. Rev. Letts 95, 257202 (2005)

[36] V. N. Krivoruchko, Low Temp. Phys. 40, 586 (2014)

[37] R. D. Merithew, M. B. Weissman, F. M. Hess, P. Spradling, E. R.Nowak, J. O'Donnell, J. N. Eckstein, Y. Tokura, and Y. Tomioka, Phys. Rev. Lett. 84, 3442 (2000)

[38] R. H. Heffner, J. E. Sonier, D. E. MacLaughlin, G. J. Nieuwenhuys, G. Ehlers, F. Mezei, S.-W. Cheong, J. S. Gardner, and H.Röder, Phys. Rev. Lett. 85, 3285 (2000).

[39] K. Kumar, A. K. Pramanik, A. Banerjee, and P. Chaddah phys. Rev. B 73, 184435 (2006)

[40] P, Majhi, S. Chatterjee, R. S. Bisht, V. R. Reddy, B. Ghosh, and A. K. Raychaudhuri, Phy. Rev. Matt 5, 085005 (2021)

[41] S. Heo, C. Oh, M. J. Eom, J. S. Kim, J. Ryu, J. Son and H. M. Jang, Sci Rep, 6, 22228 (2016).

[42] J.M. Yan, M. Xu, T.W. Chen, M.M. Yang, F. Liu, H. Wang, L. Guo, Z.X Xu, F. Y. Fan, G.Y. Gao, et al. Phys. Rev. Applied 11, 034037 (2019)

Chapter 2

Sample preparation, characterization and measurement techniques

Abstract:
In this chapter we discuss the methods of preparation of in $NdNiO_3(NNO)$ sample (bulk material pellet and thin film). We also discuss the characterization methods used along with the different measurement techniques used for the works. The bulk material pellet of NNO was prepared by compacting nano particles of the material which was synthesized using sol-gel technique. The films were prepared by pulse laser deposition technique using the pellets.

2.1 Introduction

In this thesis we have explored the physics near and around the metal-insulator transition region of $NdNiO_3$ (NNO) film grown on different single crystalline substrates. To get definite result growth of good quality film is required. Pulsed laser deposition (PLD) technique was used to grow the thin films of NNO. PLD technique has numerous advantages including deposition of large variety of materials and mixtures and ability to maintain proper stochiometry in the film and also good adhesion between films and substrate.

We have synthesized NNO powder as well as thin films for the study. Growth methods of oxide powder and thin films can be classified as chemical and physical processes. Briefly we narrate them-
Chemical process: The sol-gel route was used for preparing the nano-powder and followed by repeated high temperature annealing with oxygen to increase the grain size and to form proper perovskite phase.
Physical process: The main advantage of physical method is to obtain contamination free materials with better crystallinity. PLD technique was used to grow the films and optimization of growth parameters of PLD was done during growth. The phase formation and phase purity and crystallinity of film has been checked by X-ray diffraction (XRD), reciprocal space map (RSM). The composition was checked by the energy dispersive x-ray spectroscopy (EDEX). The thickness of the films was measured by cross-sectional SEM and AFM. The topography of thin film was checked using an atomic force microscope (AFM).

We have prepared single as well as bi-layered films of NNO. For single layered NNO film, single crystalline $SrTiO_3$, $LaAlO_3$, and $BaTiO_3$ substrates were used. As a bi-layered film, the top NNO layer was grown on pre-deposited $BaTiO_3/SrTiO_3$(BTO/STO) . We have also used $SrTiO_3/0.67Pb(Mg_{1/3}Nb_{2/3}O_3) - 0.33PbTiO_3$(STO/PMN-PT) substrate. The selection of substrates were done to have a control on the the built-in strain in the film and the extent of strain relaxation as well as resulting level of disorder within the systems.

The electrical transport measurements were carried out using cryo-generators working down to 9K. A custom-made liquid N_2 based cryostat was used for the impedance and $\frac{1}{f}$ noise spectroscopy measurement. We have also carried out temperature and voltage controlled piezo-strain dependent XRD on the NNO films. The calibration with standard samples before each measurements was performed for all the instruments used in this thesis. For the data acquisition and analysis, we have built-up LabView programs which has been discussed briefly in this section and details in Appendix-B.

2.2 Synthesis of $NdNiO_3$ nano-crystalline powder

The main challenge of growth of nickelate material with proper stoichiometry is due to multi-valency of Ni ions. In general high oxygen pressure is required to stabilized the +3 oxidation state of Ni in $NdNiO_3$ structure [1]. A polymeric synthesis route based on sol

gel synthesis was used to prepare NNO material [2].The precursors, neodymium nitrate hexahydrate $[Nd(NO_3)_3, 6H_2O]$, and nickel acetate tetra-hydrate$[Ni(OCOCH_3)_2, 4H_2O]$ were dissolved in 1:1 ratio of acetic acid and deionized (DI) water in a beaker. The appropriate amount of ethylene glycol was added to the solution. The water and ethylene glycol ratio play an important role to control the particle size of the material [3]. The solution was stirred in a hot plate equipped with a magnetic stirrer at 70^oC for 2 hours and 6 hours at room temperature. The solution was heated until the formation of sol. The sol was allowed to dry and kept at 150^oC for 12 hours followed by pyrolysis at 600^oC for 6 hours, respectively. The final heating for the phase formation was done at 900^oC for 24 hours in a flow of ultra-high pure oxygen gas. The oxygen annealing was done repeatedly few times to get formation of proper phase with homogeneous dispersion.

We have pressed the nano-powder into pellet with 80 MPa pressure and formed target material for PLD. The pellet has been sintered at 900^oC in a tubular furnace under oxygen flow. The pellet was ground and again annealed with 900^oC for 24 hrs. The last step was repeated five times to remove the oxygen vacancy and increase the perovskite phase content. In Fig. 2.1, shows the flow chart of the preparation of nano-powder and pellet.The pellet has been used as PLD target after the characterization.

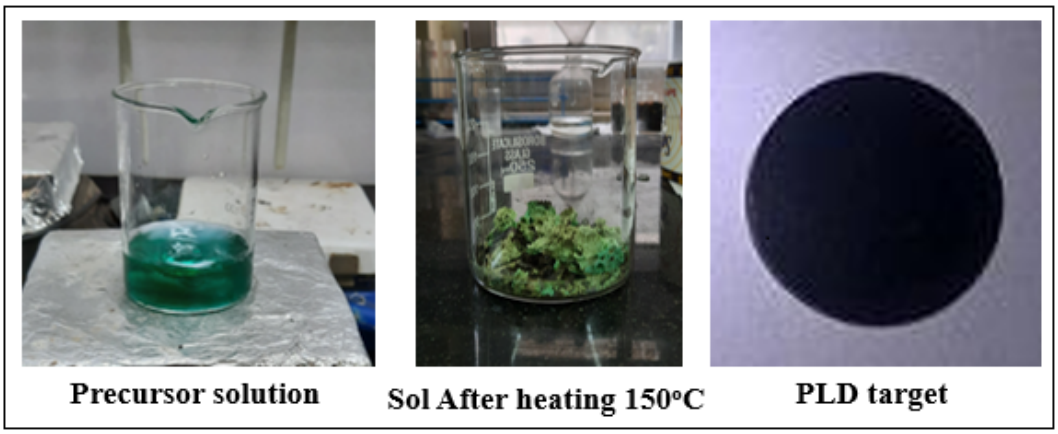

Figure 2.1. Different steps of sol-gel synthesis of NNO nano-power and pellet

2.3 Film growth using Pulse Laser Deposition(PLD)

Pulsed laser deposition (PLD) is a class of physical vapour deposition (PVD) technique where a high energetic pulsed laser is used to melt, evaporate and ionize the material from the surface of a target and the interaction between Laser and target material governs the process [4].A pulse excimer laser is focused on the target material (pellet) which rotates with a constant rpm. The target material is ablated by the high-energy laser pulse in oxygen ambience which leads to the formation of a plasma plume containing ions, molecules,

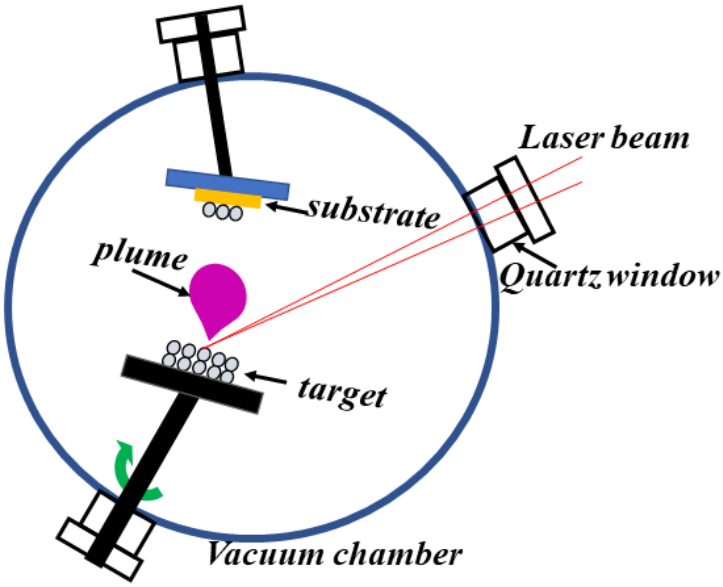

Figure 2.2. Schematic diagram of PLD chamber with plume formation

electrons, etc.A schematic diagram of the PLD setup is shown in Fig. 2.2. The impact of the laser energy vaporized the target material (pellet) in the form of high luminous plasma plume that expands rapidly away from the target surface. The ablated material is deposited on a properly placed substrate upon which it condenses in the presence of a background gas, such as oxygen and growth of thin film occurs. The characteristics of the thin films can be controlled by laser intensity, substrate temperature, buffer gas pressure, and incident angle of the plasma plume. We have used the complex pro 201F KrF excimer laser of wavelength 248 nm for the film growth. The photograph shows the PLD unit in laboratory used for thin film growth in Fig. 2.3

The following steps are followed which are written in the flow chart as the detail process of thin film formation using PLD – Interaction with Laser pulse with target material → Plasma plume formation → Slowing down of plasma plume in oxygen ambience → Nucleation starts on substrate → Thin film formation.

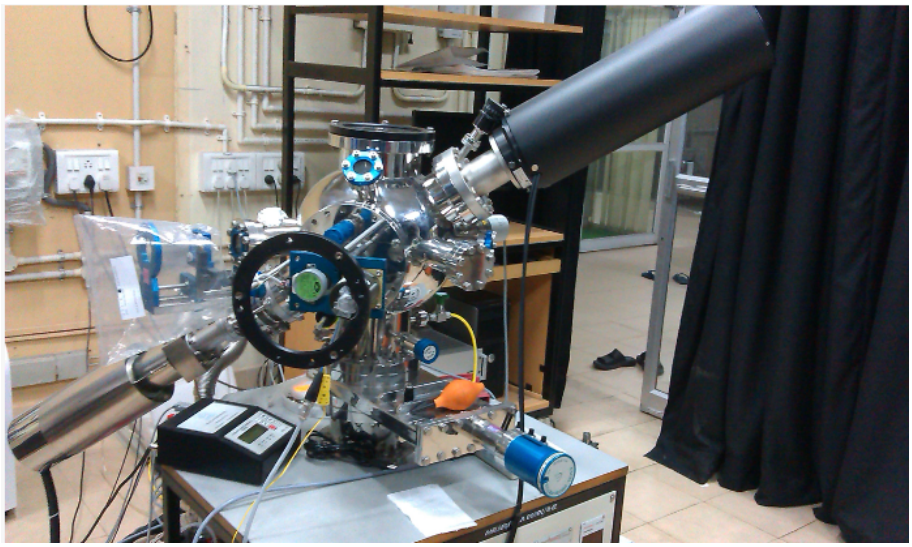

Figure 2.3. Photograph of PLD unit

2.3.1 Selection of substrate

There is a significant impact of the substrate on the growth of film i.e.during the film deposition, the growth is strongly controlled by lattice match/mismatch between film and substrate and other related parameters. The selection of substrates was done, keeping in mind the following criteria (a) lattice match/mismatch which controls the in-built strain,dislocation density etc.(b) substrate's crystallographic orientation which influences the film growth direction (c) substrate's surface: roughness which effects the nucleation process.(d) Type of substrate: conducting substrate required specifically as bottom electrode for our work which we use to apply electrical bias. In table-1, the detail specification of the substrates used for the thin film growth in this dissertation has been mentioned. Thin films of NNO of thickness $\approx$ 25-30 nm were grown on different substrates:

Table 1. Comparison of the substrates used for growth of NNO

Substrates used for optimization				
Substrate	Crystal system (room temperature)	Orientation	ΔC with NNO (%)	Substrate surface
$SrTiO_3(STO)$	Cubic	$<100>,<001>$	-2.6	non-conducting
$LaAlO_3(LAO)$	Pseudo-cubic (Rhombohedral)	$<100>,<001>$	-0.8	non-conducting
$BaTiO_3(BTO)$	Pseudo-cubic (Tetragonal)	$<100>,<001>$	-5.69	non-conducting
$0.67Pb(Mg_{1/3}Nb_{2/3})O_3 - 0.33PbTiO_3(PMN-PT)$	Pseudo-cubic (Rhombohedral)	$<100>,<001>$	-5.25	non-conducting
$Nb : SrTiO_3(Nb : STO)$(0.7% Nb doped)	Cubic	$<100>,<001>$	-2.6	conducting

lattice mismatch(Δc)= $\frac{c_{film}-c_{substrate}}{c_{film}} \times 100\%$

Along with the single layered NNO film, We have prepared two bi-layered films NNO/BTO/STO(Nb:STO) and NNO/STO/PMNPT. In bi-layered film, the layers have been deposited simultaneously without breaking the vacuum.

NNO/BTO/STO(Nb:STO):

This is an unconventional bi-layer with NNO as a top layer. NNO films have been deposited on several close lattice matched substrate like $SrTiO3$ (STO), $LaAlO_3(LAO)$, $NdGaO_3$ (NGO) etc. [5–7] and the metal-insulator transition(MIT) phenomena were studied. But NNO film deposition on pre-deposited BTO in the configuration BTO/STO or BTO/Nb:STO where lattice mismatch is large (about $\geq 5.86\%$) is not common. A well characterized BTO pellet was used to deposit BTO film on STO or Nb: STO substrates. We have chosen this geometry keeping two important things in mind. Firstly, the large mismatch between NNO and BTO layer creates large misfit dislocation which lead to strain relaxation in NNO film. This leads to creation of disorder in the NNO film. This broadens the MI transition and provides the disorder needed to observe an important physical phenomena namely electronic Griffiths phase (discussed in detail in chapter 3).Secondly, the NNO/BTO/Nb:STO bi-layered film was adapted for another important work used in the thesis i.e bias-controlled strain measurement study on NNO film. It is an common practice to use the single crystalline piezo-electric substrate like PMN-PTor BTO to generation of piezo-strain on the top NNO layer [7]. But in this thesis, we used not only the single crystalline PMN-PT and BTO

substrate to generate piezo-strain but also we used PLD deposited BTO layer for the same in NNO/BTO/Nb:STO. Here a part of Nb:STO substrate surface has been covered by a metal mask during bilayer (NNO/BTO) deposition. Later a Cr/Au contact pad was put on the masked portion for the out-of-plane voltage bias application.Here the role of conducting Nb: STO not only as substrate but also as bottom electrode to apply the voltage. In a schematic diagram (Fig.2.13) the geometry has been shown.

NNO/STO/PMN-PT:

Another bi-layer NNO/STO/PMN-PT film is used in the thesis.The STO layer of thickness 3-5 nm was used as buffer layer to improve the lattice matching. The buffer layer , however, reduces the bis generated strain transfer from the Piezo-electric PMN-PT substrate.These substrates are cut in 2 mm $\times$ 5 mm dimension using diamond saw, wire cutter and has undergone successive boiling and ultrasonication in benzene, acetone and ethanol to clean organic impurities from the surface.

2.3.2 Optimization of growth parameter

There are some deposition parameters in PLD which control the film growth. After optimizing the parameters we have finally achieved the desired growth condition for NNO film. The important parameters are-

- Laser fluence
- Substrate temperature
- Rate of deposition
- Oxygen partial pressure
- Pre and post annealing

In PLD, the laser fluence(J/cm^2), laser energy, and ionization degree of the ablated material will affect the quality and stoichiometry of NNO film [9].These laser parameters control the deposition flux which has the direct influence in nucleation density of film growth. The required substrate temperature has been attained by the heater coil attached with the sample holder. The rate of deposition has been controlled by laser frequency which we have varied from 3 to 5 Hz and pulse width $\approx 20ns$. The ambient oxygen pressure controls the deposition rate as well as the oxygen stoichiometry which have impact on the structural and physical properties like M-I transition of the NNO film. The substrates were annealed for 15-20 minutes to clean out adsorbate . The post-deposition annealing was done with the presence of sufficient oxygen to control the film surface roughness and oxygen vacancy. We have used low laser fluence to keep in control the rate of ablation of target material and ensured an uniform nucleation as well as thickness of the film [10].

Table 2. Parameters used for growth of NNO

Growth parameter optimization		
Sr no	Parameter	Values
1	Pulse	3-5 Hz
2	Substrate Temperature	650 - 700 °C
3	Oxygen Pressure	0.2 mbar
4	Fluence	1.7 J/cm^2) $-$ 3.7J/cm^2)
5	Post Annealing Temperature	700 °C
6	Post Annealing oxygen pressure	0.3 mbar - 1 atm

2.4 Characterization of NNO films and bulk pellets

The single and bi-layered films of NNO along with the NNO pellet (target material of PLD) were characterised before using them in experiments. We have used X-Ray diffraction (XRD), Reciprocal Space Mapping (RSM), (Scanning Electron Mapping (SEM), Energy Dispersive X-Ray analysis (EDAX) and Atomic Force Microscop (AFM) for the characterization of the samples. NNO shows temperature driven M-I transition and its a characteristics phenomena of this materials.

2.4.1 Metal-insulator phase transition observed in NNO materials

The NNO material both in bulk and thin film shows temperature driven M-I transition. We have observed the first-order Mott transition at a well-defined temperature T_{MI} in pristine form of the material where the low temperature insulating phase sets in on cooling. The Mott transition, like any other first-order phase transition is accompanied by hysteresis [11]. People have investigated the cases of non-stoichiometric (specially oxygen deficient) [12], disordered [10], strained [14] films of NNO where the hysteresis & T$_{MI}$ are deviated from the well defined temperature T_{MI}. We have observed the T_{MI} along with hysteresis in NNO films and pellet and confirmed the good quality of material grown (Fig. 2.4). In table 3, a survey of the M-I transition temperature on various thin films and pellets have been conducted as a comparison with our prepared samples.

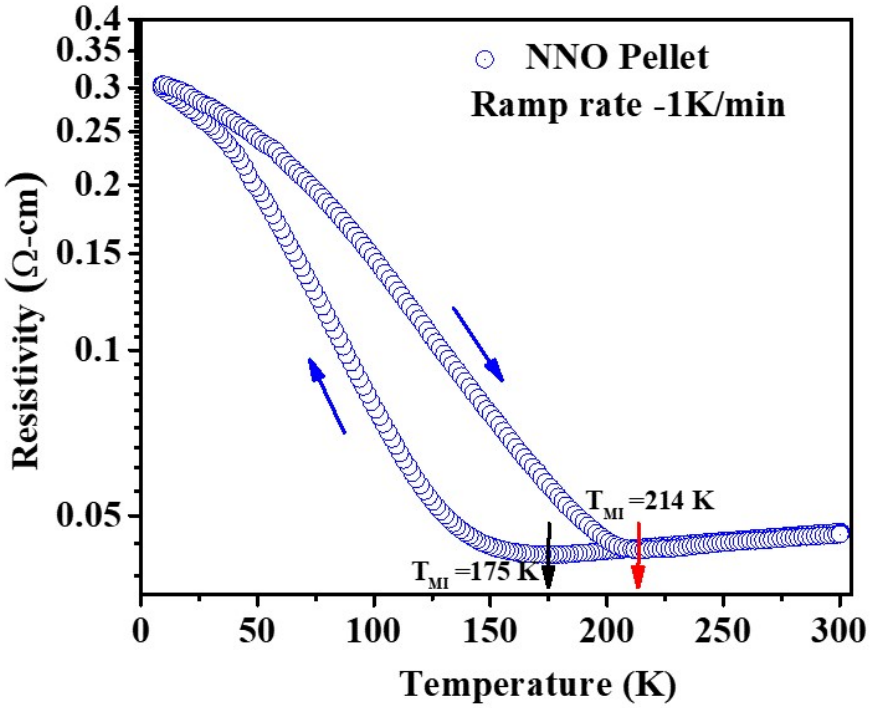

Figure 2.4. The resistivity data of $NdNiO_3$ material in pellet form down to 9 K at uniform ramp rate 5K/min showing the M-I transition

Table 3. M-I transition temperature (T_{MI}) at ramp 1 K/min

Comparison of T_{MI} with literature				
Sr no	Sample	T_{MI}(K) H, C	From literature, T_{MI}(K) H, C	remarks
1	NNO pellet	214, 175	219, 175 [15]	Closely matching
2	NNO/LAO	153, 121	148, 110 [6]	Roughly matching
3	NNO/STO	202, 192	177, 160 [5]	Our film texture and grain morphology is different.
4	NNO/STO/PMN-PT	159	152 [6]	Closely matching
5	NNO/BTO/STO	160	[10]	Unconventional bi-layered film

2.4.2 Results of characterization of NNO films and bulk pellets

X-ray diffraction

The X-ray diffraction (XRD) is a non-destructive primary characterization tool mostly used in material characterization.The XRD used to understand the crystal structure, crystallinity, and phase identification. The basic principle of diffraction theory: wavelength (λ) of electromagnetic radiation should be comparable with the order of spacing of the grating i.e the inter planner spacing of crystal. The X-rays will be scattered when the monochromatic beam falls on a crystal and interact with oscillating electric field. The interference will be constructed due to the periodic arrangement of atoms in some direction govern by the Bragg's equation-

$$n\lambda = 2dsin\theta \tag{1}$$

Here n- order of reflection, θ-angle between Bragg's angle planes and incoming X-rays, λ-the wavelength of X-ray($\lambda = 1.54$Å), and d-inter-planar spacing. In this thesis, we have used PANalytical X-PERT Pro and Rikagu diffractometer for the XRD study of films and pellets.

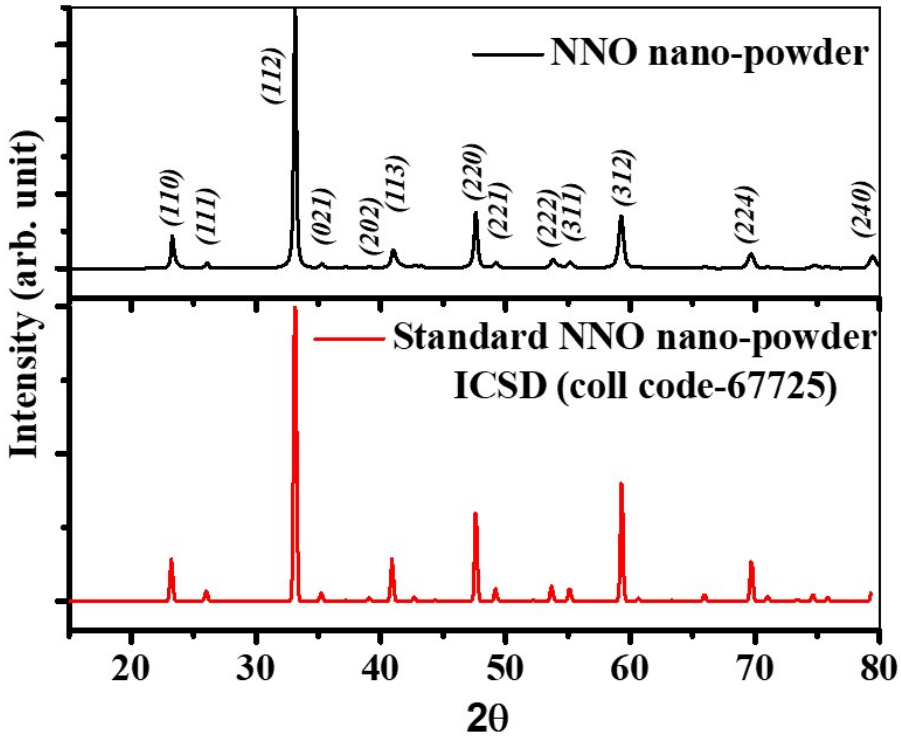

Figure 2.5. XRD data of powder used for NNO pellet

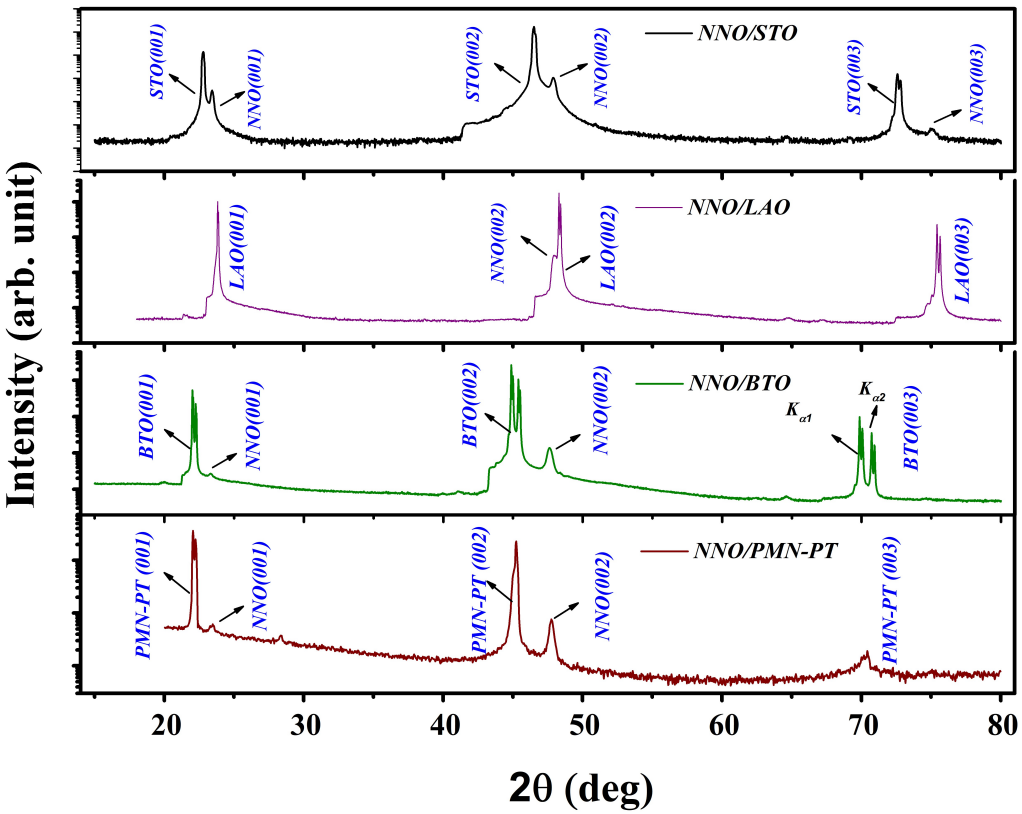

Figure 2.6. The XRD data of NNO films grown on STO, LAO, BTO, and PMN-PT single crystalline substrates

In the XRD data (Fig. 2.5) of NNO powder shows poly-crystalline nature which confirms the proper perovskite phase content and the data has been compared with standard ICSD data.From the XRD data (Fig. 2.6) we have observed that NNO films grown on STO, LAO, BTO, and PMN-PT substrates are highly oriented film with growth along (001) crystallographic direction.

Scanning Electron Microscope and Energy Dispersive X-ray Spectroscopy

The Scanning electron microscope (SEM) is a type of electron microscope where an electron beam is used to gather the information about surface morphology i.e texture, crystallographic phase, chemical composition of the sample. We have used the SEM instrument (Quantum FEG 250), where the electron beam is produced from a field emission gun (FEG). After the electron-sample interaction (inelastic and elastic), the following events may appear; electrons spreading out into the materials [17], some of electrons go back flying to the vacuum, which is backs-cattered electrons and some lose their energy and results in the emission of secondary electrons and X-ray, etc. The secondary electrons are detected by the detectors and produces the images. In the interaction of electron with sample, electrons can eject from the inner shell and create holes which are fulfilled by higher-energy electrons

from another shell. This results appear us as the emission of characteristics X-ray. which is mechanism of energy dispersive spectrometer(EDAX) [18] used to determine the elemental composition of the material.

The SEM image (Fig. 2.7(a)) of NNO powder in pellet form shows the top surface which is highly compact with average grain size 120 nm which is obtained from the hystogram plot shown in Fig. 2.7 (b). The Fig. 2.7(c) represent the EDAX spectra for the as-prepared powder materials.The atomic percentage reveals that the samples are stoichiometric.

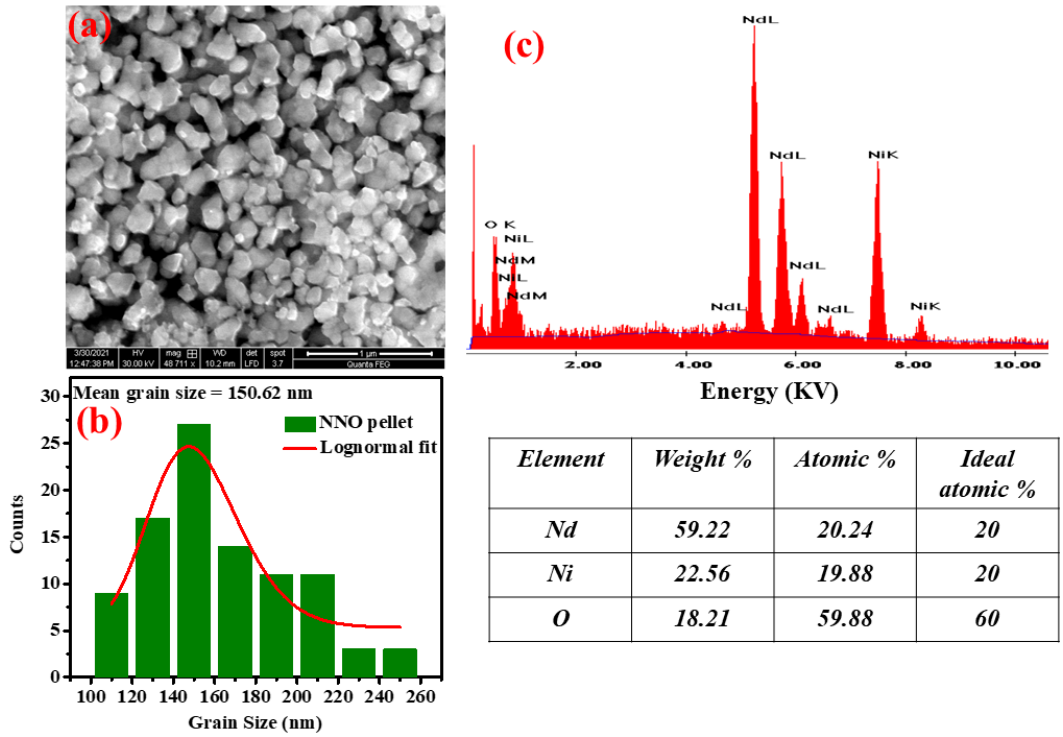

Element	*Weight %*	*Atomic %*	*Ideal atomic %*
Nd	*59.22*	*20.24*	*20*
Ni	*22.56*	*19.88*	*20*
O	*18.21*	*59.88*	*60*

Figure 2.7. SEM and EDAX data of NNO pellet

Atomic Force Microscopy (AFM)

The Atomic force microscopy (AFM) is one of the valuable tools for imaging sample's topography.It consists of a cantilever with a sharp tip (probe) at its end which gathers the information by feeling the surface by the probe.During the scanning, tip comes proximity to the sample's surface which initiate the interactive forces(attractive and repulsive) and for that positive or negative bending appears in cantilever, which is detected by the laser beam.The cantilever is generally made of silicon or silicon nitride with the pyramidal-shaped tip dimension in the order of nanometers.We have used AFM (Model-Nanosurf) for our measurement in both contact and tapping mode type of tip.

The topography images of NNO/LAO, NNO/STO, NNO/BTO/STO films shown in Fig. 2.8. The grain size and rms roughness have been estimated from AFM data. We have estimated the average film thickness ≈ 27 nm by height measurement (shown in Fig. 2.8(d)) where the variation of film height (in nm) with AFM tip movement (in μm) along x direction is shown.

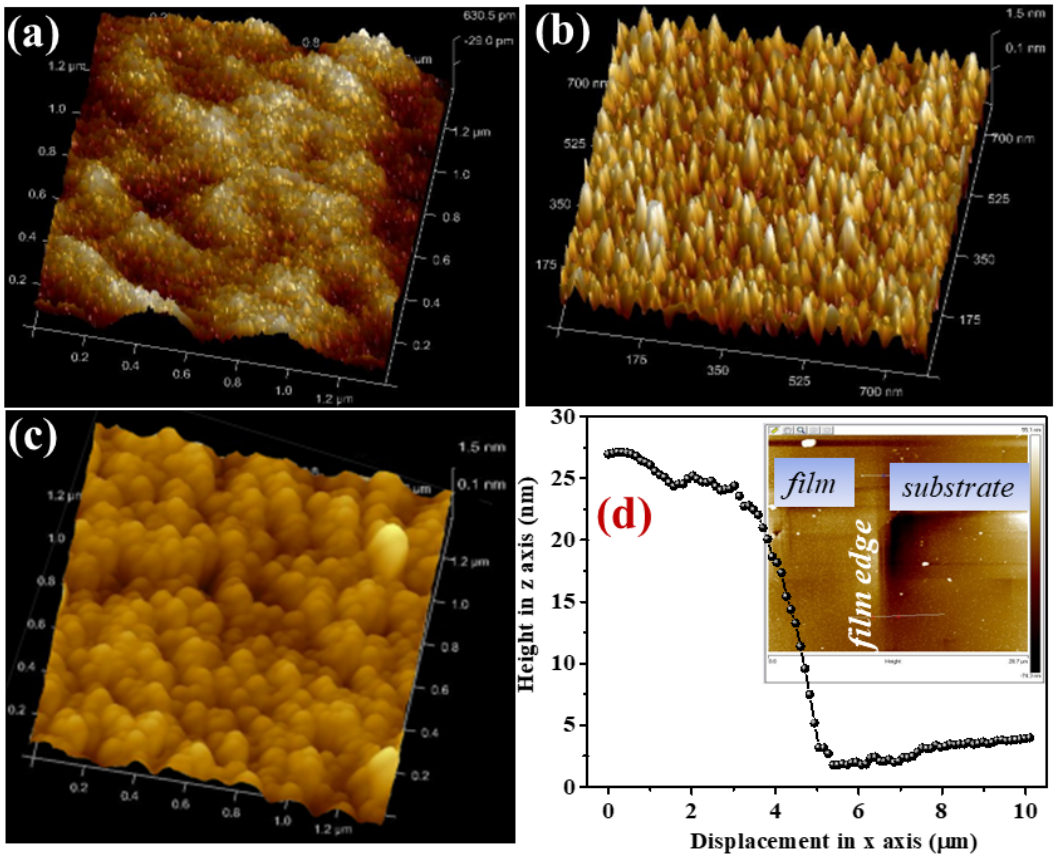

Figure 2.8. The AFM topography images of (a)NNO/LAO (b) NNO/STO (c) NNO/BTO/STO and (d) The film thickness estimation from AFM measurement

2.4.3 Characterization of bilayered films

Characterization of $NNO/BT/STO(Nb:STO)$ bi-layered film

The Fig 2.9 and Fig 2.8 (c) show XRD and AFM data of NNO film grown on BTO/STO (100).The XRD data reveals strongly oriented growth of BTO and NNO on STO(100).The (200) line being the most prominent line is highlighted. The NNO line and the BTO line straddle the STO line. The NNO line being at larger angle than the BTO line, has smaller lattice constant compared to that of the BTO. The lattice constant of NNO film is ≈ 2.51 % smaller than that of STO and the BTO film is ≈ 2.18 % larger than that of the STO film.

Thus, there is a large mismatch of lattice constant between NNO and BTO. The XRD scan shown in Fig.2.9 covers the full 2θ range and shows absence of impurity peaks. The AFM image (Fig. 2.8(c)) shows the surface morphology of the NNO film over a scan area of 1.3 μ m $\times$ 1.3 μ m area. The film surface is highly compact with rms roughness of 1.6 nm. Scan shows growth of coherent grains of average grain size $\approx$ 50 nm along the terrace steps of the substrate.

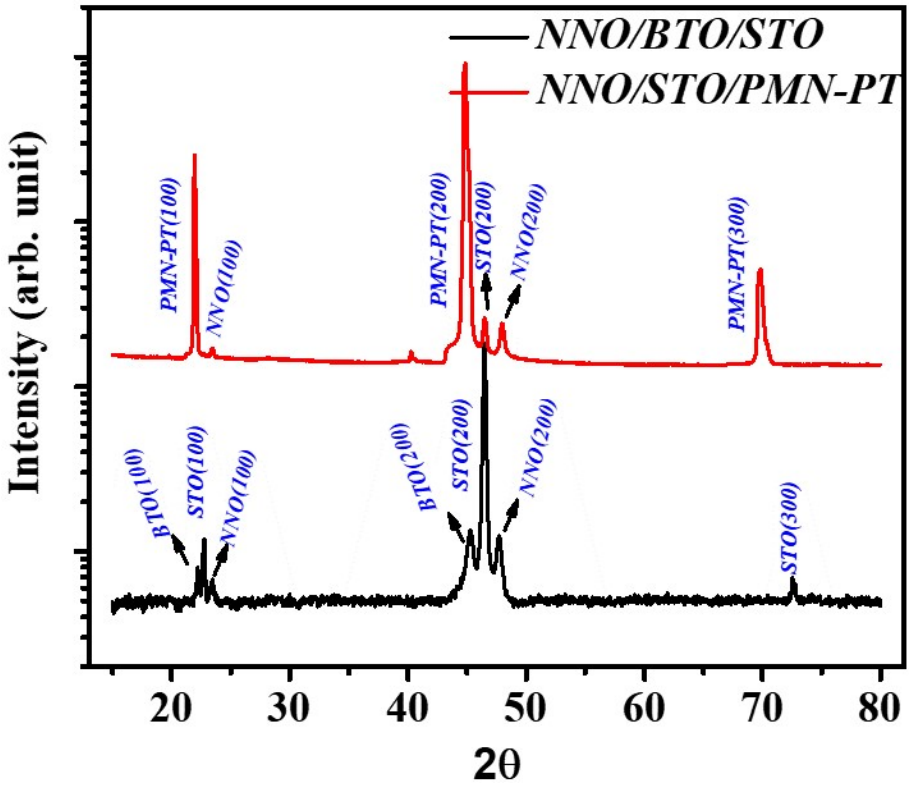

Figure 2.9. The XRD data of bilayered films; NNO/STO/PMN-PT and NNO/BTO/STO

Reciprocal Space Map (RSM)

We have utilised a powerful characterisation technique called Reciprocal space map (RSM) which gives us the idea about peak displacement, peak broadening or peak overlap, off-axis growth and information about strain relaxed growth of thin film.The RSM data was obtained in a Bruker D8-Discover system using Cu K radiation which has been carried out at UGC-DAE-CSR Indore. The Bruker D8 system is equipped with a Eulerian cradle, Goebel mirror, and LynxEye detector.The data were analyzed with LEPTOS software. Information on elastic constants needed for the analysis were obtained from published data [19] .In RSM data we observe the variation of momentum transfer axis q_Z with q_X for (200) and asymmetric (101) direction.

The Fig. 2.10 (c,d) shows the RSM data along film's growth direction(200) which indicates good texture of $BTOandNNO$ layers and from the data along asymmetric (101) direction,we get the confirmation about strain relax growth of NNO layers. The analysis was carried out across the asymmetric (101) reflection. The data obtained from the analysis suggest relaxed states, which is reflected in the value of the relaxation parameter R $\approx$ 0.99. The relaxation parameter can be estimated by-

$$R = \frac{a_{film} - a_{substrate}}{a^R_{film} - a_{substrate}} \tag{2}$$

$$\epsilon_\perp = \frac{c_{film} - c^R_{film}}{c_{substrate}} = 0.51\%, \epsilon_\parallel = \frac{a_{film} - a^R_{film}}{c_{substrate}} = -0.59\% \tag{3}$$

a being the in-plane lattice constant. Subscripts film and substrate refer to film and the substrate, respectively. The superscript R refers to the fully relaxed film.) The out-of-plane and in-plane strain as determined from RSM data. For the NNO film grown on BTO in the $NNO/BTO/STO$ (100) structure, the substrate parameters used are the measured parameters for BTO. The strain relaxation leads to the formation of misfit dislocations which are sources of quenched disorder and which also lead to strain inhomogeneity in the NNO film.

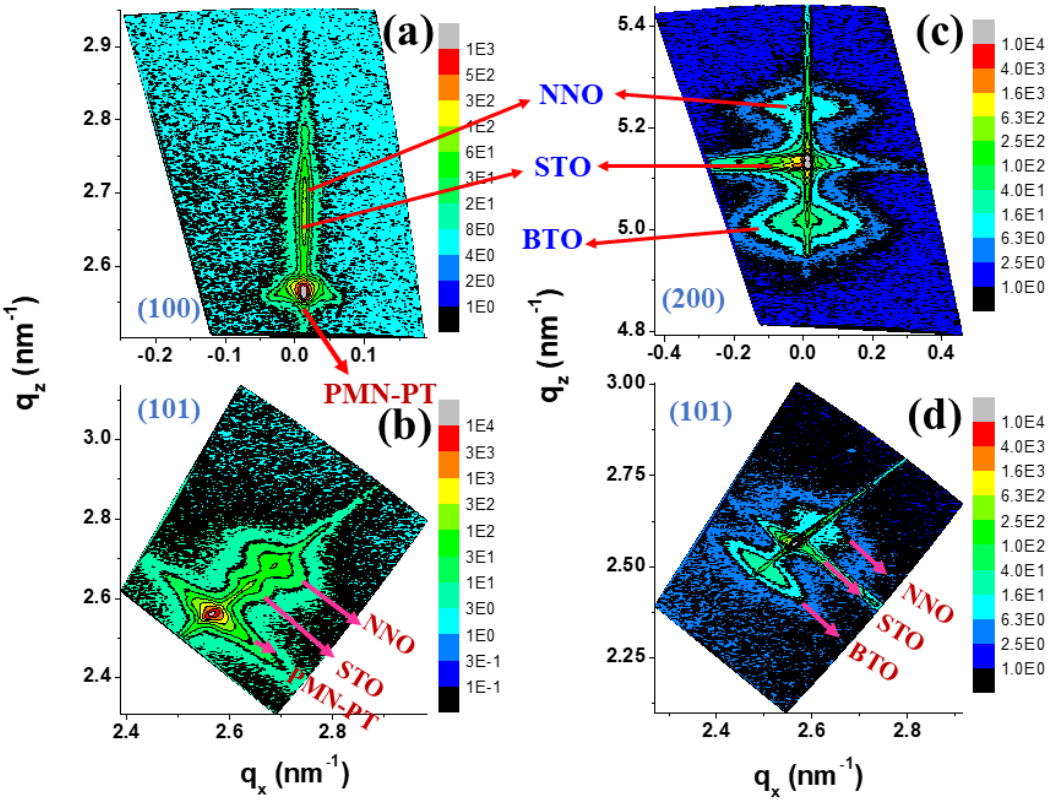

Figure 2.10. The RSM data of $NNO/STO/PMNPT$ along (a) (100) (b)asymmetric (101) direction and of $NNO/BTO/STO$ along (c) (200) and (d)asymmetric (101) direction

Characterization of NNO/STO/PMNPT bi-layered film

The bi-layered film NNO/STO/PMNPT has been characterised by XRD and RSM technique. The XRD data (red line), Fig. 2.9 indicates the highly oriented film growth along (100) crystallographic direction which is strongly textured.The RSM data Fig. 2.10(a,b) along asymmetric direction shows the film is partially strain relaxed with good texture.

2.5 Measurement techniques

2.5.1 Temperature and time dependent resistivity measurement

The electrical resistivity measurements was carried out using lock-in amplifier i.e. 4 MHz lock-in amplifier (Model- SR 865A), Source meter (Model-Keithley 2410), temperature controller (Model- Lakeshore 335) and a cryocooler system based on GM cryocooler (GMC) (Model-Coldedge) down to 10 K connected with a suitable LabView programme which able to record temperature and time dependent resistivity data. We have developed the Labview programme for the thesis, which recorded the resistivity data with both temperature and time simultaneously. We have investigated the low temperature kinetics where we observed and recorded the changes of resistivity with time at constant temperature. A photograph of the transport measurement set-up down to 10K is given in Fig. 2.11

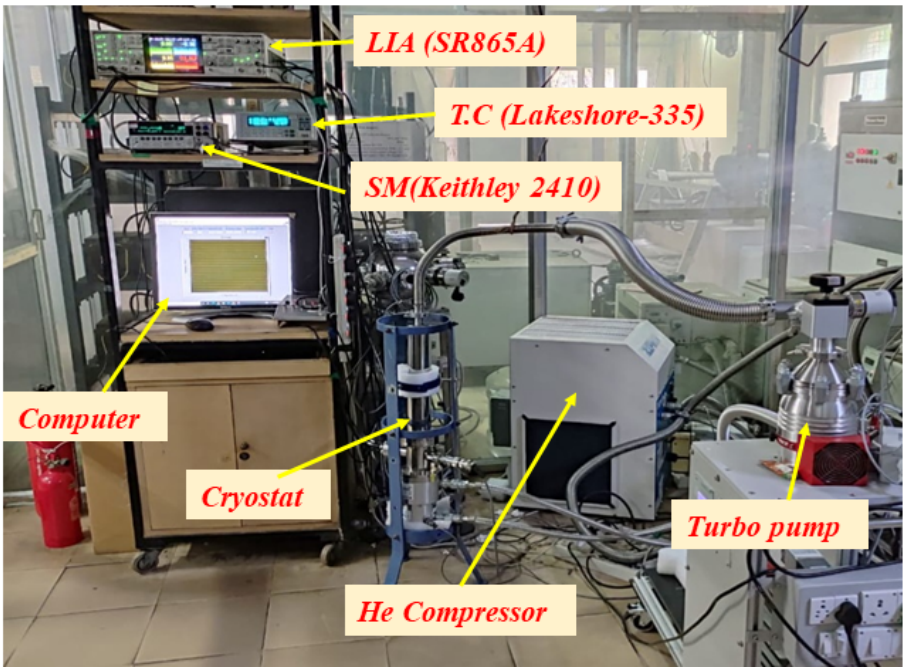

Figure 2.11. The transport measurement set-up

Other than the above mentioned set up, we have also used another type of cryostat equipped with Pulse Tube cryo-cooler (PTC) 405 (Cryomech) down to 3 K (Fig. 2.12 (a)), we have used for resistivity measurement. There are three main components presents in cryo-cooler which are compressor, re generator and displacer [20] observed on GMC.But in PTC, diplacer is replaced by pulse tube.

A custom designed cryostat was also used for the electrical measurements down to liquid nitrogen temperature, 77K (Fig. 2.12 (b)) also. The cryostat was designed with four high-quality coaxial wires (required for sample's 4 probe connection), a Pt-100 temperature sensor fixed on cold stage beside the sample, and the manganin wire used as a heater. The outer jacket of cryostat was pumped down to 10^{-6} mbar pressure before inserting it to the liquid nitrogen bath.

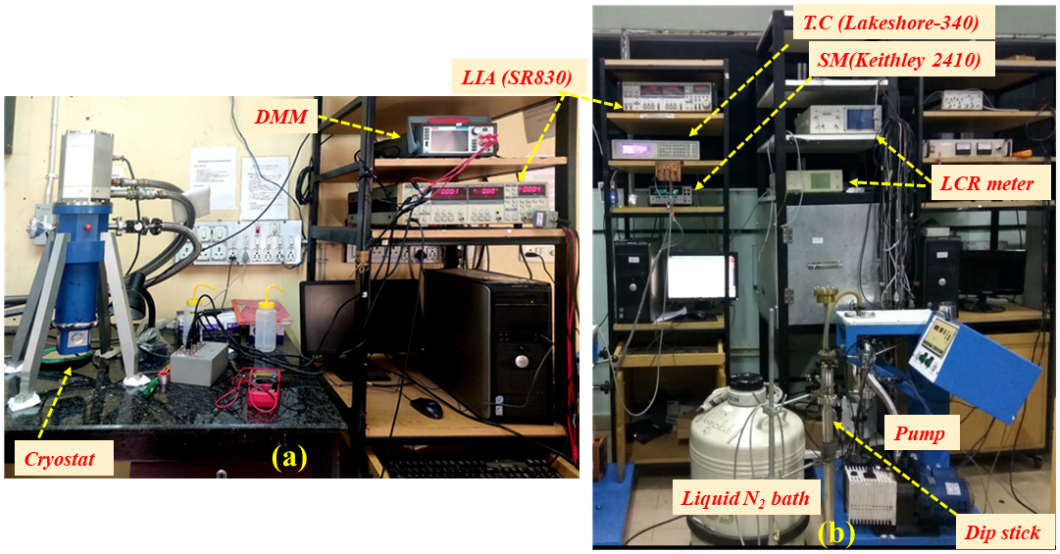

Figure 2.12. The transport measurement set-up (a) down to 3K (b) down to 77 K (custom designed)

2.5.2 Piezo-strain (voltage controlled) dependent resistivity measurement set up

We have developed the strain dependent resistivity measurement set-up where the strain is generated on the piezoelectric substrate due to converse piezoelectric effect on application of an external bias. The resistivity $\rho_{\parallel}$ (in-plane) has been influenced by the perpendicular to the film bipolar bias (field) applied on it $V_{\perp}$ ($E_{\perp}$). The change in resistivity has been measured by the relation -

$$\frac{\Delta\rho_{\parallel}}{\rho}[E_{\perp}] = \frac{[\rho_{\parallel}(E) - \rho_{\parallel}(0)]}{\rho(0)} \tag{4}$$

The experimental set-up was arranged with a source meter(Kethley 2410) for external voltage application, a lock-in amplifier (SR 865A) to measure the in-plane resistivity and a

low temperature cryostat down to 10 K(model coldedge) linked with a suitable labview programme. The schematic diagram is shown in the Fig. 2.13.

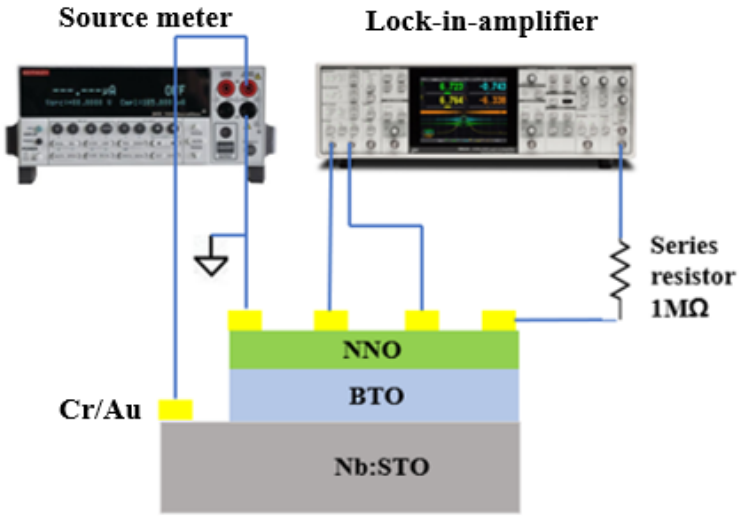

Figure 2.13. The schematic diagram of voltage dependent resistivity measurement set-up along with NNO/BTO/Nb:STO bilayer

2.5.3 Temperature dependent noise measurement technique

The 1/f noise measurements was performed in the temperature range 80K $<$ T $<$ 300 K using a four-probe AC excitation technique (Fig. 2.14).The noise was measured by recording the time series of voltage fluctuations δ v(t) arising due to resistance fluctuation δR in a current biased (I = 1 μA) sample of resistance R. The voltage fluctuation times series δ v(t) was measured by a phase-sensitive homodyne detection method. The homodyne mixed signal was demodulated by a lock-in-amplifier whose output was then digitized with a 16-bit analog to digital converter card of bandwidth 200 kHz. The frequency window of the noise spectrum in our experiment is fmin = 10 mHz to fmax = 7 Hz, which is the band width of detection. At each temperature, one data set was recorded with a sampling rate 1024 data points/s for nearly 16 minutes duration of data acquisition. Thus one data set contains about 1 million points. The stored data were decimated and digitally processed to obtain the power spectra [21]. The spectral power density was calculated from the stored and processed time domain data using method of average periodogram [22]. All the data were taken by stabilizing the temperature with accuracy $\pm$5mK in heating cycle to avoid drift contribution to the fluctuation.

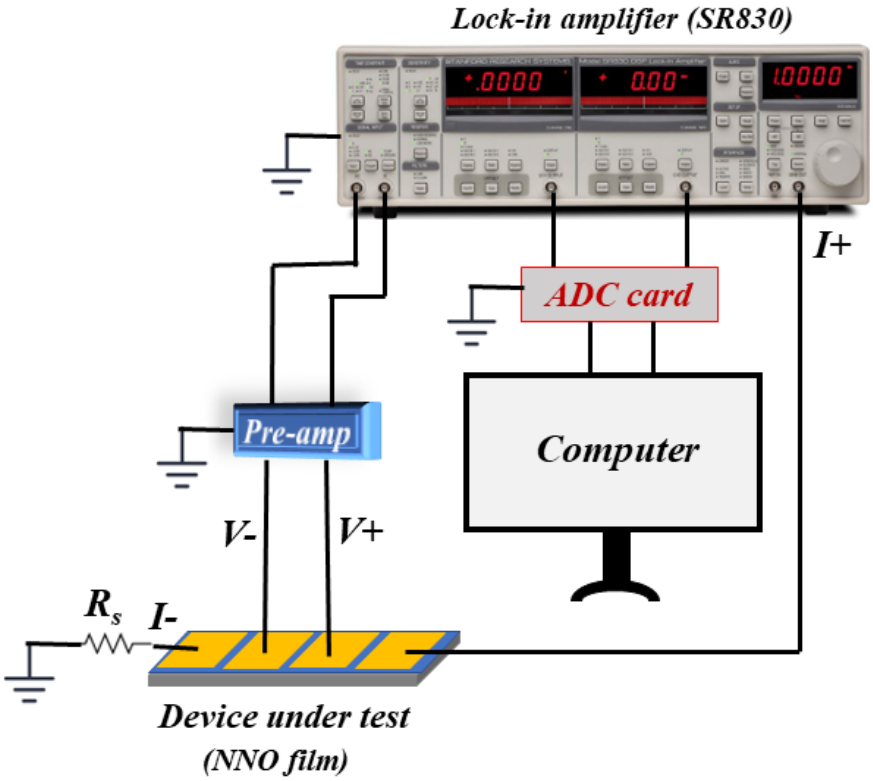

Figure 2.14. The schematic diagram of noise measurement set-up

2.5.4 Impedance measurement set up

We have used a LCR meter for the measurement of complex impedance in a frequency range from 50 Hz to 1 MHz. Two widely used methods; Bridge and network analysis method can be applied to measure the the impedance, phase angle, resistance, capacitor, etc. In the LCR meter bridge method is used with auto-balancing feature and the LCR meter works in a wide frequency range. In our experiments, we have used commercial Hioki 3532- 50 LCR meter, which works from 42 Hz to 5 MHz frequency range. The custom designed cryostat system down to liquid Nitrogen temperature, was set up with the LCR meter and we performed the temperature and frequency ($\omega = 2\pi f$) dependent impedance measurements.The experiment was carried out in the frequency range 100 Hz $<$ f $<$ 1MHz in a planar geometry with current in plane of the film.The open-circuit and short-circuit compensations were done to take care of the capacitive and inductive contributions of the connecting coaxial cables.

2.5.5 Temperature dependent XRD

Investigation of modification/variation of crystallographic structure of NNO with temperature was done down to 4K. We have measured the variation of structural changes as well as the

thermal strain with temperature using the high resolution XRD machine (Model-RIGAKU) facility down to 4K. We have carried out temperature dependent XRD with NNO thin films and found that the M-I transition in NNO is associated with orthorombic to mono clinic structural transition.

2.5.6 Piezo-strain dependent XRD measurement

In this thesis, we have explored the physics of strained thin film. Besides the in-build strain due to film-substrate lattice mismatch, another important way, a film can be strained is voltage controlled reversible strain using piezo-electric crystal/film. The strain generation due to application of electric field in piezoelectric substrate by converse piezoelectric effect followed by the equation-

$$\epsilon_{\perp} = d_{33} E_{\perp} \tag{5}$$

where $\epsilon_{\perp}$, $E_{\perp}$, and d_{33} are the strain,electric field and piezo-coefficient respectively. The subscript $\perp$ refer to the direction perpendicular to the film as shown in schematic diagram, Fig. 2.15 below.The measurement set-up was arranged with the HRXRD machine (Model-Rigaku) along with a sourcemeter (Model-keytheley 2410).We have carried out peizo-strain dependent XRD with NNO/BTO/NbSTO bilayered film and NNO/BTO-SC film.

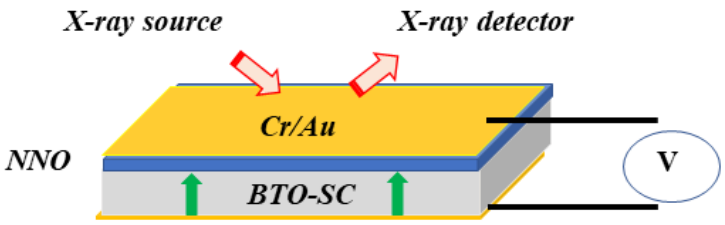

Figure 2.15. The schematic diagram of XRD set-up with arrangement for applying bias on the substrate

The experiment allows us to measure the shift in the XRD lines on the film and the substrate as well thus providing primary calibration of the strain produced by the applied bias both in the substrate and the film .Thus it also provides the extent of strain transfer.

References

[1] R. Jaramillo, F. Schoofs, S. D. Ha, and S. Ramanathan, J. Mater. Chem. C, 1, 2455-2462 (2013).

[2] J.D.G. Fernandes, D.M. Araujo Melo, L.B. Zinner, C.M. Salustiano, Z.R. Silva, C. Alves Junior, J.A.P. da Costa, E. Longo J. of Alloys and Compounds 344, 157–160 (2002)

[3] T. Sarkar, Tuning of ground state and phase transition in complex oxide nanomaterials, Ph.D. thesis, University of Calcutta, India (2018)

[4] T. Venkatesan, X. D. Wu, A. Inam, and J. B. Wachtman, Appl. Phys. Lett. 52, 1193 (l988).

[5] S. Chatterjee, R. S. Bisht, V. R. Reddy and A. K. Raychaudhuri, Phy. Rev. B, 104, 155101 (2021).

[6] R. S. Bisht, S. Samanta, and A. K. Raychaudhuri, Phy. Rev. B 95, 115147 (2017)

[7] G. Catalan, R. M. Bowman, and J. M. GreggJ. of Appl. Phys. 87, 606 (2000)

[8] J.-M. Yan, M. Xu, T-W. Chen, M-M. Yang, F. Liu, H. Wang, L. Guo,Z-X. Xu,F-Y. Fan,G-Y. Gao,S-N. Dong, X-G. Li, H-S. Luo,W. Zhao, and R-K Zheng, Phy. Rev. Applied 11, 034037 (2019)

[9] T.Ohnishi, K. Shibuya, T. Yamamoto, M. Lippmaa, J. of Appl. Phys.103, 103703 (2008)

[10] W. K. Lee, H. Y. Wong, K. Y. Chan,T. Yong, S. Yap and T. Y Tou, Appl. Phys. A 100, 561–568(2010)

[11] Y. G. Liang, S. Lee, H. S. Yu, H. R. Zhang, Y. J. Liang, P. Y. Zavalij, X. Chen, R. D. James, L. A. Bendersky, A. V. Davydov, and X. H. Zhang, I. Takeuchi, Nat. Commun. 11, 3539 (2020).

[12] S. Heo, C. Oh, J. Son and H. M. Jang,Sci Rep 7, 4681 (2017).

[13] P. Majhi, S. Chatterjee, R. S. Bisht, V. R. Reddy, B. Ghosh, and A. K. Raychaudhuri Phy. Rev. Matt 5, 085005 (2021)

[14] P.H. Xiang, N. Zhong, C. G. Duan, X. D. Tang, Z. G. Hu, P. X. Yang, Z. Q. Zhu, and J. H. Chu, J. of Appl. Phys. 114, 243713 (2013)

[15] S. Roy, R. Katoch, R.B. Gangineni, S. Angappan, J. of Solid State Chem. 294 (2021) 121865.

[16] S. Heo, C. Oh, M. J. Eom, J. S. Kim, J. Ryu, J. Son and H. M. Jang, Sci Rep, 6, 22228 (2016).

[17] C. Brechignac, P. Houdy, and M. Lahmani, A textbook of Nanomaterials and Nanochemistry

[18] J. Goldstein, Scanning Electron Microscopy and X-Ray Microanalysis

[19] A. J. Hauser, E. Mikheev, N. E.Moreno, J. Hwang, J. Y. Zhang, and S. Stemmer, Appl. Phys. Lett. 106, 092104 (2015).

[20] Coldedge 10 K cryostat system manual.

[21] A. K. Raychaudhuri, Curr. Opin. Solid State Mater. Sci. 6, 67 (2002).

[22] P. D. Welch, in Modern Spectral Analysis, edited by D. G. Childers, (IEEE Press, John Wiley and Sons, New York, 1978).

Chapter 3

Observation of electronic Griffiths like phase in $NdNiO_3$ film grown on $BaTiO_3/SrTiO_3$ with quenched disorder

Abstract:

In this chapter we investigate diffused metal-insulator transitions (MITs) in an oxide with disorder that undergoes a Mott transition. The investigation was carried out in the multilayer film NdNiO3/BaTiO3/SrTiO3 (NNO/BTO/STO), where a large mismatch of lattice constants of NNO with those of BTO leads to strain relaxation and creation of quenched disorder in the NNO film. The NNO film in the NNO/BTO/STO multilayer structure shows a broad Mott-type MIT at a temperature T_{MI} = 160K from a high-temperature bad metallic with a high value of resistivity $\rho_{DC} \approx 70$m.ohm.cm at 300 K to a low temperature insulating phase. Using noise spectroscopy and impedance spectroscopy which can probe the dynamics of the coexisting phases near the MIT, it was observed that in addition to the MIT , there exists a characteristic temperature $T_G \approx 230K$ well above the MIT, where large low-frequency correlated fluctuations appear, signifying the appearance of a phase with slow dynamics. $T_G \approx 230K$ signals the onset of a temperature region $T_{MI} < T < T_G$ with coexisting phasesthat have been corroborated by the impedance spectroscopy and AC conductivity measurements. It is suggested that the temperature T_G may signify the onset of an electronic Griffiths phase that has been theoretically proposed for Mott transitions with disorder.

3.1 Introduction

Correlation driven metal Mott insulator transition (MIT) in pristine $NdNiO_3$ film [1–3] with negligible disorder shows a the first-order Mott transition in at a well-defined temperature, T_{MI} . For $T > T_{MI}$, the system shows metallic phase with lower resistivity and in Mott transition first order transition accompanied with hysteresis. But the presence of disorder at sufficient level in system rounds - off the transition and in some cases the first order transition ends in a critical point [4, 5].The presence of disorder can stretch the critical region of phase transition. The presence of both disorder and correlation can make the transition diffused with a transition region that extends over a considerable temperature range with co-existing phases. The coexisting phases are the low temperature high resistive insulating phase and the high temperature less resistive metallic phase.In this thesis chapter, we will demonstrate the experimental investigation of MIT in a system with disorder undergoing a Mott transition of diffused nature and we try to explore whether likely appearance of electronic Griffiths phase. The 'Griffiths phase' is a characteristic phase which occurs as precursor of M-I phase transition in such disordered systems. The Griffith phase occurs as a natural consequence of Mott transition with disorder in the system where phase coexistence sets in. The idea of magnetic Griffiths phase is well established and it is seen in several magnetic system-like manganates [6–12] where spin disorder exists at sufficient level.

Theoretical studies of the Mott-Anderson transition with interactions and disorder revealed the presence of an electronic Griffiths phase close to the transition [13–17]. It has been suggested that electronic Griffiths phase, which has been linked to disorder in electronic systems, occurs universally as a precursor to MIT [17, 18].The occurrence of slow kinetics of relaxation as assessed by NMR relaxation served as the Griffith phase's signature near to but above the T_{MI}. [7].There are not too many reports on experimental existence of electronic Griffiths phase, recently it has been showed in organic Mott system but it has not been reported before in some well-known correlated oxide systems like $NdNiO_3$, VO_2 and V_2O_3 which exhibit Mott type transition. Extensive study has been done on $NdNiO_3$ (NNO) films grown on different lattice-matched substrate to investigate investigate the correlation-driven MIT [8].Recently it has been shown in a report that films of NNO on $LaAlO_3$, shows coexisting regions of a low-temperature insulating phase and a high-temperature metallic phase close to the transition region [2]. Coexisting electronic phases with a percolative nature can give to interesting behavior in noise spectroscopy or in impedance spectroscopy (IS) if there is a dynamics associated with the phase co-existence. The Noise spectroscopy and impedance spectroscopy study can be done to probe the dynamics of the coexisting phases near the MIT. Our motivation is to explore whether large lattice mismatch of the film with substrate can make MIT diffuse due to quenched disorder and hence leads to the occurrence of a Griffiths phase [8]. Though there are extensive work on MIT on NNO films but the existence of a temperature T_G, the temperature where Griffiths phase sets in above the MIT has not been investigated. We will explore whether, the large lattice mismatch of the film with substrate can make the MIT diffuse due to quenched disorder and hence shows

a Griffiths phase.To the best of our knowledge,the existence of Griffiths phase above the MIT in NNO film has not been investigated.

In this thesis, the current investigation has been carried out on NNO film grown on $BaTiO_3$ (BTO) film with which the former has a substantial lattice mismatch. The BTO film in turn was grown on crystalline $SrTiO_3$ (STO) (100) substrate. The multilayer sample is referred to as NNO/BTO/STO. Though the NNO films as well as BTO films so grown are oriented and highly textured, the large lattice mismatch and larger thickness of the films lead to strain relaxation in the films leading to creation of quenched disorder and in- plane and out- of- plane residual strains as well as local strain inhomogeneity. The metallic state in such NNO film shows a bad metallic phase with high resistivity and a negative temperature coefficient of resistivity (TCR)($\equiv \frac{1}{\rho}\frac{d\rho}{dT}$)$< 0$. The observed MIT is thus from a bad metal to an insulator. This is unlike MIT seen in NNO films grown on lattice matched substrates like STO or LAO or even good bulk pellets where the high temperature metallic phase mostly have a resistivity $\sim$ 1 -5 milliohm.cm and a positive TCR. We observe that the temperature dependent ρ shows percolative nature of transport occurring due to co-existing phases and the transition region is broad. We also find that in such a film there exists a temperature, which we refer as T_G ($> T_{MI}$) where there is appearance of substantial correlated low frequency fluctuation, slowing down of relaxation time of the correlated fluctuations and evidence of anomalous behavior as observed from the impedance spectroscopy. We explore whether T_G can be identified as onset temperature of electronic Griffiths phase in the temperature range $T_{MI} < T < T_G$. This is an electronic analogue of the magnetic Griffiths temperature.

3.2 Strain state and disorder in NNO layer grown on BTO/STO

The PLD grown NNO on pre-deposited BTO/STO has been characterised with AFM, HRXRD and RSM techniques. The details of sample characterisations have been discussed in Chapter-2. The NNO film is highly oriented in (100) crystallographic direction as revealed by XRD data. The proper strain state has been found out from the analysis carried out across the asymmetric (101) reflection in Reciprocal space map (RSM) data Fig. 2.9 (c, d). The relaxation parameters R $\approx$ 0.99 (Eqn. (2), Chapter-2) which indicates that NNO film is mostly strain relaxed. The grown film has a thickness of nearly $30nm$. The Scanning Probe Microscope image (Fig.2.8 (c), Chapter-2) shows the surface morphology of the NNO film over a scan area of $1.3\mu m \times 1.3\mu m$ area. The film surface is highly compact with rms roughness of 1.6 nm. Scan shows growth of coherent grains of average grain size $\approx 50nm$.

The NNO film grown on BTO is not coherently strained but strain relaxed with residual strain as can be judged from rather large value (-0.59%) of in-plane strain $\epsilon_{\parallel}(\%)$. The strain relaxation in the film would give rise to misfit dislocations. The appearance of grains in the films (with grain boundaries) as shown in Fig. 2.8(c) would give rise to concomitant strain inhomogeneity. We have calculated the dislocation density in NNO layer from the rocking

XRD data. The large lattice mismatch with strain relaxation leads to quenched disorder in the system. From the high-resolution X-Ray data we obtained the rocking curve of the NNO film. From the rocking curve the full width at half maximum (FWHM) (β) was evaluated to be $\approx 2^0$. The data is given in Fig. 3.13 in 'Additional data and information section'

3.3 Temperature dependent resistivity measurements

We have carried out temperature dependent resistivity data in heating and cooling cycle with uniform ramp rate 2 K/min which is shown in Fig. 3.1 (a). The nature of resistivity is quite different than the data of pristine NNO film grown on conventional single crystal substrates like LAO, STO, NGO [2, 21, 22] where the sharp M-I transition is observed with small resistivity $\approx$ 1-2 milliohm.cm at room temeprature. Here the high temperature metallic phase shows a "bad metallic" or marginal type behavior with a high value of resistivity ρ_{dc} of 70 milliohm.cm at room temperature. The temperature coefficient of resistivity in this region $\frac{1}{\rho_{dc}}\frac{d\rho_{dc}}{dT}$ is < 0. The derivative $\frac{d\rho_{dc}}{dT}$ data are shown in Fig.3.1 (b). The value of ρ_{dc} at 300K corresponds to a conductivity σ_{dc} =14.3 S.cm^{-1}, (see Fig. 3.2), which is close to the Mott minimum conductivity value in many oxide systems [5, 23].

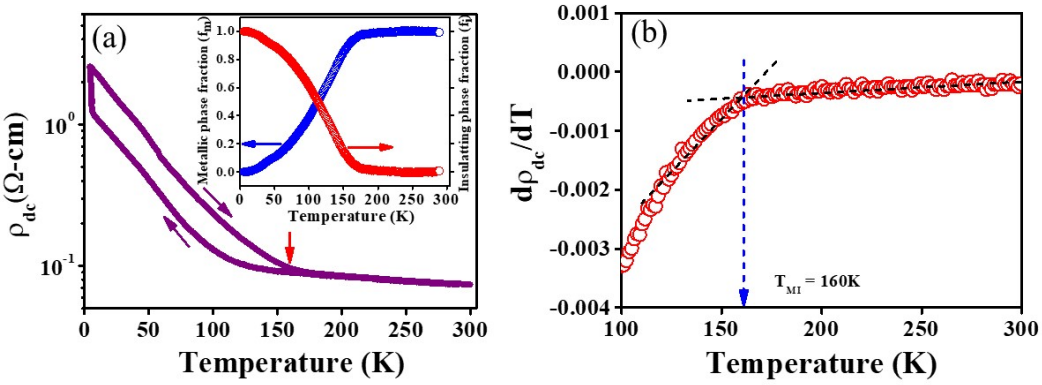

Figure 3.1. (a) Resistivity of the NNO film grown on BTO/STO as a function of temperature. Inset shows the metallic and insulating phase fractions obtained from the resistivity data (heating cycle). (b) Derivative of dc resistivity $\frac{d\rho_{dc}}{dT}$ vs T.The MIT temperature T_{MI} is marked by an arrow.Data taken during heating cycle

A noticeable feature has been observed at lowest T during cooling. The sharp rise in the resistivity at T=4K shown in Fig.3.1 (a). The rise is caused by a time dependent relaxation of the resistance which occurs when the temperature is held during isothermal annealing at constant 4K. The resistance relaxation is related to relaxation of small supercooled portion of high temperature metallic phase (that has lower resistivity) to the low temperature (equilibrium) insulating phase (that has higher resistivity) when the NNO film is cooled below the stability temperature of supercooling which is $< T_{MI}$. We had cooled down the sample down to 4K with a fixed ramp rate 2K/min and waited for around 1 hour till the resistance relaxation is complete and it reaches the equilibrium value for low temperature insulating phase. When it is warmed up again (with same ramp rate of 2K/min) it follows an

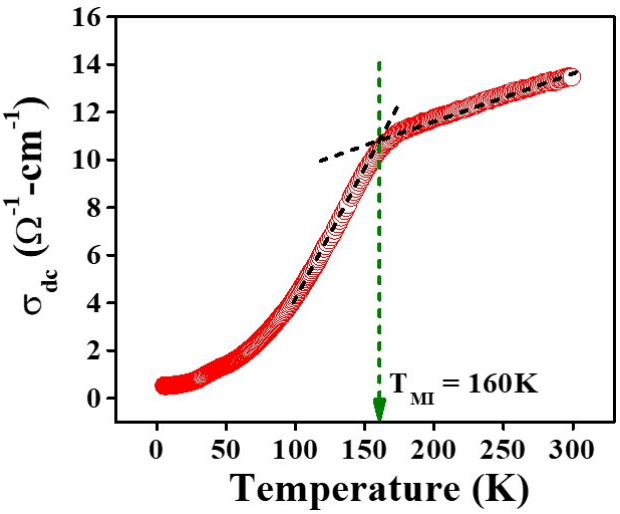

Figure 3.2. D.C Conductivity data at heating cycle showing the M-I transition temperature

equilibrium curve as shown in Fig. 3.1(a). The supercooling phenomena have been observed previously in rare-earth nickelates before ([9, 25]) below T_{MI} and we have discussed the appearance of such time dependent effect in Chapter-4 of the thesis. However, at 30OK the system is in equilibrium.

The insulating state at low temperature ($T \ll T_{MI}$) follows variable range hopping (VRH) relation: $\frac{\rho}{T^{1/4}} = \rho_0 exp(\frac{T_0}{T})^{\frac{1}{4}}$ for $T \leq 10K$. Since the MIT occurs from a bad metallic state to an insulating state both of which have $\frac{d\rho_{dc}}{dT} < 0$, exact location of the MIT temperature (T_{MI}) has an element of uncertainty which is often done through the change of sign of the derivative as has been shown in Fig.3.1(b). Some time T_{MI} can be better identified from the conductivity $\sigma_{dc}(\equiv \frac{1}{\rho_{dc}})$ vs T plot in Fig. 3.2 from these data we locate the T_{MI}=160K.

We have fitted the resistivity of the bad metallic part with the relation $\rho_{dc}(T) = \rho_{0m} - \rho_1 T$, where ρ_{0m} and ρ_1 are constants. The finite non-zero value of ρ_{0m} =0.11 ohm-cm and absence of an activated type temperature dependence indicates large disorder in NNO film grown on BTO, which makes the transition close to Anderson type.

We have used the effective medium approximation with two limiting phases at high and low temperatures respectively [26] to evaluate the phase fractions. The inset in Fig. 3.1(a) shows the metallic (f_m) and insulating fractions (f_i) as functions of temperature obtained from fitting the resistivity data taken during heating cycle. The insulating fraction $f_i \approx 0.1$ at T_{MI}. The co-existing phases near the MIT makes the transition broad and adds a percolative nature to the transition where the relative metallic and insulating phase fractions continuously change with T. If we roughly define the transition width as the temperature region where insulating phase fraction goes from 90% to 10%, the width is found to be $\approx 50K$.The data demonstrate the disordered character of the MI transition, which results in a notable expansion of the transition region. This is unlike the sharper transitions found in films grown on STO, LAO, or NGO that demonstrates the first order nature of transition.

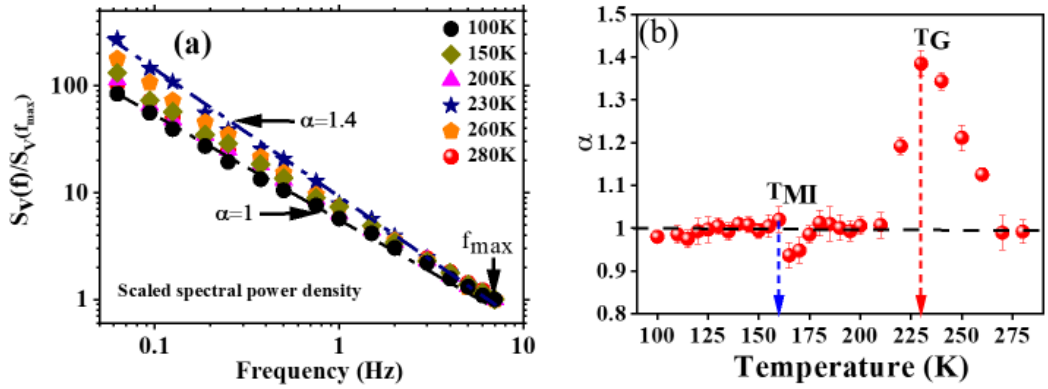

Figure 3.3. (a) Scaled spectral power density $\frac{S_V(f)}{S_V(f_{max}}$ as a function of frequency f in NNO / BTO/STO at few representative temperatures.(b) The exponent α for the spectral power density ($S_V \sim \frac{1}{f^\alpha}$) as a function of T. The α shows a prominent peak at the temperature T_G marked by red arrow. Away from T_G $\alpha \approx 1$. No discernible feature is seen near T_{MI} (marked by blue arrow). The enhancement of α to 1.4 near T_G can be seen in Figure (a)

3.4 Study of the dynamic phase coexistence with noise spectroscopy

When there are coexisting phases, noise spectroscopy is a sensitive probe to study the M-I transition region. The formation of significant low-frequency correlated fluctuations at $T \approx T_{MI}$ has been established in previous reports of $\frac{1}{f}$ noise spectroscopy around the T_{MI} in rare-earth nickelates such NNO and $SmNiO_3$ [2, 27–29].

In this work, the noise spectroscopy is used to identify not only the M-I transition temperature T_{MI} but also it marks clearly another characteristics temperature $T_G > T_{MI}$. Within a temperature region $T_{MI} < T < T_G$ slow dynamics of relaxation sets in and the low frequency dynamics persists over a distinct temperature region. The existence of such a temperature has not been recognised and reported earlier in oxides undergoing M-I transition in previous noise spectroscopy study.

The spectral power density of flicker follows the relation $\frac{S_V(f)}{V^2} \propto \frac{1}{f^\alpha}$. The exponent α was obtained from the frequency dependent spectral power density data by non-linear least square fit. This is shown in Fig.3.3(a), where the data are shown in double-log plot of the scaled spectral power density $\frac{S_V(f)}{S_V(f_{max}}$ with frequency f. $\frac{S_V(f)}{S_V(f_{max}}$ is the spectral power density at a frequency f scaled by its value at f_{max}=7 Hz, which is the maximum of the band width of measurement. As the temperature changes the exponent α evolves non-monotonically as shown in Fig 3.3 (b). It can be seen that the exponent α shows clear enhancement at a well-defined temperature T_G marked by an arrow and it deviates from the value of ≈1.0 as T_G is approached from both above or below. The width of the temperature range around T_G where α shows significant deviation from the value of 1.0 is ≈ 50K. Away from this range α ∼0.95-1.0 as is expected of a conventional flicker noise [30, 31]. The

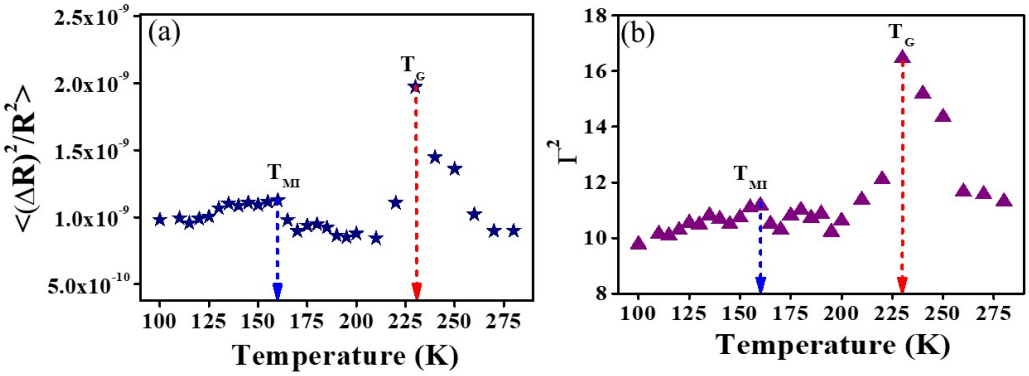

Figure 3.4. (Colour online).(a) Temperature dependence of relative variance of fluctuation $\langle\frac{\Delta R^2}{R^2}\rangle \equiv \frac{1}{V^2}\int_{f_{min}}^{f_{max}} S_V(f)df$. (b) The second spectrum Γ^2 of the noise spectra as a function of temperature. The temperatures T_{MI} and T_G, are marked.

change in the exponent α can be appreciated from Fig. 3.3(b) as well. For T away from T_G, the exponent $\alpha \approx 1$ as can be appreciated from the dotted line that has $\alpha = 1$. As $T \to T_G$ the exponent $\alpha \to 1.4$ as can be seen from the enhanced slope of the line marked in the figure. This is a change in the value of α by nearly 40%. Change of α from 1 to 1.4 indicates that the spectral weight has shifted to lower frequency. It may be noted that α generally has a limited range typically from 1 to 2 as observed from various systems [30].

The Fig.3.4 (a) shows the temperature dependence of the normalized mean square resistance fluctuation $\langle\frac{\Delta R^2}{R^2}\rangle \equiv \frac{1}{V^2}\int_{f_{min}}^{f_{max}} S_V(f)df$, where the integral is over the band width of measurement (f_{min}, f_{max}). (The normalized mean square fluctuation is often referred to as magnitude of noise). The data show that while there is a broad and shallow hump in the noise magnitude in the temperature range $T \sim T_{MI}$, it rises sharply as the temperature T_G is approached from both above and below, where there is appearance of large component of low frequency fluctuation as inferred from the sharp rise in the exponent α. It can be seen from Fig.3.3(b) that at T_G the value of the normalized mean square fluctuation changes substantially by a factor of 2 from its value away from T_G. The Fig.3.4 (a, b) clearly establish that a large low-frequency fluctuations arises in the temperature range $T_{MI} < T < T_G$, as $T \to T_G$.

The large low frequency fluctuations that appear in the temperature range $T_{MI} < T < T_G$, are non-Gaussian . It can be seen in in Fig.3.4(b) that the value of the second spectrum Γ^2 changes from 10 to nearly 17 at $T = T_G$. This would be expected when the noise sources from which the fluctuations arise are correlated in nature. Correlated fluctuation and its non-Gaussian nature have been measured through the normalized second spectrum given by [2, 30, 32].

$$\Gamma^2 = \int_0^{f_H - f_L} S^{(2)}(f_2) df_2 \tag{1}$$

Where,

$$S^{(2)}(f_2) = \frac{\int_0^{\infty} \langle \Delta v^{(2)}(t) \Delta v^{(2)}(t+\varsigma) \rangle \cos(2\pi f_2 \varsigma) d\varsigma}{[\int_{f_L}^{f_H} S_V(f_1) df_1]^2} \tag{2}$$

Where f_1 and f_2 are the frequencies associated with 1st and 2nd spectrum respectively. $\Delta v(t)$ is the measured voltage fluctuation.

Observation of a distinct temperature T_G above T_{MI} which marks the onset of slow relaxation in the system that shows diffused MIT, is one of the principal observations of the thesis. This has not been reported before. This occurs at a temperature range where the metallic phase is the majority phase with very small fraction of insulating phase ($f_i \approx .001$). The temperature range $T_{MI} < T < T_G$ is also distinct where the low frequency fluctuation is correlated as judged from its non-Gaussian nature.

3.4.1 Calculation of correlation function of fluctuation and auto correlation time

The auto correlation function (Φ (t)) of voltage fluctuation ($\delta v(t)$) and the calculated correlation time (τ), assisted to prove the existence of slow dynamics in the special temperature range $T_{MI} < T < T_G$. The auto-correlation function $\phi(t)$ is defined as $\phi(t)$ $\equiv \langle \delta v(t^{'}) \delta v(t+t^{'}) \rangle >_{t'}$, where $\langle ... \rangle_{t'}$ represents the time average and $\delta v(t)$ is the observed times series of voltage fluctuation. It is anticipated that the correlation time of fluctuation (τ) will improve in presence of slow kinetics of relaxation which results in significant increment of flicker noise with high α value in the transition zone. The $\phi(t)$ shows an approximate exponential dependence for small time ($t \leq \tau$) and a long-time tail for $t > \tau$. The dashed line in Fig.3.5 (b), which separates the exponential and non-exponential long time tails, shows the $\phi(t)$ of a few representative temperatures. We obtain the correlation time τ approximating it as the time when $\phi(t)$ becomes $\frac{1}{e}$ of the value at $t = 0$. The long-time tail of $\phi(t)$ contains valuable information on the nature of the co-existing phases in the region $T_{MI} < T < T_G$. The appearance of Griffiths phase above the MIT temperature T_{MI} would need occurrence of sparse phases like small pockets of the high temperature phase embedded in pockets of minority low temperature phases which in turn are dispersed in the majority high temperature phase. Occurrence of such sparse phase will lead to slow relaxation kinetics as has been observed experimentally. Theoretical investigations established that these rare regions can control the long-time dynamics in a Griffiths phase. As a result, the auto-correlation function $\phi(t)$ of the fluctuation has a predominant low frequency contribution. This will lead to a long-time tail which would vary as [18]:

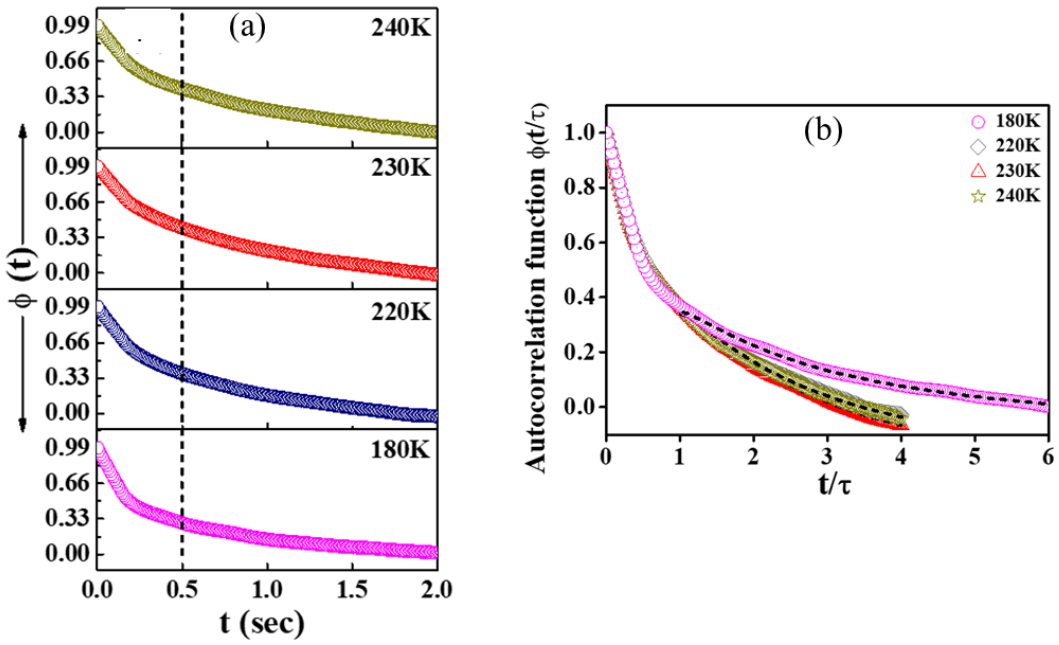

Figure 3.5. (a) Correlation function $\phi(t)$ vs t at some representative temperatures in the range $T_{MI} < T < T_G$. The dashed line demarcates the exponential region and the non-exponential long time scale. (b) Time dependence of the scaled auto-correlation function for fluctuation $\phi(\frac{t}{\tau})$ vs scaled time $\frac{t}{\tau}$ at few temperatures close to T_G. The dashed line through the data at longer times ($\frac{t}{\tau} \geq 1$) shows fit to Eqn. 4

$$\phi(t) \sim exp(-\phi_c(lnt)^{\frac{d}{d-1}}) \tag{3}$$

Where ϕ_c is a constant and d is the dimension. For d=3, one would expect the long-time tail of $\phi(t)$ to vary as $\phi(t) \sim exp(-\phi_c(lnt)^{\frac{3}{2}})$. We find that $\phi(t)$ in the system does grow a long-time tail following Eqn. 7 as shown in Fig. 3.5 (b), where the time axis has been scaled by the correlation time τ which allows scaling of the correlation functions at different temperatures to be represented in a single scaled graph. The solid lines through the data points are fit to Eqn. 7 for d=3. The proposal of existence of sparse phase and the long tail correlation function provides a strong support to the hypothesis that the temperature T_G is analogous to the onset temperature of the Griffiths phase as observed in magnetic phase transitions.

The τ has been obtained directly from the auto-correlation function $\phi(t)$ of the voltage fluctuations [30]. We demonstrate that the τ has a clear temperature dependence, peaking at T_G, where the flicker noise exhibits a prominent peak with the highest α value. In the temperature variation of τ (Fig. 3.6), It is seen that the correlation time gradually increase as T_G is approached either from above or below and it shows a peak at $T = T_G$. The value of τ at the peak is about a factor of 2 larger than that at temperatures away from T_G. The significant enhancement of τ at $T = T_G$ thus corroborates with the appearance of large low-frequency noise in the same temperature range.

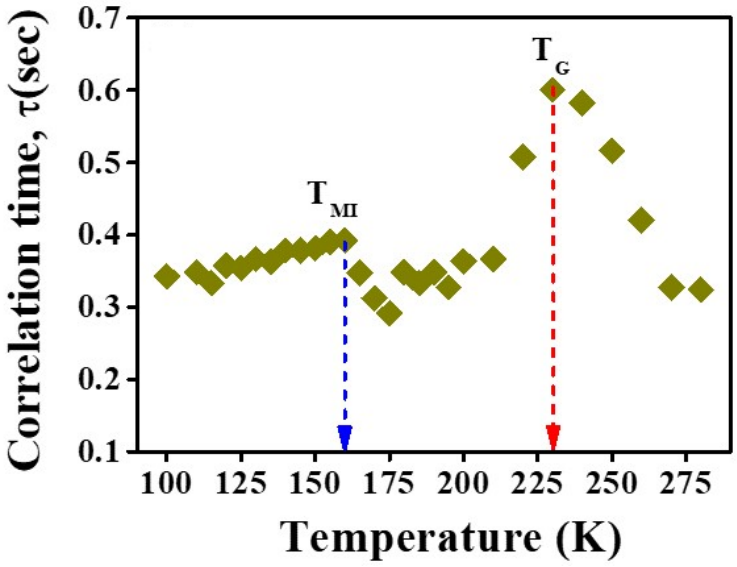

Figure 3.6. Temperature dependence of τ as obtained from the correlation function

3.5 AC conductivity and Impedance Spectroscopy

The temperature dependent resistivity and noise spectroscopy data reveals the T_{MI} and a special phase coexistence region, $T_{MI} < T < T_G$ where the low T insulating phase co-exist with the high T metallic phases. If another independent dynamic probe is used to explore to get the signature of T_G, in the region of temperature where T_G occurs it would be good because, as the minority phase fraction is very small, in DC resistivity measurement it is not observable. Hence, it is needed to do a dynamic probe like Impedance Spectroscopy (IS) that may capture the presence of small regions of a minority phase in a solid with coexisting phases. When NNO was grown on a lattice-matched LAO in a prior work, coexisting phases could be seen in the results from Scanning Tunneling Spectroscopy [2]. The charge relaxation will be determined by conductivities of the coexisting regions in such coexisting regions, where metallic regions of higher conductivity separated by an insulating region will show a capacitive effect which will control the complex impedance. The A.C IS has been used to detect the evolution of capacitive effect and hence the composite mix phase region with temperature.

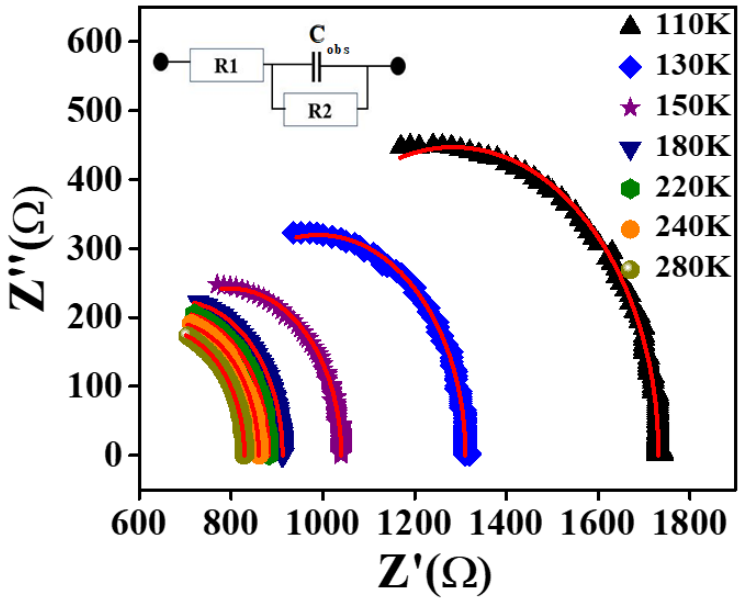

Figure 3.7. Cole-Cole plot of impedance data at few representative temperatures. The line through the data are fits to the Impedance data using a model equivalent circuit whose schematic is shown in the inset.

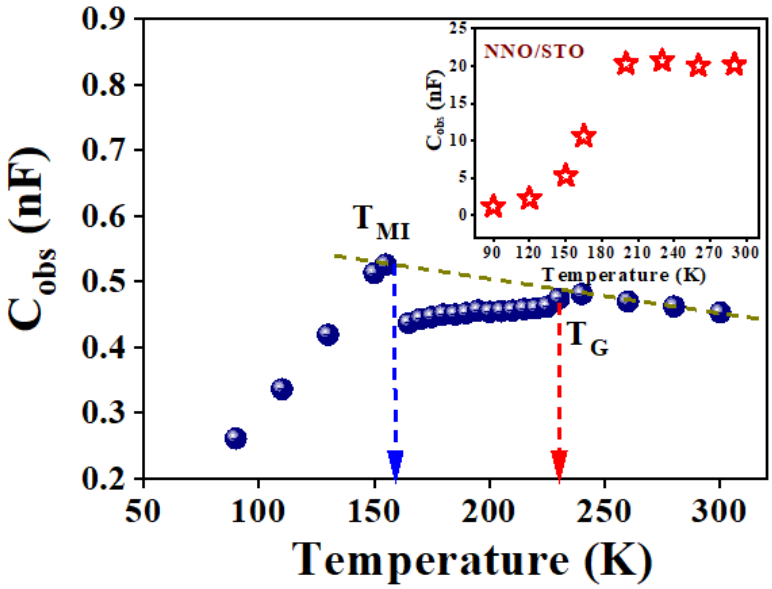

Figure 3.8. Temperature variation of the capacitance parameter $C_{obs}(T)$ of the NNO film grown on BTO/STO. The MI transition temperature T_{MI} and the temperature T_G observed in noise data are also marked. The dotted line is a simple extrapolation to show expected behaviour of $C_{obs}(T)$ in absence of a T_G. The inset shows the capacitance of the NNO film on STO.

The imaginary part of the impedance $Z^{"}$ has been plotted with the real part $Z^{'}$ at a given frequency for NNO film grown on BTO, at few representative temperatures in

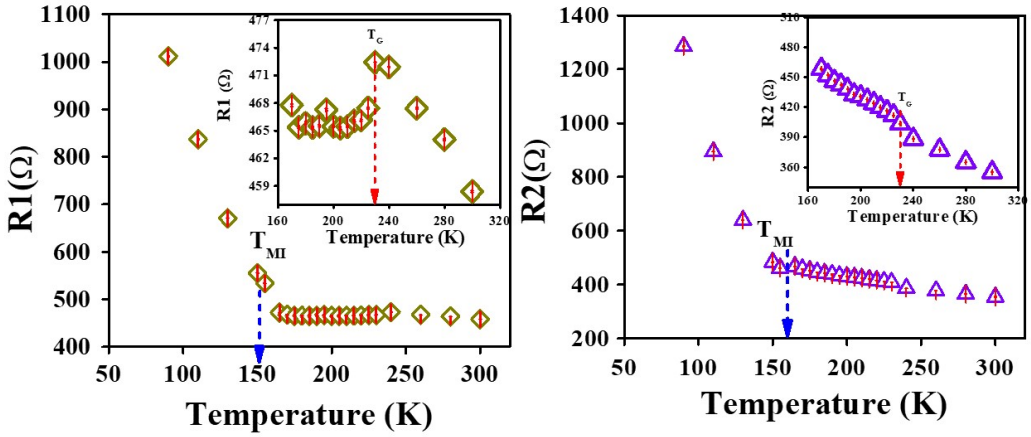

Figure 3.9. Temperature dependence of parameters R1 and R2. Inset shows data near T_G

between T_{MI} and T_G (Fig. 3.7) which is known as Cole-Cole or Nyquist plot. The lines through the data are fits using a simple phenomenological model equivalent circuit whose schematic is shown in the inset of Fig. 3.7. The model is a parallel combination of resistance $R2$ and C_{obs} in series with a resistance $R1$. We have used the software 'EIS spectrum analyzer'(EIS) to fit the impedance data to the phenomenological model. The EIS Spectrum Analyser is widely used stand alone program for analysis and simulation of impedance spectra. [33]. The software took as input a data file with observed impedance data for the Real(Z') and Imaginary part (Z") as a function of frequency. All three parameters (R1, R2, and Cobs) were automatically initialised, and several iterations were used to find the best match.The measurements of impedance were carried out in a planar geometry with the film.The equivalent capacitance in the film is represented by the $C_{obs}(T)$ which is temperature dependent (but frequency independent)in the model. The complex impedance data $Z(\omega,T)$, based on the simple model above, are given by the relation:

$$Z(\omega,T) = Z^{'} + iZ^{"} = R1 + \frac{R2(T)}{1 + j\omega R2(T)C_{obs}} \tag{4}$$

The resistances $R1$ and $R2$ as well as $C_{obs}(T)$ in the model above were presumptively free of explicit frequency dependency. The frequency independent $C_{obs}(T)$ corresponds to an average capacitance at a mean frequency $\omega_0(T)$ has been discussed later on in this section using a separate model with Eqn. 7 and 8. In Fig 3.8. the variation of $C_{obs}(T)$ is shown as a function of T , as obtained by fitting the impedance data. There is a noticeable break in the slope with a short peak at $T = T_G$ and a sharp leap is seen at $T \approx T_{MI}$.

The variation of parameters $R1$ and $R2$ with temperature shows in Fig. 3.9. Like in the fluctuation of $C_{obs}(T)$, the two separate temperatures T_{MI} and T_G are also clearly shown here. The coexistence of phases with different conductivities causes the capacitance at the transition zone, where charging of the conducting phase (isolated by the insulating phase) results in capacitance of the film.The relative volume proportion of the two phases

changes as a result of temperature variation, which causes the capacitance to be temperature dependent.The respective conductivities of the two phases affect the value of the capacitance, which in turn determines the interfacial charges in the region between the two phases. When the NNO film is grown on lattice-matched STO, the metallic phase has a significantly lower resistivity, which causes the relative difference between the two coexisting phases to be greater and the film's capacitance to be greater (see the inset data of Fig. 3.8). Contrarily, the high temperature phase in the NNO film produced on BTO is a poor metallic phase with a resistivity that is substantially higher due to strain relaxation and quenched disorder, as was previously mentioned.The distinct characteristic of the equivalent capacitance in this temperature range indicates the presence of coexisting phases with a different nature from both the metallic phase above T_G and the insulating phase below T_{MI}.

3.5.1 A.C Conductivity data

The A.C conductivity ($\sigma(\omega,T)$) was measured as a function of frequency $\omega = 2\pi f$ at different temperatures down to 80K. The data were taken in a planar configuration where the current is in plane of the film and are shown in Fig.3.10 (a). To estimate the frequency dependent part, the data in Fig.3.10(a) were fitted to the phenomenological relation:

$$\sigma(\omega,T) = \sigma(\omega = 0,T) + \sigma_\omega(T)\omega^{n(T)} \tag{5}$$

The A.C conductivity $\sigma(\omega,T)$ vs T data were fitted to Eqn.5 using non-linear least square fit. parameters $\sigma(\omega = 0,T)$, $\sigma_\omega(T)$ and the exponent $n(T)$ were taken as fit parameters.The value of $\sigma(\omega = 0,T)$ is determined by the fit which is $\approx \sigma_{dc}(T)$. We have identified the T_{MI} once again other than T dependent resistivity data from the variation of $\sigma_{dc}(T)$ in previous subsection. The frequency dependent conductivity data along with fitted line and temperature evolution of two important fitted parameters σ_ω, $n(T)$ are shown in Fig.3.10(b). The similar measurement and fitting has been carried out with NNO/STO single layer film (The data are given in Fig 3.14 (a),(b) to compare with NNO/BTO/STO sample. The data is given in the 'Additional data and information section'.

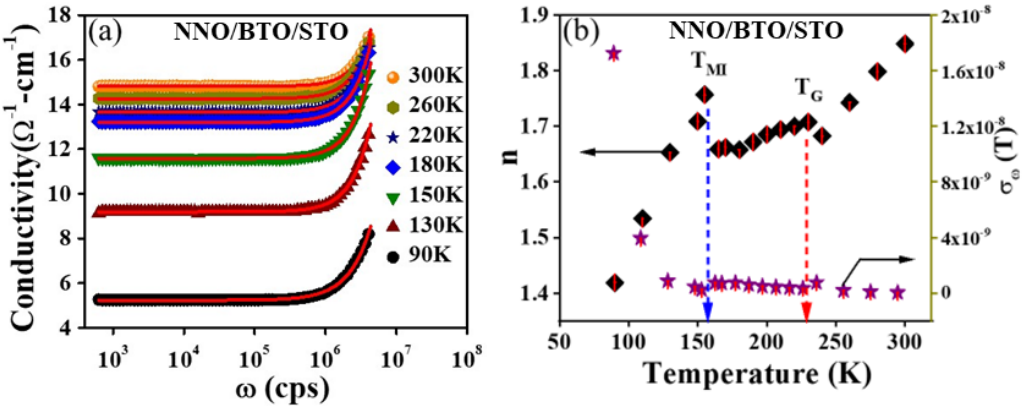

Figure 3.10. (a) A.C conductivity $\sigma(\omega,T)$ of the NNO film grown on BTO/STO as a function of frequency ω at few selected temperatures T. Fits to Eqn. 6 are shown as red line. (b) Variation of the exponent $n(T)$ and $\sigma_\omega(T)$ as a function of T for NNO film grown on BTO/STO. Two temperatures T_{MI} and T_G are marked by arrows.

The experimental conductivity data has been fitted nicely and found out the parameters for both the samples. The temperature dependency of these parameters amply demonstrates MIT temperature fingerprints. The variation in $n(T)$ with T can be appreciated as $T \to T_{MI}$. The $n(T)$ shows non-monotonous behavior in addition to the rise in the value of $n(T)$ at $T \approx T_{MI}$, there is a discernible feature at $T = T_G$ in the NNO/BTO/STO multi-layer. In this perspective, it will be interesting to compare the A.C conductivity data obtained on the NNO film formed on STO, which exhibits no abnormal features beyond the T_{MI} range. The parameters $n(T)$ for the film NNO/STO do not exhibit the abrupt changes found in NNO/BTO/STO above T_{MI}. The temperature dependency of $\sigma(\omega = 0,T)$ is the reverse of frequency dependent part, $\sigma_\omega(T)$, which is enhanced below T_{MI}. In low temperature insulating phase, this suggests a considerable increase in the relative contribution of the frequency dependent portion of ac conductivity.

We use a model of co-existing phases that includes a size distribution of metallic clusters to assess the A.C conductivity data.The model [34] had been proposed to understand that conductivity of a composite medium with co-existing insulating and metallic phases with a distribution of conducting region size (ξ) as happens close to a MI transition. In this model the frequency dependence arises as a consequence of the distribution in ξ. The length scale ξ of the conduction region determines the time scale of charge diffusion and hence the frequency dependence through the relation $\xi \approx \sqrt{D/\omega}$, where D is a typical mean carrier diffusivity. The total conductivity consisting of the dc conductivity and the frequency dependent part of the conductivity that consists of contribution from the conducting regions. This is given as [34] :

$$\sigma(\omega,T) = \sigma_{dc} + A(T)\int_0^{\omega} \frac{1}{(2\pi)^{1/2}\Sigma} exp(-\frac{(log\omega - log\omega_0)^2}{2\Sigma^2})d\omega \qquad (6)$$

Where the length scale has a log-normal distribution with broadening parameter Σ and most probable length scale ξ_0 that defines $\omega_0 = \frac{D}{\xi_0^2}$. The constant $A(T)$ contains mainly geometric factors. Both the parameters $\Sigma(T)$, $\omega_0(T)$ are temperature dependent. The smaller isolated metallic regions that cannot take part in charge transport would contribute to the capacitance which is given as-

$$C(\omega,T) = C_0(T)\int_{\omega}^{\infty} \frac{1}{(2\pi)^{1/2}\Sigma} exp(-\frac{(log\omega - log\omega_0)^2}{2\Sigma^2})d\omega \tag{7}$$

Where $C_0(T)$ is a frequency independent scale for the capacitance.

The task of derivation and extraction the value of C(ω, T) from eqn. (6)-(8) associates with a special integration which gives us the results in form of error function. The integration have been carried out in between ω to infinity by replacing the value in another variable, t i.e.,t = $\frac{log\omega - log\omega_0}{\Sigma}$. The eqn. (8) has been simplified as-

$$C(\omega,T) = C_0(T) \times \zeta; \zeta = \frac{1}{\sqrt{\pi}} exp(log\omega_0 + \frac{\Sigma^2}{2})[1 - erfp]; \quad p = \frac{\frac{log\omega - log\omega_0}{\Sigma} - \Sigma}{\sqrt{2}} \tag{8}$$

The frequency dependent ζ has been calculated and found out the value of $C(\omega,T)$ which is both frequency and temperature dependent.

The observed $\sigma(\omega,T)$ data were fitted to Eqn. 8 in order to derive the necessary parameters.The measured d.c resistivity $\sigma(\omega = 0,T) = \sigma_{dc}$ data Eqn. 7 has been used. The cluster's typical relaxation frequency $\omega_0(T)$ on average at each temperature T determines the scale for the AC conductivity's frequency-dependent component. The value of $\omega_0(T)$ was estimated from the observed frequency dependent part given as $\omega_0(T) \equiv (\frac{\sigma(\omega=0,T)}{\sigma_\omega(T)})(\frac{1}{n(T)})$, where these parameters were obtained directly from fit of the A.C conductivity data to Eqn. 8 discussed before. The parameters $A(T)$ and $\Sigma(T)$ were used as fit parameters for each T. On the MATLAB ® environment, the fitting was done utilising the least square fit tools that are already available. In the temperature evolution of $\omega_0(T)$, $A(T)$ and $\Sigma(T)$, the two distinct T are shown in Fig. 3.11 (a,b, c). The frequency dependent $\sigma(\omega,T)$ data and the fitted line obtained from Eqn. 7 are also given in Fig. 3.11 (d).

We have determined the frequency and temperature dependent capacitance $C(\omega,T)$ using Eqn. 8 which gives us the $C_{obs}(T)$ result in the form of a error function. The frequency independent constant $C_0(T)$ in Eqn. 8 was obtained by equating $C_{obs}(T)$ to $C(\omega_0,T)$ at each T. This assumes that $C_0(T)$ is an average capacitance at the mean frequency ω_0. Both the parameters $\Sigma(T)$, $\omega_0(T)$ used in calculation of $C(\omega,T)$ using eqn. 8 have been obtained from fit of the A.C conductivity data to Eqn. 7 as elaborated before.

The variation of $C(\omega,T)$ with frequency at different temperature are shown in Fig 3.12 (a). A contour plot of $C(\omega,T)$ obtained from Eqn. 8 is shown with the variation of both T and ω in Fig. 3.12 (b) which would be expected for a "composite" in the mixed phase region at the T range $T_{MI} < T < T_G$.

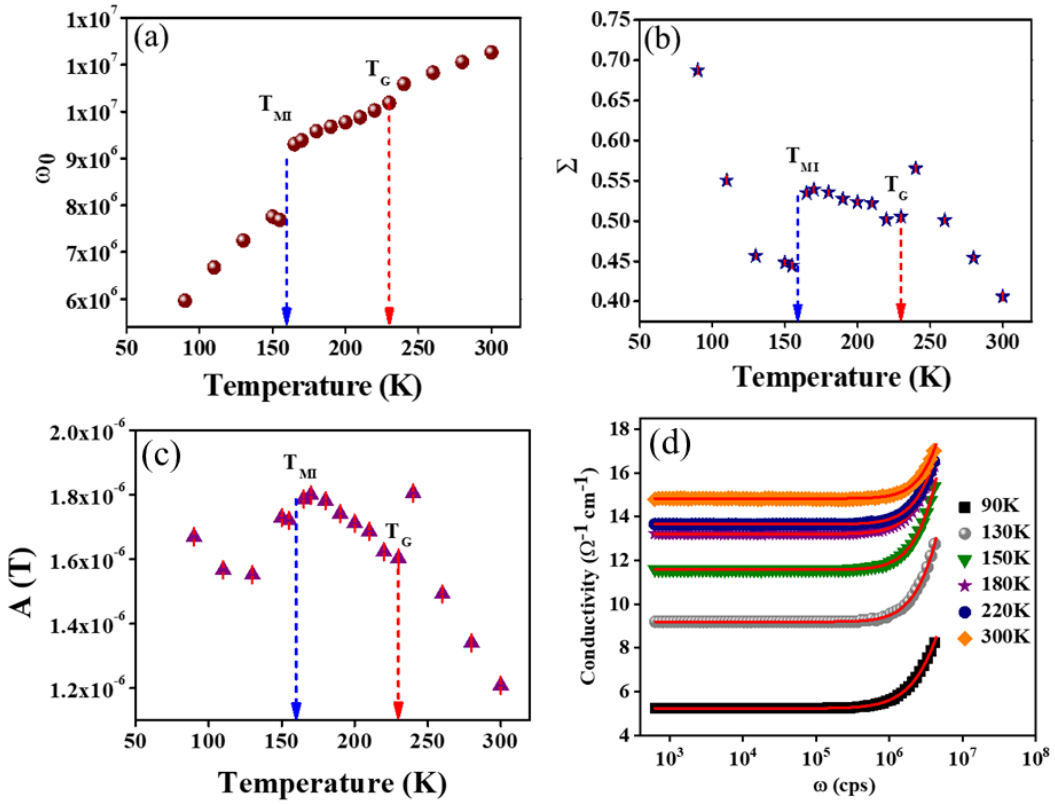

Figure 3.11. The temperature variation of parameters (a) $\omega_0(T)$ (b) $\Sigma(T)$ (c) $A(T)$. Two temperatures T_{MI} and T_G are marked by arrows.(d) The A.C conductivity $\sigma(\omega,T)$ data and fitted line with Eqn. 7 for some representative T.

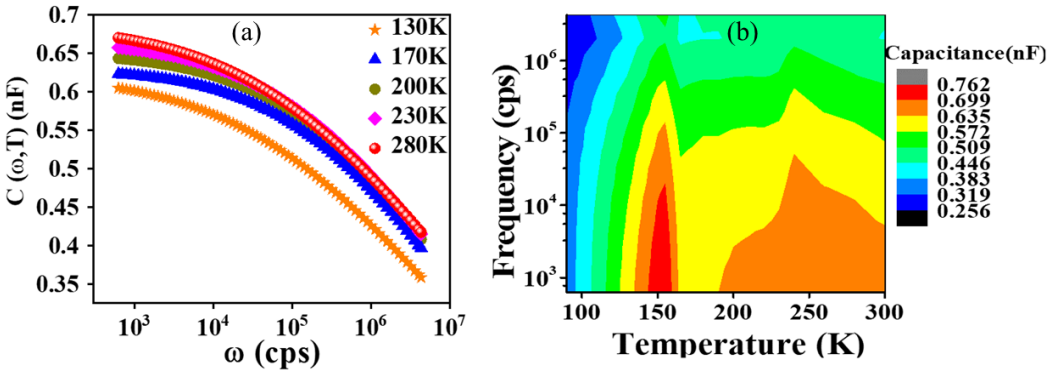

Figure 3.12. (a) The variation of $C(\omega,T)$ with ω at few representative T evaluated from eqn.8 (b) The A contour plot of $C(\omega,T)$ evaluated from Eqn.8

3.6 Discussion:

3.6.1 Broad M-I transition region

The diffused nature of the MIT (seen in Fig. 3.1) observed in NNO film grown on BTO/STO which shows anomalous features in Noise, Impedance spectroscopy data as well as in the A.C conductivity $\sigma(\omega,T)$, in the region of temperature $T_{MI} < T < T_G$. The anomalous behaviour of $n(T)$ in the said T region from Eqn. 6, reflects the nature of temperature evolution of phases [35] and contains information on the hopping character of the charge carriers through localised states. According to Mott's idea, transport through localised states in insulating systems can make $n \to 2$. In this thesis, the data matches the entire temperature range with an exponent n that is in the region $1 < n < 2$ and declines with cooling and exhibits anomalous characteristics at $T_{MI} < T < T_G$. We have elaborated in details the mixed phase region in $T_{MI} < T < T_G$ with the A.C conductivity model in the previous section. The evolution of $C(\omega,T)$ with both ω & T are shown as a contour plot (Fig. 3.12) which help in visualizing the evolution of the parameters.

3.6.2 Likely signature of Griffiths phase at T_G

We have identified a characteristic temperature T_G above T_{MI} which can be identified as the onset of electronic Griffiths phase. The system is like a composite of the high-temperature bad metallic phase and low-temperature insulating phase within temperature in between T_{MI} and T_G, which is very much similar to magnetic Griffiths phase. Where, disordered paramagnetic state coexists with a local ferromagnetically ordered phase below an onset temperature. Hence, small ferromagnetic clusters are embededed in the paramagnetic phase in magnetic Griffiths phase. (Several experiments have been conducted to understand the magnetic Griffiths phase, especially in doped rare-earth manganites that exhibit collosal magnetoresistance [6–12]).

The NNO films grown on BTO is not coherently strained but strain relaxed with residual strain $\epsilon_{\parallel}(\%) \approx -0.59\%$. Misfit dislocations would result from strain relaxation in NNO. Inhomogeneity in the strain is caused by the presence of grains in the films (with grain boundaries) as seen in Fig. 2.8.(c) The Griffiths phase needs the coexistence of phases, the film under study also shows coexistence of phases near the transition zone. In the temperature region around T_G the insulating phase is the minority phase with phase fraction $f_i \ll 1$. Thus, small pockets of metallic phase embedded in the minority insulting phases will be very rare and will occur over a small temperature region between T_G and T_{MI}. Theoretical investigations established that these rare regions can control the long-time dynamics in a Griffiths phase. As a result, the fluctuation's auto-correlation function $\phi(t)$ primarily contributes at low frequencies. In Fig. 3.5 (b), a long-time tail has been observed in the variation of auto-correlation function $\phi(t)$ which has been fitted with Eqn. 3 in the previous subsection 3.4.1. Strong evidence is given in favour of the idea that the temperature T_G is comparable to the Griffiths phase initiation temperature as seen in magnetic phase

transitions by the notion of the existence of sparse phase, The sparse phase will lead to slow relaxation kinetics as has been observed experimentally.

3.7 Conclusion:

The NNO film exhibits a Mott type metal-insulator transition from a high temperature bad metallic phase with high value of resistance = 70 milliohm.cm (at 300K) and a negative TCR to a low temperature insulating phase at a temperature $T_{MI} = 160K$ when grown on a substrate BTO/STO (with large mismatch of lattice constant). The undesirable metallic phase is comparable to what is anticipated in an oxide with quenched disorder near the Anderson transition.When the films are prepared on crystalline substrates like LAO, STO that have better matching with lattice constants, such a poor metallic phase is not found in NNO. When disorder is present, the metal-insulator transition has a percolative nature with coexisting phases both near and far from the transition zone, resulting in a wide transition.

It has been proved that in addition to the MIT at temperature T_{MI}, a new characteristic temperature T_G above T_{MI} signals the beginning of a temperature region $T_{MI} < T < T_G$, where new features are observed, using noise spectroscopy and impedance spectroscopy, which probe the dynamics of the coexisting phases.It is proposed that for the Mott transition with disorder, the temperature T_G marks the onset of an electronic Griffiths phase that has been theoretically proposed for Mott transitions with disorder. The experiment thus provides evidence of such a phase; Griffith phase in an oxide system which undergoes a Mott transition.

3.8 Additional data and information

A. Rocking XRD used to calculate the Dislocation density

The value of the FWHM is large and points to significant strain inhomogenity in the film that would arise from quenched disorder. Thus, in the NNO film on BTO there is quenched disorder which has been roughly estimated from the dislocation density (DD) per unit cm using the formulae-

$$DD = \frac{\beta^2}{9b^2} \tag{9}$$

Where β, and b are the FWHM and burger vector calculated from NNO (200) peak.The calculated value of DD is 9.72 $\times 10^{10}$ per cm which is a sufficiently large value to influence the M-I transition in NNO.

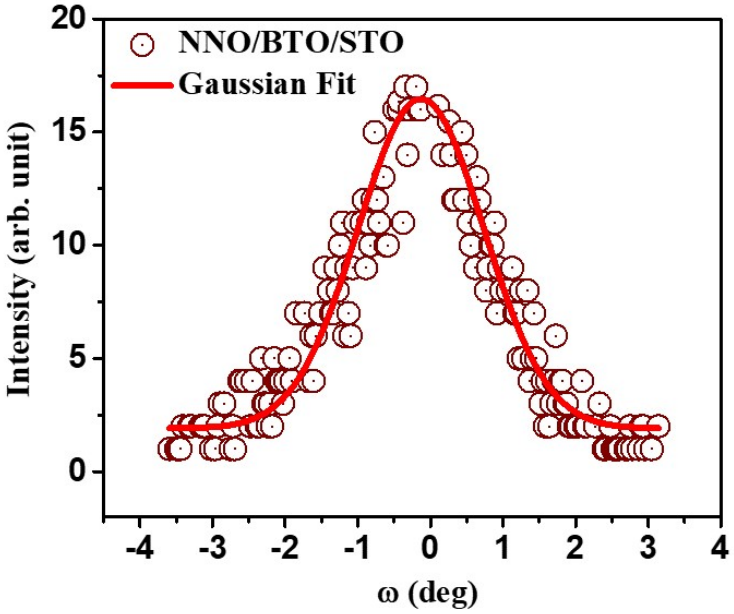

Figure 3.13. Rocking XRD of NNO layer with Gauss fit

B. A.C conductivity data of NNO/STO

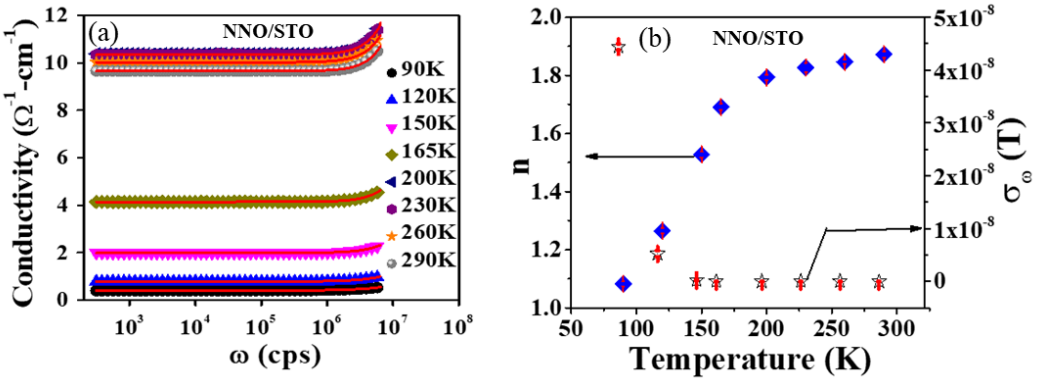

Figure 3.14. (a) A.C conductivity $\sigma(\omega,T)$ of the NNO film grown on STO as a function of frequency ω at few selected temperatures T. Fits to Eqn. 6 are shown as red line. (b) Variation of the exponent $n(T)$ and $\sigma_\omega(T)$ as a function of T for NNO film grown on STO. Two temperatures T_{MI} and T_G are marked by arrows.

References

[1] S. Middey, J. Chakhalian, P. Mahadevan, J. W. Freeland, A. J. Millis, and D. D. Sarma, Annual. Rev. Mater. Res. 46, 305 (2016)

[2] R. S. Bisht, S. Samanta, and A. K. Raychaudhuri, Phys. Rev. B 95, 115147 (2017)).

[3] S. Catalano, M. Gibert, J. Fowlie, J. Íñiguez, J. M. Triscone and J. Kreise, Rep. Prog. Phys. 81, 046501 (2018).

[4] Y. Kumar, R. J. Choudhary, A. P. Singh, G. Anjum, and R. Kumar, J. Appl. Phys. 108, 083706 (2010).

[5] R. S. Bisht, S. Chatterjee, S. Raha, A. Singha, D. Kabiraj, D. Kanjilal, and A. K. Raychaudhuri, Phys. Rev. B 105, 205120 (2022)

[6] J, Burgy, M. Mayr, V. Martin-Mayor, A. Moreo, E. Dagotto, Phys. Rev. Lett. 87, 277202 (2001)

[7] M. B. Salamon , P. Lin and S. H. Chun, Phys. Rev. Letts 88, 197203 (2002)

[8] J. Deisenhofer et., al Phys. Rev. Letts 95, 257202 (2005)

[9] V. N. Krivoruchko, Y. Melikhov and D. C. Jiles, Phys. Rev. B 77, 1804069R) (2008))

[10] R. D. Merithew, M. B. Weissman, F. M. Hess, P. Spradling, E. R.Nowak, J. O'Donnell, J. N. Eckstein, Y. Tokura, and Y. Tomioka, Phys. Rev. Lett. 84, 3442 (2000)

[11] R. H. Heffner, J. E. Sonier, D. E. MacLaughlin, G. J. Nieuwenhuys, G. Ehlers, F. Mezei, S.-W. Cheong, J. S. Gardner, and H.Röder, Phys. Rev. Lett. 85, 3285 (2000).

[12] V. N. Krivoruchko,1 M. A. Marchenko,1 and Y. Melikhov, Phys. Rev. B 82, 064419 (2010).

[13] V. Dobrosavljević and G. Kotliar, Phys. Rev. Letts 78, 3943 (1997),

[14] M. C. O. Aguiar, V. Dobrosavljević, E. Abrahams, and G. Kotliar, Phys. Rev. B 71, 205115 (2005)

[15] E. C. Andrade, E. Miranda, and V. Dobrosavljević, Phys.Rev. Lett. 102, 206403 (2009),

[16] V. Dobrosavljević, N. Trivedi, and J. M. Valles, Conductor-Insulator Quantum Phase Transitions (Oxford University Press, Oxford, 2012))

[17] D. Tanaskovic, E. Miranda, V. Dobrosavljevic, Phys. Rev. B 70, 205108 (2004).

[18] T. Vojta, AIP Conference Proceedings 1550, 188 (2013)

[19] R. Yamamoto , T. Furukawa , K. Miyagawa ,T. Sasaki, K. Kanoda and T. Itou, Phys. Rev. Letts 124, 046404 (2020).

[20] P. Majhi, S. Chatterjee, R. Singh Bisht, V. R. Reddy, B. Ghosh, and A. K. Raychaudhuri Phy. Rev. Matt 5, 085005 (2021)

[21] J. Liu, M. Kareev, Gray, J. W. Kim, P. Ryan, B. Dabrowski, J. W. Freeland, and J.Chakhalian Appl. Phys. Lett. 96, 233110 (2010).

[22] E. Mikheev, A. J. Hauser, B. Himmetoglu, N. E. Moreno, A. Janotti, C. G. Van de Walle, and S. Stemmer, Sci. Adv. 1, e1500797 (2015).

[23] A.K. Raychaudhuri , Advances in Physics 44, 21 (1995)

[24] X. Granados, J. Fontcuberta, X. Obradors and J. B.Torrance, Phys. Rev. B 46, 15683 (1992)

[25] D. Kumar, K. P. Rajeev, J. A. Alonso and M. J. Mart´ınez-Lope, J. Phys.: Condens. Matter, 31, 145603 (2019)

[26] D.S. McLachlan, J.Phys C: Solid State Phys. 20, 865 (1987).

[27] A. Sahoo, S. D. Ha, S. Ramanathan, and A. Ghosh, Phys. Rev. B 90, 085116 (2014).

[28] A. M. Alsaqqa, S. Singh, S. Middey, M. Kareev, J. Chakhalian, and G. Sambandamurthy, Phys. Rev. B 95, 125132 (2017).

[29] G. N. Daptary, S. Kumar, M. Kareev, J. Chakhalian, Aveek Bid, and S. Middey, Phys. Rev. B 100, 125105 (2019).

[30] A. K. Raychaudhuri, Curr. Opin. Solid State Mater. Sci. 6, 67 (2002).

[31] P. Dutta and P.M Horn, Rev. Mod. Phys. 53, 497 (1981).

[32] S. Samanta, A. K. Raychaudhuri, X. Zhong, and A. Gupta, Phys. Rev. B 92, 195125 (2015).

[33] Source of EIS :http://www.abc.chemistry.bsu.by/vi/analyser/

[34] A. N. Papathanassiou, I. Sakellis, and J. Grammatikakis , Appl. Phys. Lett. 91, 122911 (2007).

[35] P. Lunkenheimer and A. Loidl, Phys. Rev. Letts 91, 207601 (2003).

Chapter 4

Phase co-existence, super-cooling and resistance relaxation kinetics in $NdNiO_3$ films below the M-I Transition temperature

Abstract: *In correlated oxides undergoing temperature driven Mott-like MI transition, the co-existence of electrically different phases below the metal-insulator (MI) transition temperature (T_{MI}) has been found in a variety of systems, including $NdNiO_3$ (NNO). In both bulk and thin film forms, pristine NNO materials exhibit phase coexistence and sluggish dynamics below T_{MI} down to low temperatutes well below T_{MI}. In this chapter, we have reported an extensive investigation on relaxation of co-existing phases below the metal-insulator transition in well characterized films of grown on three different crystalline substrates.One aspect of the coexisting phases is that as the temperature is dropped below T_{MI}, the metastable high temperature metallic phase transforms into the stable insulating phases with a finite relaxation time. We have carried out an exclusive experimental investigation using resistivity as a tool where the ramp dependent hystersis and isothermal annealing induced resistivity relaxation were studied. The isothermal annealing experiment done on several temperatures,$T_a << T_{MI}$ which reveals the temperature evolution of average relaxation time $< \tau >$. The $< \tau >$ decreases on cooling pointing to a temperature dependent barrier to relaxation, where the barrier reduces continuously on cooling down to a temperature T^* and the relaxation time $\rightarrow 0$ at this temperature. We identified T^* as limit of supercooling. A model based simulation by Monte Carlo technique has been done to analyze the experimental observations (both hysteresis and isothermal annealing) with a minimal set of parameters, namely, a temperature T^* and an energy scale of transformation E^*. The parameters used in the simulation and other experimentally observed quantities like average relaxation time $< \tau >$ and its temperature dependence were found to be correlated with certain structural parameters, in particular, the crystallite grain size that determine the size range in these films.*

4.1 Introduction

Metal-insulator transition (MIT) as it happens in a correlated system is a fascinating phenomena. This phenomena have been studied in correlated oxides like V_2O_3, VO_2, $NdNiO_3$, $PrNiO_3$ for example, where a temperature driven MIT occurs (like a Mott transition) on cooling from a high temperature metallic phase to a low temperature insulating phase. The transition is often first order and is accompanied by hysteresis. In such MIT even in presence of some degree of disorder, the underlying first order nature of the transition leads to phase coexistence.

The occurrence of phase-coexistence near the MIT and the associated physics have been investigated for some time in different oxide systems undergoing MIT. In recent years the issue of the electronic phase separation and phase-coexistence have again attracted renewed attentions, due to sustained theoretical developments as well as due to innovative use of different types of direct imaging techniques like Scanning Tunneling Microscopy and Spectroscopy (STM/STS) with near atomic level resolution and spatially resolved infrared imaging including near field imaging with spatial resolution $\approx$ 25nm [1–4]. There are a number of important outcomes from these experiments. For instance, it has been established that the coexisting phases indeed have different electronic signatures and their density of states near the Fermi level ($N(E_F)$) show clear signatures of both correlated metallic and insulating phases. It has been observed that there is persistence of the high temperature metallicity within the insulating phase below the MIT [4, 5].The scale of phase separation is in the nanoscopic to mesoscopic regime and the size scale along with volume fraction of the coexistence phases vary with temperature.This leads to an aspect of percolation that determines the outcome of the experiments.

A particular mention be made of the recent near-field imaging of the MIT in 300nm oriented V_2O_3 film [2]. It has been observed that the underlying structural transition at MIT directs the correlation driven electronic transition. Both the structural (ξ_{struc}) as well as the electronic (ξ_{elecn}) correlations lengths grow from nanoscopic scales to mesoscpoic scale (fraction of a micron to a micron), close to the transition. We propose to investiagate in this paper a closely related issue. The existence of such a length scale near the transition can get affected by the morphology of a film grown on a substrate, such as the size of coherent crystallographic regions. This may affect the kinetics of relaxation below the metal-insulator transition temperature (T_{MI}). This issue has been studied in the present investigation.

In addition to direct imaging methods as mentioned before, experiments of "bulk" nature, that probe the kinetics and dynamics associated with the co-existing phases, can observe clear signatures of the nanoscopic phase separation. As an example, appearance of large thermal noise (much larger than the anticipated Nyquist Noise) [6] near the T_{MI} has been traced to nanoscopic phase separation. The phase separation also leads to onset of slow electronic relaxation , which can give rise to electronic Griffiths phase as observed in

Polymeric systems and also in Oxides [7, 8].

The phase co-existence has important consequences, in particular, when kinetics of co-existing phases are considered near and below T_{MI}. In the phase coexistence region below T_{MI}, the persistence of the high temperature metallic phase in the low temperature insulating phase creates a metastable condition [9], because the high temperature metallic phase is not an equilibrium phase and can relax to the equilibrium insulating phase with a finite relaxation time. Cooling further below T_{MI} will change the relative volume fractions of the two phases, but there is a likelihood of presence of a finite volume fraction the high T phase , although the volume fraction may be small. As a result, at a given temperature a fraction of the metastable state will be transformed to the equilibrium state with a finite time associated with the kinetics of transformation. The consequence of this will be hysteretic cooling and heating curves at a finite rate of cooling and heating . The presence of the metastable high temperature phase would also lead to an evolving time dependent volume fraction when an isothermal anneal is done at a temperature below T_{MI} after cooling at a given rate.The discussion above have been done in the general context of a temperature driven MIT which is expected to have a broad validity in all such systems undergoing MIT. However, details of each material undergoing MIT would have contributions that are materials specific. In this chapter, we report an extensive investigation of kinetics of relaxation in the system NNO which has shows a clear MIT [5] and shows phase co-existence below T_{MI}.

It has been established in previous investigations [10] that the resistance relaxation method is a viable method to study relaxation kinetics of co-existing phases because, the co-existing phases have different resistivities (ρ) or conductivities (σ). The conductivity of a solid with co-existing phases is like that of a composite medium where the volume fractions of the two phases determine the resulting conductivity and this can be quantified by an effective medium theory [11].The volume fraction of the two co-existing phases in such a solid with metastable phase will change on isothermal anneling below the T_{MI}. This changing volume fraction will show up as a time dependent conductivity (or resistivity) of the solid undergoing an isothermal annealing below T_{MI}.

Presence of the metastable metallic phase below T_{MI} also gives rise to hysteresis when the temperature is cycled above and below the T_{MI} with a finite rate of heating and cooling ($\frac{dT}{dt}$) due to finite relaxation time $<\tau>$ of the metallic phase. When the solid undergoes cooling/heating at a finite rate , if the rate $\frac{dT}{dt}$ is too fast compared to relaxation rate ($\frac{1}{<\tau>}$), then there will be unrelaxed high temperature phase during cooling co-existing with the equilibrium phase. On heating , the growth of the volume fraction of the metallic phase, will follow a different path due to the presence of the unrelaxed phase . This will give rise to a rate dependent hysteretic resistivity vs T curve. Quantitative analysis of resistivity data for both the isothermal annealing and rate dependent hysteresis will identify the relevant parameters that control the relaxation process. In this investigation we have carried out a physical model dependent Monte Carlo simulation with a set of

parameters, that can quantitatively describe both the hysteresis as well as isothermal kinetics.

We have carried out a detailed investigation on the kinetics associated with phase coexistence and relaxation below T_{MI} in NNO film grown on three different kinds of substrates that results in different structural features (as revealed through temperature dependent X-Ray diffraction (XRD), and morphology (as revealed through Atomic Force Micorscopy). These factors, as we show below have clear effects on the relaxation kinetics. This is likely a first evidence that the phase co-existence in such MIT can indeed be controlled by structural factors. We have chosen three substrates $LaAlO_3(LAO)$, $SrTiO_3(STO)$, $BaTiO_3(BTO)$ to grow the films.

It is noted that resistance relaxation experiments under isothermal annealing below T_{MI} have been carried out on bulk pellets of PNO [9] and NNO [10] which indicates existence of slow kinetics.However, these experiments did not have any structural characterizations that allow one to connect the structural parameters and the relaxation kinetics.

4.2 Experimental

The Pulse Laser Deposition (PLD) system with KrF laser ($\lambda = 248nm$) has been used to grow the NNO films on three different substrates namely $SrTiO_3(STO)$, $LaAlO_3(LAO)$and $BaTiO_3/SrTiO_3(BTO/STO)$ with uniform growth conditions.A well characterized NNO pellet has been used as the target material. The deposition has been carried out at temperature 675^oC with base chamber pressure 10^6 mbar, and oxygen pressure of 0.2 mbar during deposition. After depositing each films oxygen annealing has been done for 1 hr at 1 atm oxygen. pressure to maintain its proper stoichiometry. The details of the film deposition process as well as characterizations are given in Chapter-2.

The electrical resistivity measurements have been carried out using a low temperature cryocooler system (Model-Coldedge) down to 10 K connected with a suitable LabView programme (discussed detail in Chapter-2 and appendix 2) which is able to record temperature and time dependent resistivity data. The time and temperature dependent resistivity data have been recorded to study the kinetics. We have covered a range of uniform heating/cooling ramp rate starting from 0.2 K/min to 15 K/min to take the resistivity data when the temperature is cycled across the transition region. For the low temperature kinetics measurement for an isothermal anneal, samples were cooled to the desired anneal temperature $T_a(< T_{MI})$, where it was held for at least 2 hrs. of relaxation experiment was found to cover more than 5-13 time constants even in slowest relaxation process. After completed the heating cycle we have waited 1 hr. at 300 K to nullify the previous memory.

4.3 Structural Data

4.3.1 Room temperature characterization of the films

The Fig. 4.1(a, b, c) shows the XRD data of the NNO films grown on LAO, STO and BTO/STO substrates. The XRD data show highly oriented film growth along the (001) crystallographic direction. We have chosen these substrates to grow the films because the film growth and texture have been varied among them. The films are differing from each other on the basis to their growth texture, strain, morphology (grain), and order of dislocation density present with in the systems. In Fig. 4.1, the AFM images of the film's top surface reveals the films are highly compact with various grain size (Fig. 4.14, 'Additional data and information' section) and surface roughness. The films are mostly strain relaxed(established through Reciprocal Space Mapping) as discussed in Chapter-2, but have a built-in residual strain. Granular morphology and misfit dislocations are produced as a result of strain relaxation. It is anticipated that these structural characteristics will play a significant role in the kinetics of phase change. The parameters related to sample characteristics are put in the table-I.

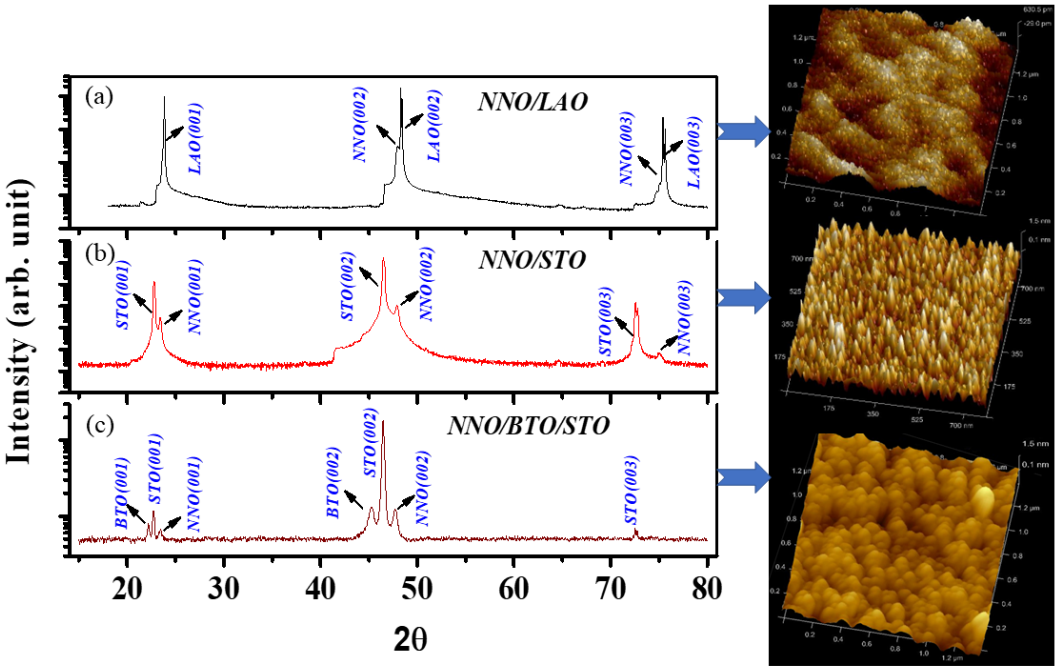

Figure 4.1. The XRD data of NNO films along (001) crystallographic direction grown on (a) LAO (b)STO (c) BTO/STO. The AFM images of the top surfaces of the films are given in parallel arrow accordingly.

4.3.2 Temperature evolution of lattice constants in the films

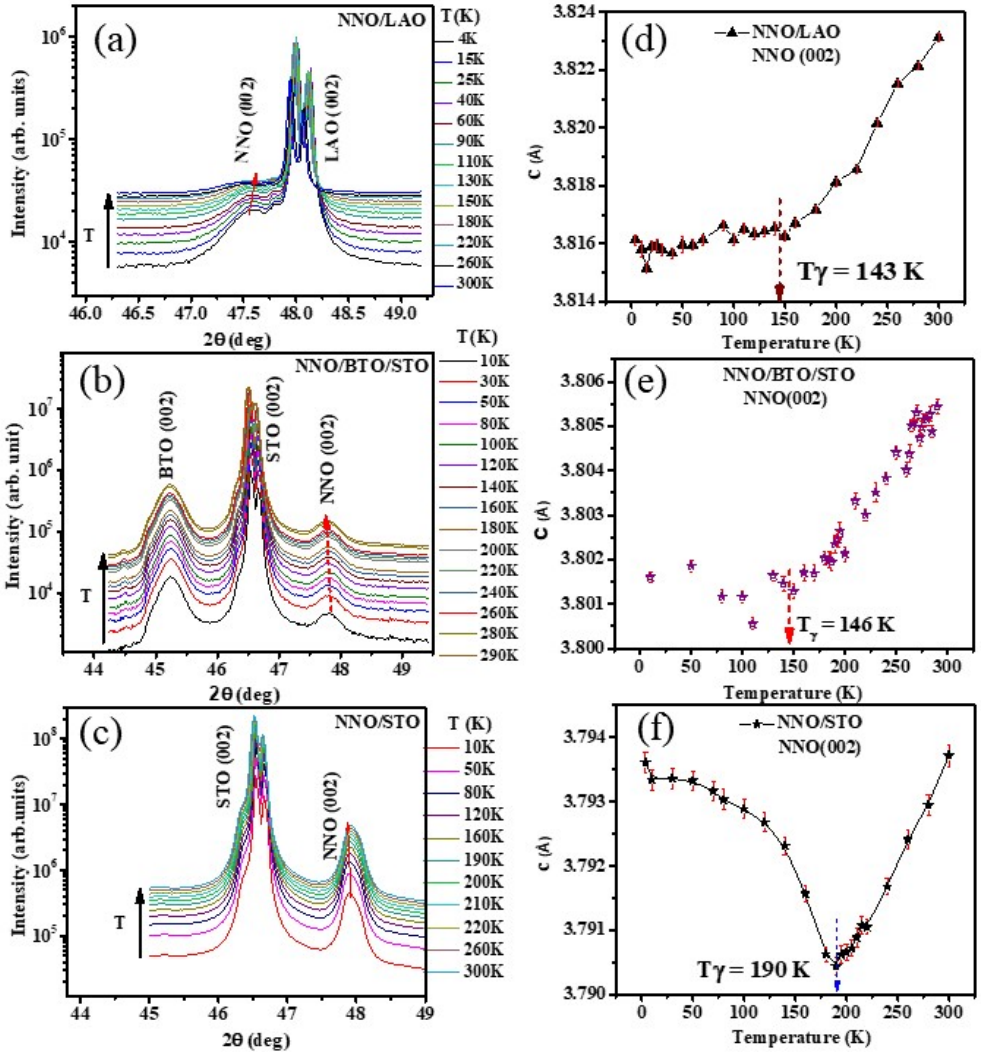

Figure 4.2. The T dependent XRD data of NNO films grown on (a) LAO (b) BTO/STO (c) STO. The temperature dependence of the out-of-plane lattice constant c are shown in Figures (d) NNO/LAO (e) NNO/BTO/STO and (f) NNO/STO . The temperature dependence of c indicate the structural transitions at the marked temperatures

The development of (002) peak region of each film has been observed with temperature in Fig. 4.2 (a, b, c). We have looked at how the films' lattice constants have changed over temperature using temperature dependent XRD. Data were taken during heating cycle with temperature stabilized at each point to within $5mK$ for at least 15 minutes (details are in Chapter-2). Shift of the peak positions of the $NdNiO_3$ (002) reflection as well as the substrate (002) reflections have been observed with T as shown in Fig. 4.2 (d, e, f) for NNO/LAO, NNO/STO and NNO/BTO/STO respectively. The XRD peak (002) position

has been obtained by peak-fit and the out-of-plane lattice constants **c** were obtained.

The $NdNiO_3$ exhibits insulator to metal phase transition which is associated with change in symmetry from low temperature monoclinic to high temperature orthorhombic structural transformation when warmed up through T_{MI} [12]. The lattice constant shows the clear change of slope in the variation at $T = T_\gamma$ which is very close the T_{MI} of the respective films. The temperature at the slope's intersection is described as T_γ and $\frac{T_\gamma}{T_{MH}} = 1 \pm 0.03$. The transition in NNO/STO is very sharp and there is a sharp-up turn of **c** below T_γ as marked where as similar type of lattice constant evolution is observed in other two samples. From the Fig, we see NNO/STO film has the smallest out-of-plane lattice constant and hence largest in-plane lattice constant giving rise to a tensile strain that stabilizes the insulating phase leading to the highest T_{MI} among the the three films. For the other two films, the in-plane lattice constants lead to residual compressive strain. The local symmetry change (local crystal structure) is strongly guided by transformation of the high T metallic phase (orthorhombic symmetry) into low temperature insulating phase (monoclinic) below T_{MI}.

Table 1. Structural parameters of the films

Sample	$< d >$	$r_A(nm)$	DD(cm^{-2})	$\epsilon_\parallel(\%)$	R (%)	T_γ(K)	$\frac{T_\gamma}{<T_{MI}>}$
NNO/LAO	189 ± 3	0.2	2.31×10^8	-0.89	0.99	143	1.02
NNO/BTO/STO	40.5 ± 0.5	1.6	9.72×10^{10}	-0.59	1.1	146	1
NNO/STO	22.3 ± 0.3	0.4	3.58×10^8	0.094	0.96	190	0.97

$< d >$ - Average grain size, r_A-Average roughness, DD-Dislocation density, R- Relaxation, $\epsilon_\parallel$ is in-plane strain

4.4 Ramp dependent hysteretic resistivity data

The temperature dependent resistivity measurements have been carried out with several uniform ramp rate ($\frac{dT}{dt}$) of cooling and heating starting from 0.2 K/min to 15 K/min in the temperature range 10K to 300 K with the samples (Fig. 4.3).The hysteritic character of resistivity data is one of the key indicators of metastability and relaxation at $T < T_{MI}$. The path of the resistivity which it traverses from 300 K to 9 K (during cooling) and from 9 K to 300 K (during heating) separates out due to to the hysteresis. The kinetics of the high temperature metallic phase's relaxation below T_{MI} are connected by the change in the area of the hysteresis curves when the ramp rate is changed.

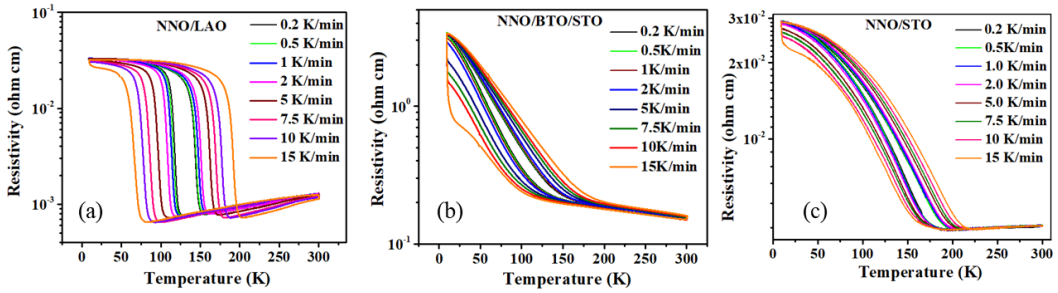

Figure 4.3. The ramp dependent resistivity data in the temperature range 10 K to 300 K of (a) NNO/LAO (b) NNO/BTO/STO (c) NNO/STO film

The resistivity curves get modified when the ramp-rate is varied, where the T_{MI} has been shifted to lower (upper) temperature for cooling (heating) cycle with the appearance of large hysteresis area. The shift in T_{MI} as a function of ramp rate for both heating and cooling cycles are shown in Fig. 4.4. It can be seen that the T_{MI} and area of hysteresis get significantly modified by the variation of ramp rate. T_{MI} shifts to lower (higher) temperatures for cooling (heating) cycle when the ramp rate is enhanced. The data also show that the values of the transition temperatures T_{MI} as well as the areas under the hysteresis curves for the resistivities have a strong dependence on the substrate on which the films are grown. The higher ramp rate increases the separation of the resistivities during heating and cooling thus enhancing the height of the hysteresis curve. We have quantified two parameters of hysteresis curve, namely, scaled height of hysteresis i.e. $\xi(T =< T_{MI} >)$ at average phase transition temperature, $< T_{MI} >$ and width of hysteresis i.e. ΔT_{MI}. These parameters are defined below:

$$\Delta T_{MI} = T_{MI,H} - T_{MI,C} \tag{1}$$

$$\begin{aligned} < T_{MI} >&= \frac{T_{MI,H} + T_{MI,C}}{2} \\ < \rho(T) >&= \frac{\rho_H(T) + \rho_C(T)}{2} \end{aligned} \tag{2}$$

$$\begin{aligned} \Delta\rho(T =< T_{MI} >) &= \rho_H(T) - \rho_C(T) \\ \xi(T =< T_{MI} >) &= \frac{\Delta\rho(T =< T_{MI} >)}{< \rho(T =< T_{MI} >) >} \end{aligned} \tag{3}$$

Heating and cooling cycles are denoted by the letters H and C in the subscript respectively. The $< T_{MI} >$ and $< \rho(T) >$ are the average transition temperature and average resistivity at a given T respectively. Both the parameters, ΔT_{MI} and $\xi(T =< T_{MI} >)$ mentioned in the Eqn. (1) and (3), are positive throughout and are enhanced with increasing of ramp rate.

A nearly rectangular shaped hysteresis area with largest width of the hysteresis is observed in NNO/LAO. The hysteresis area enhancement is comparatively less with ramp rate for the film NNO/STO (Fig. 4.3(c)). In NNO/BTO/STO a broad and diffused M-I

transition has been observed with gradually increasing hysteresis area with ramp rate. A poor or marginal type metallic zone with a negative temperature coefficient(TCR) of resistivity exists at high temperatures over T_{MI} where as contrast positive TCR observed in both NNO/LAO and NNO/STO films.

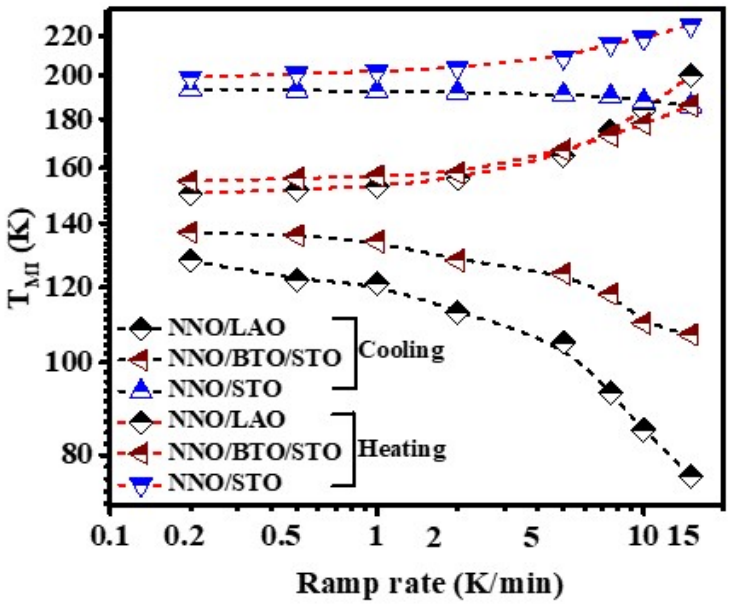

Figure 4.4. The variations of T_{MI} with ramp rate for NNO/LAO, NNO/BTO/STO and NNO/STO obtained from ramp dependent hysteresis data, Fig. 4.3

The derived parameters from ramp dependent hysteresis curve for the three film samples are shown in Fig 4.4 and 4.5.(a, b). The shift in T_{MI} as a function of ramp rate for both heating and cooling cycles for individuals sample are shown in Fig. 4.4.The noticeable change in the value of T_{MI} is observed for NNO/LAO whereas lesser change reported for NNO/STO.The moderate change in hysteresis area and T_{MI} observed for $NNO/BTO/STO$ film. The ΔT_{MI} as well as the scaled height ξ vary in the films in the order of $NNO/LAO > NNO/BTO/STO > NNO/STO$. There hysteresis curves close at both temperature ends for NNO/LAO but not for films grown on STO and BTO/STO. This aspect is linked to resistivity relaxation at $T < T_{MI}$, as will be described later on

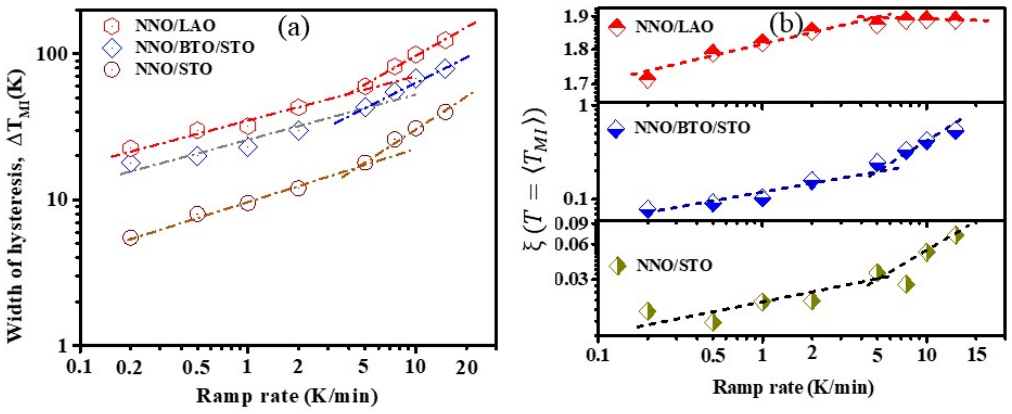

Figure 4.5. The variations (a) width of hysteresis(ΔT_{MI}) (b) scaled height of hysteresis (ξ) with ramp rate for NNO/LAO, NNO/BTO/STO and NNO/STO obtained from ramp dependent hysteresis data, Fig. 4.3

We have observed the variation of ΔT_{MI} as well as that of the scaled height of hysteresis $\xi(T =< T_{MI} >)$ with ramp rate as (see Fig. 4.5 (a) and (b)) which show a power law dependence of both the parameters with ramp rate so that $\Delta T_{MI} \propto (\frac{dT}{dt})^m$ and $\xi(T =< T_{MI} > \propto (\frac{dT}{dt})^n$. An additional factor that enhances the size of the hysteresis curves is the break in slope in both sets of curves with values of m and n at a ramp rate of 5 K/min.

Table 2. Parameters linked to hysteresis at ramp rate 5 K/min

Sample	$T_{MI,H}$ (K)	$T_{MI,C}$ (K)	ΔT_{MI} (K)	ξ	$\tau(T^*)$ (min)	ρ at 300K (Ohm-cm)	ρ at 10K (Ohm-cm)
NNO/LAO	165	105	60	1.874	0.11	1.3×10^{-3}	3.3×10^{-2}
NNO/BTO/STO	167	124	43	0.245	0.06	1.5×10^{-1}	3.3×10^{0}
NNO/STO	209	191	18	0.034	0.09	4.6×10^{-3}	2.9×10^{-2}

4.5 Observation of kinetics of resistivity relaxation during isothermal annealing

The kinetics of relaxation of the metastable high temperature metallic phase to the low temperature equilibrium insulating phase below T_{MI} during cooling cycle is an important part of this study. The time dependent resistivity data have been collected in isothermal condition by fixing the temperature at various annealing temperatures T_a, where $T_a \leq T_{MI}$ in the cooling cycle following a uniform rate of cooling at 5 K/min from starting temperature $T > T_{MI}$.This is an isothermal anneal where temperature is kept constant at T_a. We applied an isothermal anneal time t_a=2 hr for all the cases at different T_a. Following the anneal the sample was heated back upto room temperature and annealed at RT for a time t_{RT}= 1 hr. This is followed by the next cooling cycle. The cyclic heating and cooling curves with

different isothermal anneal temperature (T_a) for all the 3 samples are shown in Fig. 4.6

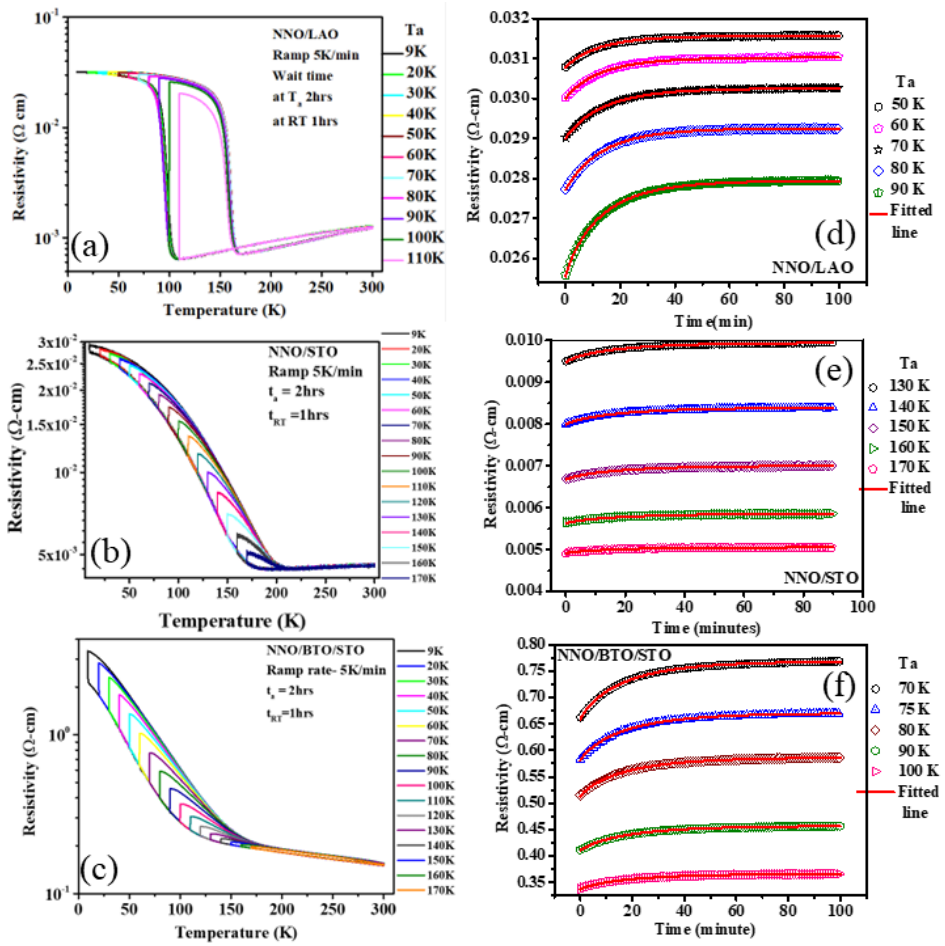

Figure 4.6. Hysteresis with isothermal annealing at several T_a for (a)NNO/LAO (b) NNO/STO (c) NNO/BTO/STO.The resistivity ralaxation curves under isothermal annealing for few representative T_a for (d)NNO/LAO (e)NNO/STO (f) NNO/BTO/STO. The lines through the data are fits to the streched exponential relation.

We have investigated the phenomena of attainment of maximum saturated resistivity over sufficient time of anneal (t_a) at $T_a(\leq T_{MI})$ in cooling run. During this process of isothermal annealing the resistivity relaxes to a higher value as the high temperature metallic phase transfroms to the insulating phase. The variation of resistivity with time shows that the systems slowly evolve towards an insulating state at $T = T_a$. The time dependent resistivity relaxation was fitted to a stretched exponential function (Eqn. 4) as given below and obtained the characteristic relaxation time, τ:

$$\rho = \rho_\infty - \rho_1 \exp[-(\frac{t}{\tau})^\beta] \tag{4}$$

$\rho_1(t) = \rho_\infty - \rho_0$ the relaxing part of the resistance, the exponent β and relaxation time τ are the fit parameters. From the τ, we obatined the mean relaxation time of relaxation $< \tau >$ given as $< \tau >= \frac{\tau}{\beta}\Gamma(\frac{1}{\beta})$. $\Gamma(\frac{1}{\beta})$ being the Gamma function.

Generally, β deviates from 1, it is taken as a signature of non-Debye relaxation .The hierarchical relaxation or stretched exponential relaxation might result from the distribution of the relaxing entities' relaxation times.The fitted parameters: β, τ, and the ratio $\delta\rho_{relax}=\frac{\rho_1}{\rho_\infty}$ have been found out for each T_a where the isothermal annealing performed for all the three films separately. The β lies between 1 and 0.75 for all the films . The three films show quantitatively different β both in their values and dependence on T_a. However, β in all the films have qualitative similarities. It starts from relatively low value for T_a which rises steadily as T_a is lowered and after reaching a shallow peak it decreases at still lower T_a. The data are given as Fig. 4.15 in 'Additional data and information' section. The detail discussion on the variation of τ with T_a and its link with the kinetics will be analysed at discussion section.

4.6 The variation of relaxational time (τ) as a scaled function of T_a

The evolution of the average relaxation rate, $< \tau >$ as a function of T_a have been obtained from the relaxation data. The data is added in Fig. 4.16 for all the samples in 'Additional data and information' section. It decreases on cooling below T_{MI} which is most expected for case of supercooled metallic phase conversation into stable insulating phases. However, it nature of decrement with T depends on sample to sample. The scale of $< \tau >$ is in the range of tens to few tens of minutes in all the films.

To compare the temperature dependences of relaxation times as observed in the three films, we present in Fig. 4.7 (b) a scaled graph of $\frac{<\tau>}{<\tau_{max}>}$ vs $\frac{T_a}{T_{MI}}$. τ_{max} is the maximum value of the relaxation time for a given film as it happens when $T_a \to T_{MI}$. The annealing temperature T_a is scaled by the T_{MI} of the given film for a cooling rate of 5K/min, which is compatible with the annealing experiment. It can be seen from Fig.4.7(b) that there are three distinct regions in the temperature dependence of the relaxation process. For $\frac{T_a}{T_{MI}} \geq 0.8$, the relaxation rate has a shallow temperature dependence for NNO/LAO and NNO/BTO/STO while it decreases for NNO/STO. For $0.8 > \frac{T_a}{T_{MI}} > 0.4$, for all the films the relaxation time decreases monotonously. At $\frac{T_a}{T_{MI}} \approx 0.4$ there is a break and at lower temperature it decreases further albeit with different slopes. For the film NNO/STO there is a local small maxima around $\frac{T_a}{T_{MI}} \approx 0.4$, pointing to a slowing down of the relaxation process over a small temperature region. Fig. 4.7 also shows that at temperature even below $0.4T_{MI}$ there is a finite relaxation time associated with the relaxation of the high temperature

metallic phase. This points to some degree of persistence of the high temperature phase well below T_{MI}.

At this point a broad qualitative correlation with the temperature dependence of the lattice constant can be made to rationalize the observed variations of $\frac{<\tau>}{<\tau_{max}>}$ with temperature. One of the factors that would determine the ease of transformation and hence the relaxation time is the stability of the metallic phase for $T < T_{MI}$. In NNO/STO, the large built-in tensile strain makes the metallic phase less stable. This makes the relaxation time smaller and just below T_{MI} it starts to drop. Below T_{MI}, the out-of-plane **c** enhances on cooling leading to decrease of the in-plane lattice constant thus decreasing the tensile strain to a degree and this leads to some enhancement of the stability of the metallic phase.It can be seen from Fig.4.2 (f) that the enhancement of **c** is rapid in the temperature range $T_{MI} \geq 0.4$. The modest local enhancement of the relaxation time may thus be related to this effect. For the other films, the built-in strain being compressive, the metallic phase will have higher stability leading to larger $< \tau >$ and near temperature independence of the relaxation time for $\frac{T_a}{T_{MI}} \geq 0.8$ can be linked to this stability. For all the samples the steady decrease in $< \tau >$ for $\frac{T_a}{T_{MI}} < 0.8$ can be linked to softening of the relaxation barrier discussed below.

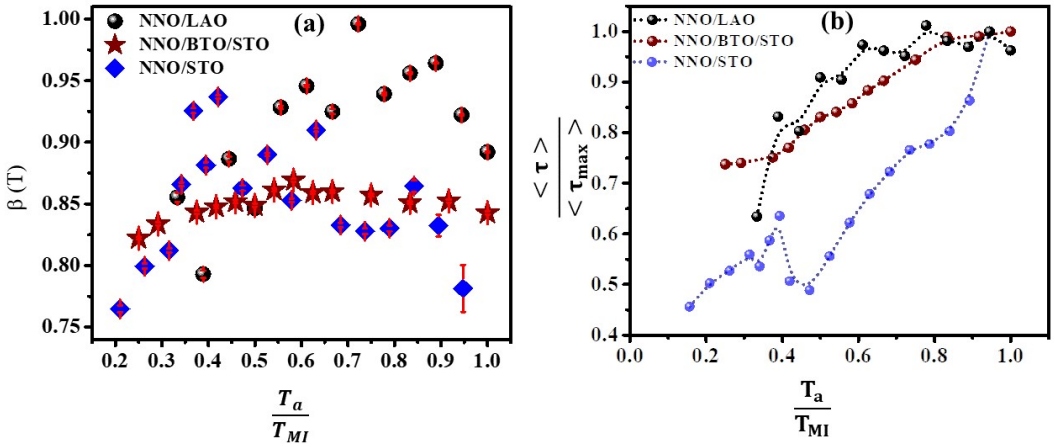

Figure 4.7. (a) The variation of β with scaled $\frac{T_a}{T_{MI}}$ for the three samples NNO/LAO, NNO/BTO/STO, and NNO/STO (b)The variation of scaled $\frac{<\tau>}{<\tau>_{max}}$ with scaled $\frac{T_a}{T_{MI}}$ for the three samples NNO/LAO, NNO/BTO/STO, and NNO/STO

4.7 A physical model for the phase transformation phenomenon and its utilization in Monte Carlo simulation.

A phase transformation would involve relaxation through a barrier (U) and in most common cases would involve a Arrhenius type relation:

$$< \tau(T) >= \tau_0 \exp(\frac{U}{k_B T}), \tag{5}$$

Where $<\tau(T)>$ is relaxation time which is temperature dependent. The k_B is the Boltzman constant. A temperature dependent U, that decreases on cooling, is needed to make $<\tau(T)>$ decrease with temperature. Given the fact that we may have a distribution of activation energy we use a modified Arrhenius form (with $\alpha < 1$) as shown below:

$$<\tau(T)>=\tau_0 \exp(\frac{U(T)}{k_B T}) = \tau_0 \exp(\frac{\eta v(T-T*)^{\alpha}}{T}); \eta = \frac{1}{v^*}(\frac{E^*}{k_B})^{1-\alpha} \tag{6}$$

The transformation of the metallic phase to the stable insulating phase occurs through transformation regions (TR) that have crystallites of volume v, which is size of the average of the relaxing volume, v^* is the scale of transformation volume $\approx$ unit cell size.E^* is scale for the transformation energy. The factor η also makes the expression for $<\tau(T)>$ with modified Arrhenius form dimensionally correct. From the simulation α as well as η can be extracted and we can obtain the energy E^* using the relation:

$$E^* = k_B (v^* \eta)^{1/1-\alpha} \tag{7}$$

The detail derivations of eqns. are written in 'Additional data and information' section.The temperature T^* needs mention. This is needed to prevent the barrier $U \to 0$ as $T \to 0$. Thus the above expression is valid for $T \geq T^*$ The expression for The monotonous decrease in $<\tau>$ with decreasing temperature occurs till $\frac{T}{T_{MI}} \approx 0.4$ where there are anomalous features.T^* is thus expected to be such that it is close to $\frac{T^*}{T_{MI}} \approx 0.4$. Later on we would seek more physical basis for T^*.

We have used the above model in the Monte Carlo Simulation, to obatin the relevant parameters from the relaxtaion data below T_{MI}. We have estimated the number total transforming regions (TR) which contains the metastable metallic phases and then calculated the density of the transforming region (TR density, n). (The TRs basically consist of large number of crystallites with each volume v.)

The probability p for transformation is $\propto <\tau>^{-1}$. For the rate heating and cooling experiment, it is given by the following relation:

$$p = exp(-\frac{\eta v(T-T*)^{\alpha}}{T}) \times \gamma \tag{8}$$

where the constant γ is a constant that normalizes the probability and also encompasses prefactor τ_0^{-1}
For the isothermal annealing since the temperature is held constant at T_a, the probability p also becomes time dependent that would tag-on with with the relaxation process. We use the following relation for the time dependent *p(t)* where a stretched exponential has been added as the time dependent part:

$$p(T=T_a) = exp(-\frac{\eta v(T_a-T*)^{\alpha}}{T_a}) \times \gamma \times \exp(-(\frac{t-t_0}{\tau})^{\beta} \tag{9}$$

t_0 is the start time of the anneal process at $T = T_a$.

The simulation that follows the transformation and change in the volume of the metastable metallic state gives us the change in the insulating volume fraction. If n = density of transforming regions (TRs) and Δn =change in number density of the TRs. The simulaion obtains the change in the insulating volume fraction (Δn) which is the change in the density of TR region. The fractional change is given as:

$$\zeta_v = \frac{\Delta n}{n} \tag{10}$$

ζ_v is a function of t as well as T. This information was then used to calculate the resistivity $\rho_{cal}(T)$ for rate heating and cooling experiment and $\rho_{cal}(T = T_a, t)$ for isothermal annealing experiment using General Effective Medium(GEM) theory [11].

$$\zeta_v = 1 - \frac{\rho_M(\rho_{cal} - \rho_I)}{\rho_{cal}(\rho_M - \rho_I)} \tag{11}$$

Where, ρ_{cal}, ρ_M, ρ_I are the calculated resistivity and full-scale extrapolated resistivity for metallic and insulating portion respectively. The metallic portion of the resistivity data has been fitted by the equation $\rho = \rho_0 + \rho_1 T^p$ (p = 1 for NNO/LAO and NNO/STO, but NNO/BTO/STO, p $\approx$ 0.16) and extrapolated for the full T range to find out the ρ_M. For the insulating phase we used the variable range hopping equation-

$$\rho T^{-1/4} = \rho_0 \exp[T_0^{1/4} T^{-1/4}] \tag{12}$$

Conversely, one can also obtain from the eqn. 11 above the ζ_v, using the observed resistivity data ρ_{obs}, in place of ρ_{cal}.

The high T metallic region above T_{MI} of the individual hysteresis curve for each set of ramp rate has been fitted with the mentioned Eqn. above to find out the fitted parameters ρ_0 and ρ_1 and p which are utilized to extrapolate for total T region to get ρ_M.The job is repeated for heating and cooling curve separately for all ramp's data of the films. In Fig 4.8 (a,b,c) the metallic resistivity fitting has been shown for only ramp of 5K/min at heating cycle for the individual samples. The low T region $\leq T_{MI}$ of the hysteresis curve is fitted with VRH Eqn. (12) both for heating and cooling curve. The ρ_I has been extracted using the fitted parameters obtained from VRH Eqn..In Fig. 4.8 (d, e,f), represents the VRH of ramp 5k/min for the samples. The ρ_I, ρ_M are used in GEM (Eqn. 11) to find out the insulating volume fraction (ζ_v). The hysteresis in ζ_v for ramp 5K/min along with the simulated ζ_v line below T_{MI} has been depicted in Fig. 4.8 (g, h, i).

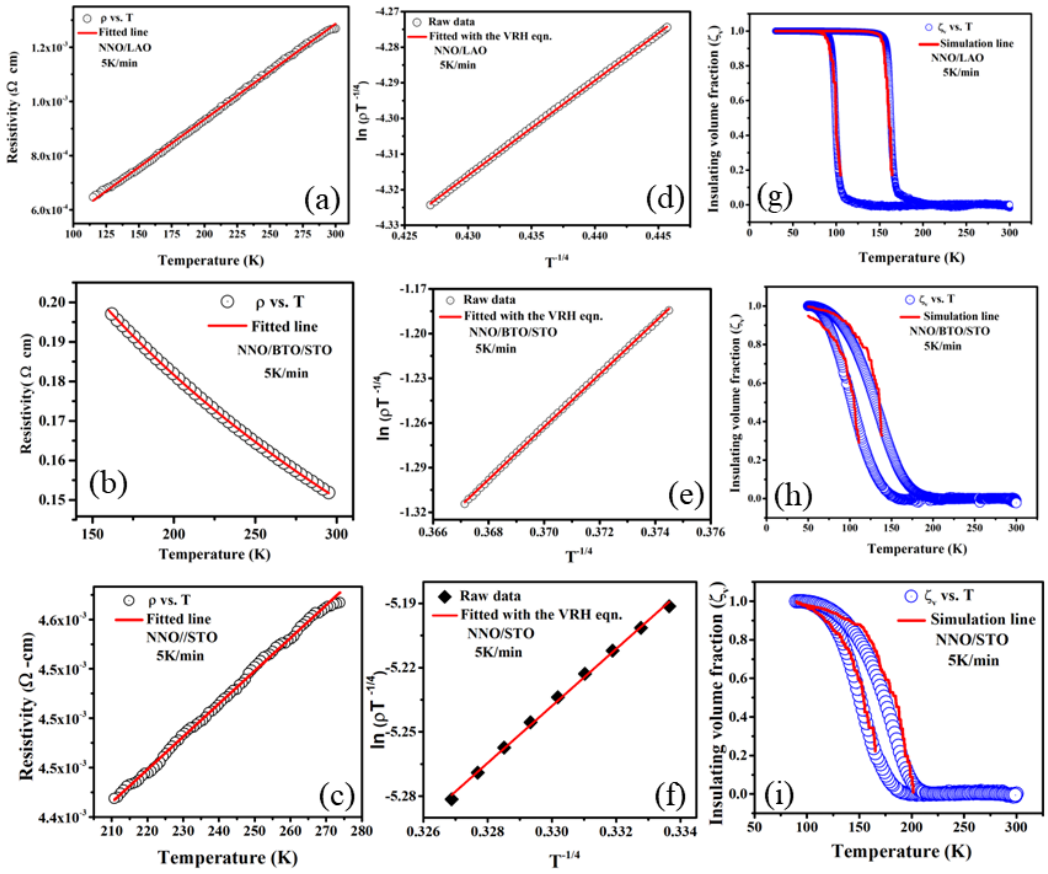

Figure 4.8. The fit of data to the resistivity Eqns for metallic part (a, b, c) and insulating part (d, e, f) with VRH (Eqn.-12) for ramp rate 5k/min for all the samples. Fig (g, h, i) shows the insulating volume fraction (ζ_v) calculated from GEM (Eqn. 11) and simulation(Eqn.10) for all the samples

The resistivity data have been reconstructed from the insulating volume fraction obtained from simulation using Eqn. 11 and compared with experiment.The simulation has been iterated till best matches between experimental insulating volume fraction obtained from the observed resistivity data ρ_{obs} and the simulation value. The details of the parameters which are used in the simulation are given in Table -III.

Table 3. Simulation details

Sample	T_{MI}	T^*	$\frac{T^*}{T_{MI}}$	n	η (T^*)	α	v$\times 10^{-7}$ (μm^3)	ζ_v at T_{MI}
NNO/LAO	105	30	0.29	4×10^{12}	6×10^{8}	0.33	1-5	0.109
NNO/BTO/STO	124	50	0.40	3×10^{11}	1.2×10^{9}	0.29	1-5	0.196
NNO/STO	191	90	0.47	5×10^{10}	2×10^{9}	0.25	1-5	0.012

T_{MI}, T^* - experimental value at ramp rate 5K/min, n = TR density. v = volume of TR. η, α fit parameters.

Simulation had been carried out for each set of ramp dependent hysteresis, starting from 0.5 K/min to 15 K/min for all the samples. In Fig. 4.9, we have shown the experimental resistivity (as a function of $\frac{1}{T}$) along with calculated resistivity data as obtained from simulation for few representative ramp rates. Good matching has been obtained with the data for all the ramp rates in the three films.

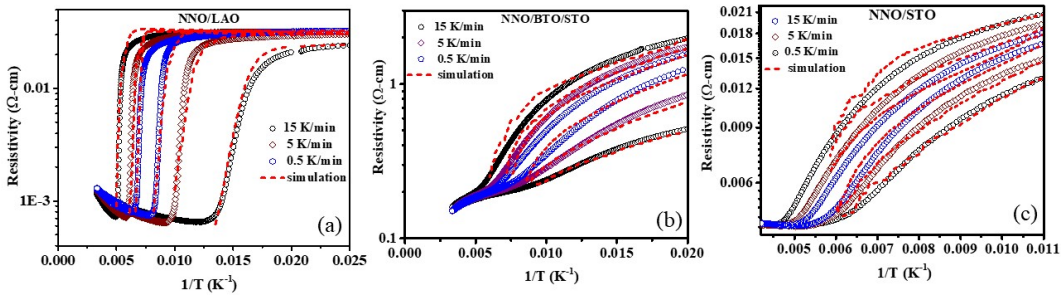

Figure 4.9. The ramp dependent hysteresis data for few representative ramp rates along with the simulated line of (a) NNO/LAO (b) NNO/BTO/STO (c) NNO/STO Note the temperature scale in $\frac{1}{T}$

We have followed the following procedure to compare the isothermal annealing data with the results obtained from simulation. The variation of the incremental insulating volume fraction ($\Delta\zeta_v$) with time at a given $T = T_a$ is obtained by subtracting the ζ_v by the value of ζ_v at t=0. So that $\Delta\zeta_v(t,T_a) = \zeta_v(t,T_a)$ - $\zeta_v(t=0,T_a)$. The variation of both experimental and simulation $\Delta\zeta_v$ lines have been shown with time in Fig. 4.10 for the samples at several representative T_a. We have taken such band of T_a which lies in the supercooling region below T_{MI}. The values of the parameters used are the same as that obtained previously from fit with the hystersis data. The match with experimntal data is good. Fig. 4.7 and 4.8 establish the efficacy of the simulation process. The model used and the simulation give a set of physical parameters that can be used to quantify the experimental data.

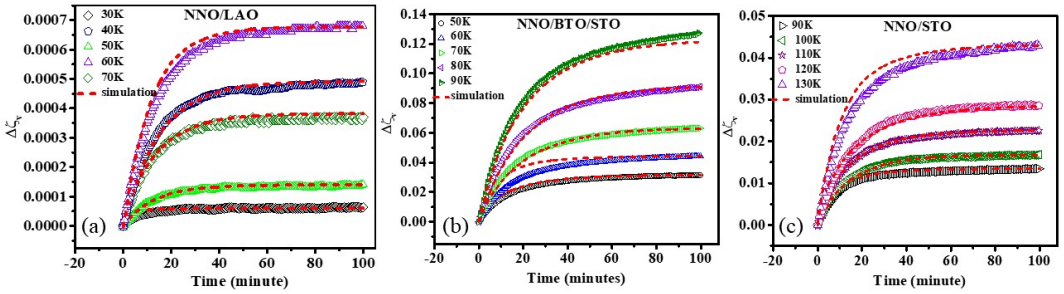

Figure 4.10. The variation of incremental relative insulating volume ($\Delta\zeta_v$) experimental data with simulated line at several representative Ta for (a) NNO/LAO (b) NNO/BTO/STO (c) NNO/STO

4.8 Discussion

4.8.1 The correlation between structural and simulation parameters

In this sub-section we would like to establish the correlations of the physical parameters as obtained from the simulation.A major quantity obtained from experiment is the average relaxation time $<\tau(T)>$. $<\tau(T)>$ decreases monotonously in all the films, when T is reduced till $\frac{T^*}{T_{MI}} \approx 0.4 \pm 0.1$. Temperature T^* has been introduced above to describe the temperature dependence of the barrier to relaxation. We would like to propose a plausible explanation for the temperature T^* as the limit of supercooling. The existence of metastable metallic phase for $T < T_{MI}$ and importantly continuous lowering of the transformation barrier on cooling is generally observed in supercooled systems. At the limit of supercooling (metastability) the barrier $\rightarrow 0$ and the relaxation time $\tau \rightarrow 0$ as well. Noting the similarity of our observation with that expected for a supercooled system, we propose to associate T^* as the limit of supercooling. The process of supercooling is inhibited by presence of heterosurface like a grain boundary. Thus a lower temperature of limit of supercooling is expected in a film that has less heterosurfaces like grain boundary. The coherent grain size being largest in NNO/LAO it can be supercooled to a somewhat lower temperature ($\frac{T^*}{T_{MI}} \approx 0.29$). As the coherent grain size decreases the value of $\frac{T^*}{T_{MI}}$ increases. This inverse correlation is shown in frame (a) of Fig.4.11.

An important parameter obtained from the simulation is the density of TR (n) and its temperature dependence. When the sample is cooled or heated at a given rate there is a clear change in n which in essence controls the relaxation characteristics and the associated hysteresis. A scaled plot of $\frac{n(T)}{n_{max}}$ vs $\frac{T}{T_{MI}}$ is shown in Fig. 4.11 (b). n_{max} is the value of n at $T = T_{MI}$.

The ratio $\frac{n(T)}{n_{max}}$ decreases monotonously as T is decreased with an approximate exponential dependence on T. The decrease is very similar for the films NNO/STO and NNO/BTO/STO while the temperature dependence is sharper for the film NNO/LAO that has bigger grains as well as less dislocation density. This rapid decrease of the ratio $\frac{n(T)}{n_{max}}$ with T is correlated with the sharp transition seen in the film NNO/LAO.

It is also observed that the dependence of $\frac{n(T)}{n_{max}}$ shows a sharp decrease in the temperature range $\frac{T}{T_{MI}} \leq 0.3 - 0.4$. In this range as can be seen from Fig. 4.11, the relaxation time also changes its temperature dependence. In this temperature range $T \rightarrow T^*$, which has been proposed as the limit of stability of the high temperature metallic phase. The rapid decrease of $\frac{n(T)}{n_{max}}$ on further cooling below T^* underscores this phenomena.

The parameter η is also obtained from the simulation. The η is function of both rate of cooling and heating as well as of temperature. Variation η with ramp rate (rate of cooling/heating) are plotted in Fig.4.11 along with variation of η for different T_a for a fixed ramp rate (5K/min.) η has a reciprocal dependence on ramp rate ($\frac{dT}{dt}$). From the reciprocal dependence it appears that $\eta \times \frac{dT}{dt} \approx$ constant. From Fig. 4.11 it can also be seen that η varies almost linearly with T for a given ramp rate.

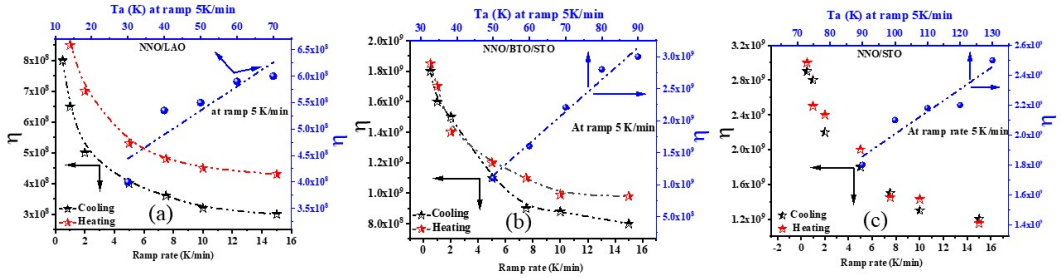

Figure 4.11. The variation of simulation parameter η with ramp rate and isothermal annealing temperature (T_a)

In Fig. 4. 12(a) we have plotted the dependence of two more simulation parameters α and η as a function of $< d >$. In this Figure we had also plotted the inverse correlation of T^* with $< d >$. The exponent α that measures degree of non-Debye relaxation has a clear dependence on $< d >$. For the film NNO/STO that has smallest grain boundary has lowest α and as the grain size grows α also increases. The modified Arrehenius form of the activated relaxation generally arises when there is a distribution of activation energy and the relaxation occurs over a distributed length scale as in Mott's variable range hopping (Eqn. 12) where the exponent is 0.25. In case of α, as has been observed in the simulation, it is close to this value for the the two films NNO/STO and NNO/BTO/STO that have rather smaller grain size with higher degree of quenched disorder. The enhanced grain size and reduced quenched disorder expectedlyenhances α.

The parameter η as defined is determined by E^*, which is the scale of energy of transformation and v^*. For different films v^* being same the primary differences would arise from E^*. The energy scale depends on a number of factors like free energy difference of the two co-existing phases and importantly internal surfaces like that seen in grain boundary that may act to enhance the scale E^*. A more comprehensive explanation would theoretical treatment is outside the scope of this investigation.

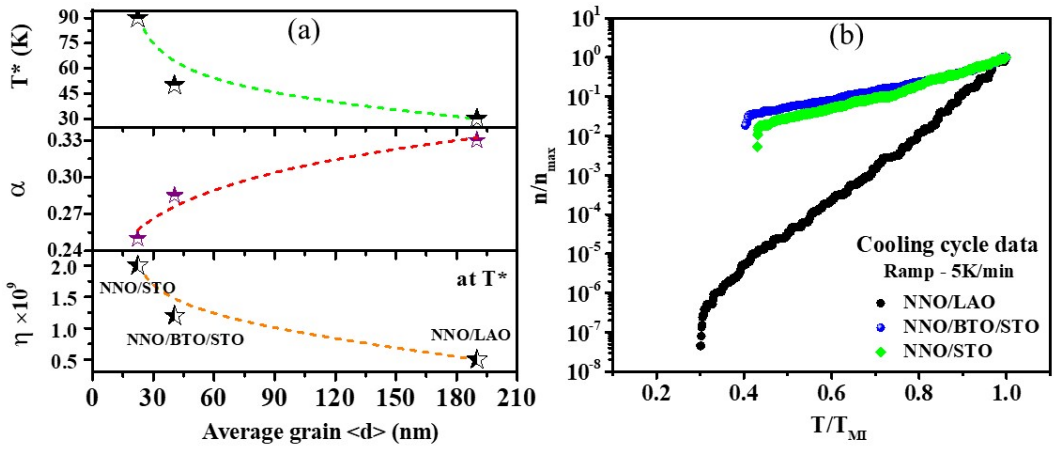

Figure 4.12. (a)Variation of simulation parameters T^*,α and η (at T=T^*) with average grain size $< d >$. The line through the data is guide to the eye. (b) Scaled variation of TR density(n) with uniform scaled cooling at 5K/min for the samples

In the context of magnetic transition there are extensive investigations of slow dynamics resulting from relaxation in supercooled high temperature metastable phase using temperature and magnetic field as tuning parameter. A glass like kinetically frozen phase in the metastable region had been observed. The slow relaxation arising below the T_{MI}, which has been investigated here, however, have a qualitative difference, that there is no kinetically arrested phase as the average relaxation time becomes shorter on cooling.

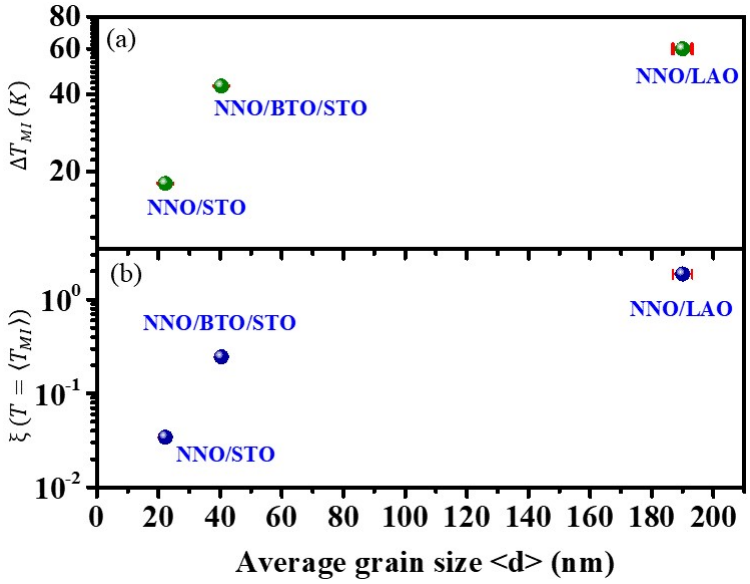

Figure 4.13. The variation of (a) ΔT_{MI} and (b) Scaled height of hysteresis $\xi(T =< T_{MI} >$ with average grain size for three samples at ramp 5 K/min.

We also find that the parameters obtained from experimental data, namely ΔT_{MI} and ξ also have a correlation with average grain size $< d >$ (Fig.4.13). There are certain models of hystersis that may explain this dependence but we have not explored them in the thesis.

4.9 Conclusion

In this chapter, we investigated thoroughly the slow kinetics of relaxation below the metal insulator (MI) transition temperature T_{MI} and its temperature dependence in NNO thin films grown on three distinct substrates. The MI transition in such films have co-existing phases and for $T < T_{MI}$ the metastable high temperature metallic phase that has its persistence in the stable low temperature insulating matrix transforms into stable insulating phase over cooling. The kinetics have been investigated by two sets of experiments. First, a ramp rate dependent hysteresis in the resistivity that arise during thermal cycling above and below the T_{MI} and the other with isothermal annealing below T_{MI} at a fixed temperature T_a. One important observation from the isothermal annealing experiment is that the average relaxation time $< \tau >$ decreases on cooling, contrary to the expectation of relaxation through a fixed barrier. This led us to propose a temperature dependent barrier to relaxation that leads to a relaxation time decreasing on cooling. This led to introduction of a temperature T^* in the temperature dependence of the barrier, which has been interpreted as a likely 'limit of supercooling' or the 'limit of metastability'.

A Monte Carlo simulation was used to analyse the experimental data which is based on a limited set of parameters that includes the temperature T^* where relaxation time, $< \tau >$ $\rightarrow 0$ and the energy scale of the transformation E^*. The parameters used in the simulation and also the experimental quantities like average relaxation time $< \tau >$ and its temperature dependence was found to be correlated with certain structural parameters, in particular, the crystallite grain size that determine the size range in these films.

4.10 Additional data and information

A. Grain size distribution and histogram plot

The mean grain size has been calculated by the histogram plot (Fig 4.14) from the AFM data for each film. The variation of grain size of each film has been fitted by the Gauss distribution function and calculated the mean grain size.

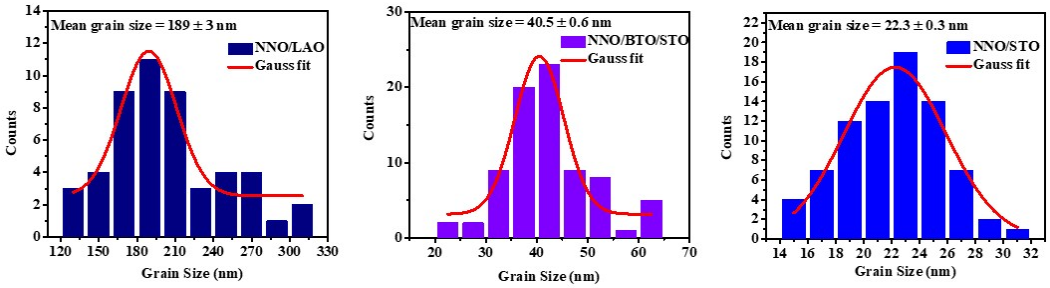

Figure 4.14. The average grain size ($< d >$) obtained from the count versus grain size showing the histogram for the samples

B. Temperature evolution of $\beta(T)$ and $\frac{\rho_1}{\rho_\infty}$ obtained from stretched exponential

From the time evolution of resistivity, we have obtained the fitted parameters using the stretched exponential mentioned in Eqn. (4). Here the $\beta(T)$ varies from 0.75 to 1 for all the cases in the T zone below T_{MI} imples the stretched nature of relaxational phases. where as the degree of attainment of maximum resistivity i.e., insulating phase content evolution justified by the ratio $\frac{\rho_1}{\rho_\infty}$ in the said T range. The data is given in Fig. 4.15

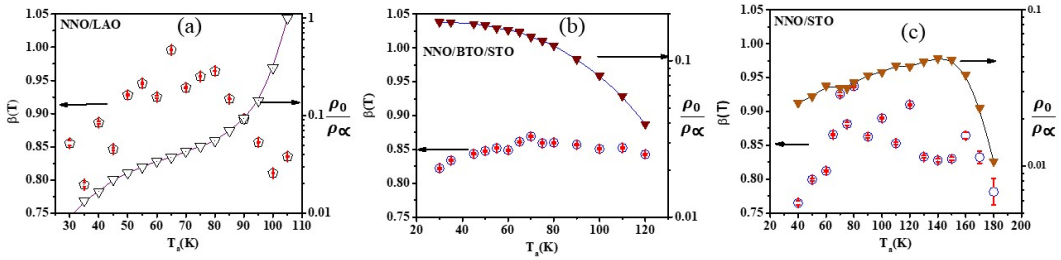

Figure 4.15. The temperature evolution of exponent $\beta(T)$ and $\frac{\rho_1}{\rho_\infty}$ obtained from the fitting with Eqn, 4 for (a) NNO/LAO (b) NNO/BTO/STO (c) NNO/STO

C. Average relaxation time $< \tau >$ as a function of T_a

The average relaxation time, $< \tau >$ has been displayed as a function of annealing temperature (T_a) in Fig. 4.16 which is calculated using Gamma function aforementioned in the text.

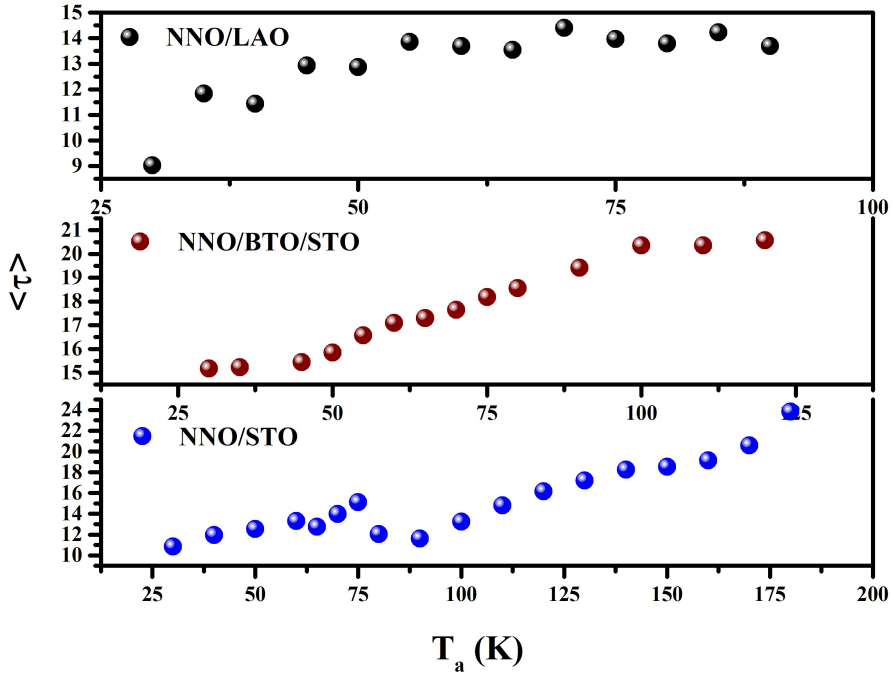

Figure 4.16. Average relaxation rate time $< \tau >$ as a function of T_a

D.Temperature variation of potential barrier (U)

In the M.C simulation, the barrier energy (U) is a continuous and monotonic function of (T - T*) which is defined by Eqn. (6). This variation stands the phase conversation protocol from meta-stable metallic to stable insulating phase. For better understanding, we have started showing the evolution of U from common high temperature 190K which ends in respective T* of the samples. It has the direct structural parameter (average grain size, $< d >$) link NNO/STO has largest U with smallest average grain size where as for NNO/LAO only U $\approx$ 18 meV is recorded having largest $< d >$.

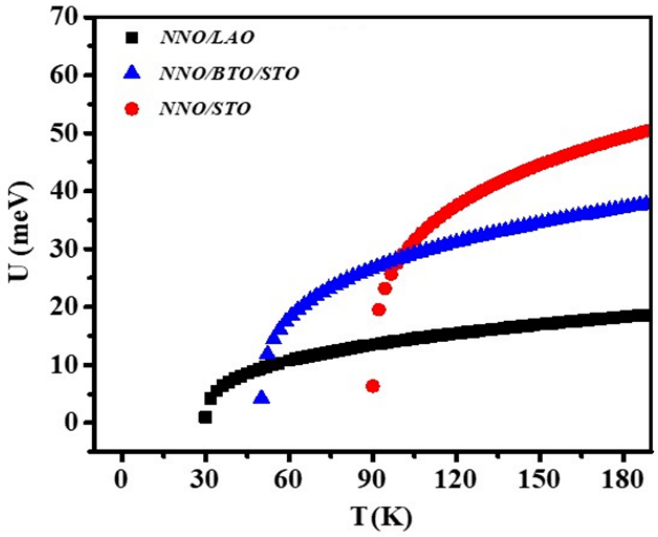

Figure 4.17. The variation of potential barrier with temperature for NNO/LAO, NNO/BTO/STO and NNO/STO

References

[1] M. M. Qazilbash, A.Tripathi, A. A Schafgans, Bong-Jun Kim, Hyun-Tak Kim,Zhonghou Cai, M. V. Holt,J. M. Maser, F. Keilmann,O. G. Shpyrko, and D. N. Basov, Phys. Rev. B, 83, 165108 (2011)

[2] A. S. McLeod, E. van Heumen, J.G. Ramirez, S. Wang, T. Saerbeck, S. Guenon, M. Goldflam, L. Anderegg P. Kelly, A. Mueller, M. K. Liu, Ivan K. Schuller1 and D. N. Basov,Nature Phys 13, 80–86 (2017).

[3] M. M. Qazilbash, A. A. Schafgans, K. S. Burch, S. J. Yun, B. G. Chae, B. J. Kim, H. T. Kim, and D. N. Basov, Phys. Rev. B, 77, 115121 (2008)

[4] K. W Post, A. S. McLeod, M. Hepting, M. Bluschke, Yifan Wang, G. Cristiani, G. Logvenov, A. Charnukha, G. X. Ni, P. Radhakrishnan, M. Minola, A. Pasupathy, A. V. Boris, E. Benckiser, K. A. Dahmen, E. W. Carlson, B. Keimer and D. N. Basov, Nature Phys 14, 1056–1061 (2018).

[5] R. S. Bisht, S. Samanta, and A. K. Raychaudhuri, Phys. Rev. B 95, 115147 (2017).

[6] S. Chatterjee, R. S. Bisht, V. R. Reddy and A. K. Raychaudhuri, Phy. Rev. B, 104, 155101 (2021).

[7] R. Yamamoto , T. Furukawa , K. Miyagawa ,T. Sasaki, K. Kanoda and T. Itou, Phys. Rev. Letts 124, 046404 (2020).

[8] P. Majhi, S. Chatterjee, R. S. Bisht, V. R. Reddy, B. Ghosh, and A. K. Raychaudhuri, Phys Review Matt. 5, 085005 (2021).

[9] X. Granados, J. Fontcuberta, and X. Obradors, Phys. Rev. B 46, 15683 (1992).

[10] D. Kumar K P Rajeev, J A Alonso and M JMartınez-Lope, Phys. Condens. Matter 21 185402 (2009.)

[11] D. S. McLachlan, J. Phys C: Solid State Phys. 20, 865 (1987).

[12] J. L. G. Muñoz, M. A. G. Aranda, J. A. Alonso and M. J. Martínez-Lope,Phys. Rev. B 79, 134432 (2009)

Chapter 5

Effect of voltage controlled reversible strain on M-I transition and other physical properties in $NdNiO_3$ film

Abstract: *In this chapter we investigate the effect of small but reversible strain that can be created on a film of $NdNiO_3(NNO)$ (grown on a piezo-electric substrate like $BaTiO_3(BTO)$) by applying a bias electric field on the substrate. In general, strains in a film are produced by growing them on substrates with lattice constant mismatch but the strain so produced is irreversible and often due to finite film thickness the strain is relaxed. We have used a single crystal BTO and also a film of BTO grown on $SrTiO_3(STO)$ as substrates to grow NNO films. The strain produced in the film as well as the substrate by the applied field bias was calibrated by measuring in-situ the X-Ray diffraction and the shift in the characteristics diffraction lines.We have investigated change in the in plane resistivity ($\rho_{\parallel}$) as produced by the strain originating from the applied electric field on the underlying piezo-electric substrate. The For either field bias the in-plane field was found to be compressive, leading to reduction in $\rho_{\parallel}$, that enhances on cooling and was found to have a non-linear dependence on the applied strain. The strain effects in the two films (one on single crystal BTO and other on the film of BTO were complimentary. The investigation was carried out to well below the M-I transition temperature T_{MI} in the film grown on the film of BTO grown on STO as the single crystal BTO often cracks due to internal strain on cool down. The observations were analyzed using information on MI transition in NNO films as well as the temperature dependent Structure of BTO.*

5.1 Introduction

In the thesis (as described in Chapter 3 and 4) the strained/strained relaxed films were used where the film of $NdNiO_3(NNO)$ was grown on single crystalline substrates that have lattice constant. Strain in the film can be substantial, yet it is irreversible as it is in-built in the film during growth. This is the conventional way to investigate effect of strain and related interventions that modulate the physical property of the film. In this chapter we undertake investigation using a different and unconventional approach (although used by some investigators) to where the film of NNO is grown on a Ferro- and Piezo- electric substrate like $BaTiO_3$ and on application of an electric field ($E_\perp$) perpendicular to the substrate surface an out-of plane mechanical strain ($\epsilon_\perp^{sub}$) is created on the substrate. A fraction of the strain substrate so created gets transferred to the NNO film and creates an out-of-plane strain $\epsilon_\perp$ as well as a biaxial in-plane strain $\epsilon_\parallel$ in the film, linked to the former by the Poisson ratio (ν). This method produces a reversible but a small strain.

In materials like manganites where Jahn-Teller effects play a dominant role this type of bi-axial in-plane strain can create big effects which have been investigated [1–5]. In other ABO_3 type perovskite oxides like NNO [6, 7] or Rhuthanates [8], the band width can get changed by strain due to change in orbital overlaps arising from change in Metal-Oxygen-Metal angle. In general, in such oxides with ABO_3 structure, on application of a compressive bi-axial in plane strain $\epsilon_\parallel$, the bond B-O-B straightens and becomes closer to 180^0 . This enhances the band width, reduces the resistivity and stabilizes the metallic phase.

For investigation on physical effects applied reversible strains, two direct methods can be used that allow calibration are, (a) Film grown on a cantilever, which can be bent into flexure and can produce both compressive or tesnile strain of relatively large magnitude ($\approx 5\%$) depending on the substrate flexibility.(ref Jaynto sarka et.al, Amlan Biswas eta.al). (b) Use a Piezo-electric substrate as has been done here. A popular choice is the relaxor ferro-electric and piezoelectric substrate $0.67Pb(Mg_{1/3}Nb_{2/3})O_3 - 0.33PbTiO_3$ $(PMN-PT)$, that is available commercially as a crystalline substrate (Rata group JAP as reference) One problem , however, is that the substrate has large lattice constant mismatch with many oxides resulting in films with large defects. It is a practice to grow a buffer layer to reduce the lattice constant mismatch. But the strain transferred gets reduced. The straining depends on orientation. In orientation (001) for either sign of the applied bias, the out-of-plane strain is tensile, which also is the case for $BaTiO_3$. In orientation (111) the strain can change from tensile to compressive as the sign of the applied bias changes. Before using the crystal for experiment, it is necessary to poll them with a field that is $\geq E_C$, where E_C is the coercive field [2–4, 9].

In this thesis, we report strain-field- mediated control of electrical transport in oriented NNO films grown on $BaTiO_3$ (BTO) single crystal (SC) (referred to as Sample S1) and also on a NNO film grown on a pre-deposited $BaTiO_3$ layer grown on conducting $Nb-SrTiO_3$ $(BTO/Nb-STO)$. This sample is referred to as sample S2. Here Nb-STO (0.7% Nb

doped $SrTiO3$) substrate on which $BaTiO_3$ is grown is also used as the conducting bottom electrode.The BTO-SC and BTO/Nb:STO substrates are best alternative substrate of $PMN-PT$ which can generates sufficient bi- axial strain by converse piezoelectric coupling. Since the $BaTiO_3$ can be grown also as a film, it gives us an opportunity to create relatively appreciable strain for small bias. Lattice constant mismatch however remain similar as shown in Table I .The lattice constant mediated residual strain is tensile out-of-plane and compressive in-plane. It can be seen in Chapter 3 and 4 that the NNO films are largely strain relaxed due to thickness of the film. The degree of residual strain is more in the sample S1 compared to that in multilayer sample S2.

Table 1. Estimation of lattice mismatch between substrate and NNO film from (002) peak, XRD data

Sample	c_{NNO}(Å)	c_{ML}(Å)	$c_{substrate}$(Å)	Δc(%)
NNO/BTO-SC (001)	3.813	NA	4.03	-5.69
NNO/BTO/Nb: STO (001)	3.807	3.990	3.904	-4.8
NNO/PMN-PT-SC(001)	3.804	NA	4.004	-5.25
NNO/STO/PMN-PT (001)	3.795	3.9	4.004	-2.77

ML- middle layer(BTO or STO),Lattice mismatch $(\Delta c) = \frac{c_{film}-c_{substrate/ML}}{c_{film}} \times 100\%$

Use of both single crystal based sample S1 and the film based sample S2, provide complimentary situation. While sample S1, gives a proper well calibrated Ferro and Piezo-electric substrate with a measurable E_C, it has two bottlenecks for use. Firstly, a larger thickness ($\leq 500\mu$ m) limits the Field to be applied $E_\perp$ to a low value. For a given thickness of 500μm even a large bias of 0.5kV give rise to a a field $E_\perp = 1 \times 10^6$V/m. Secondly, $BaTiO_3$- SC on cooling develops large strain which lead to explosive cracking. In case of sample S2, $BaTiO_3$ layer (110nm) has much weaker Piezo-electric characteristics where the coercive field E_C is very low. However, this sample can be temperature cycled to 10K or below without cracking and allow for a much larger applied field ($E_\perp$) which is about 5000 times larger compared to that in the single crystal for the same applied bias.

In our experiment we calibrated the strain generated in the film from the shift in the lattice constant with applied bias which can be measured by the X-Ray diffraction (XRD) . From study on the NNO grown on the $BaTiO$ film (sample S2) down to 10K we observed that the applied in plane bi-axial compressive strain ($\epsilon_\parallel$) can lead to sufficient reduction in the in-plane resistivity ($\rho_\parallel$) of the NNO film and the reduction is severely enhanced at low T (below 100K). The temperature dependence of the strain dependence carries signature of the MI transition as well as the transitions of $BaTiO_3$ at low temperatures ($\leq$) 100K. The applied strain bi-axial strain stabilizes the metallic state and shifts the metal-insulator transition temperature (T_{MI}) to lower temperatures.

5.2 Field induced strain in a piezo-electric crystal and strain transfer in the film grown on it

The strain generated in a piezo-electric crystal creates charge which is generally expressed in the form:

$$P_i = \Sigma_{jk} \tilde{d}_{ijk} \sigma_{jk} \tag{1}$$

Here the summation is over the indices i,j,k that range for 1,2,3. $\tilde{d}_{ijk}$ is the 3rd order piezo-electric sensor, P_i is the polarization vector and σ_{jk} is the second order stress tensor.

The strain is created in a piezo-electric crystal using inverse piezo-electric effect, where an applied field creates a polarization (charge) which in turn creates a strain. Under *stress free condition*, the strain sensor (ϵ_{ij}) can be linked to the applied electric field vector (E_i) using the inverse piezo-electric 3rd order tensor d_{ijk} so that:

$$\epsilon_{ij} = \Sigma_k d_{ijk} E_k \tag{2}$$

In practice, the two-index engineering notation is often used which utilizes the symmetry properties of the tensors. In terms of the engineering notation, the two symmetric indices (i.e. i,j,k) ranging from 1 to 3 are replaced by a single index ranging from 1 to 6 and is given as $(11 \rightarrow 1)$, $(22 \rightarrow 2)$,$(33 \rightarrow 3)$,$(23 \rightarrow 4)$,$(31 \rightarrow 5)$,$(12 \rightarrow 6)$. In this notation the inverse piezo-electric Eqn. can be written as:

$$\begin{pmatrix} \epsilon_1 \\ \epsilon_2 \\ \epsilon_3 \\ \epsilon_4 \\ \epsilon_5 \\ \epsilon_6 \end{pmatrix} = \begin{pmatrix} 0 & 0 & d_{31} \\ 0 & 0 & d_{32} \\ 0 & 0 & d_{33} \\ 0 & d_{24} & 0 \\ d_{15} & 0 & 0 \\ 0 & 0 & 0 \end{pmatrix} \times \begin{pmatrix} E_1 \\ E_2 \\ E_3 \end{pmatrix}$$

If Z-axis (k=3) is chosen perpendicular to the substrate , the piezo-strain along z axis or perpendicular to the substrate ($\epsilon_{\perp}^{sub}$) can be evaluated from the Eqn above , which is proportional to the applied electric field ($E_{\perp}$) through the coefficient d_{33} so that:

$$\epsilon_{\perp}^{sub} = d_{33} \times E_{\perp} \tag{3}$$

Primary straining occurs in the substrate ($BaTiO_3$) on which the film is grown. The substrate has orientation (001). The strains in the substrate are termed as $\epsilon_{\perp}^{sub}$ which is the Z-axis perpendicular to the substrate and $\epsilon_{\parallel}^{sub}$ which is the bi-axial strain in-plane on the substrate. The bi-axial strain is generated by this process and these two strains are related through the Poisson Eqn.:

$$\epsilon_{\parallel}^{sub} = \frac{\epsilon_{\perp}^{sub}}{\nu} \tag{4}$$

where ν is the Poisson constant.
The bi-axial substrate strain creates a bi-axial strain $\epsilon_{\parallel}^{film}$ in the plane of the film and also a transverse strain $\epsilon_{\perp}^{film}$. In the XRD experiment with applied field bias on the substrate,

described in the next section, we determine the transverse strains both in the film and the substrate. The total transfer of the transverse strain can be quantified from the shift in the lattice constant through the ratio defined as:

$$\gamma = \frac{\epsilon_{\perp}^{film}}{\epsilon_{\perp}^{sub}} \tag{5}$$

5.3 Growth of NNO film

Detailed discussion on film growth and basic characterization have been discusse in earlier Chapters specifically in Chapter 2. Here we mention a brief description for the sake of completeness. For both cases we have deposited NNO of equal thickness $\approx 27nm$ by pulsed laser deposition. The films' top surface morphologies, surface roughnesses and compactness had been checked by AFM. The thickness of $BaTiO_3$ layer has been measured with the cross- sectional SEM [Fig. 5.1(b)] which is $\approx 110nm$ separately before preparing the bilayer NNO/BTO/Nb-STO. The bi-layer $NNO(27nm)/BTO(110nm)/Nb-STO$ was deposited in-situ without breaking the vacuum. The lattice mismatch between NNO and BTO is relatively large as shown in Table I. This leads to strain relaxation and sometimes quenched disorder observed in such systems which we have shown in previuos publication from the group. [10]. X-ray diffraction data for both bi-layered $NNO/BTO/Nb-STO$ and $NNO/BTO-SC$ film are shown in Fig. 5.1 (a).The NNO films grow as highly oriented film with growth along (001) crystallographic direction.

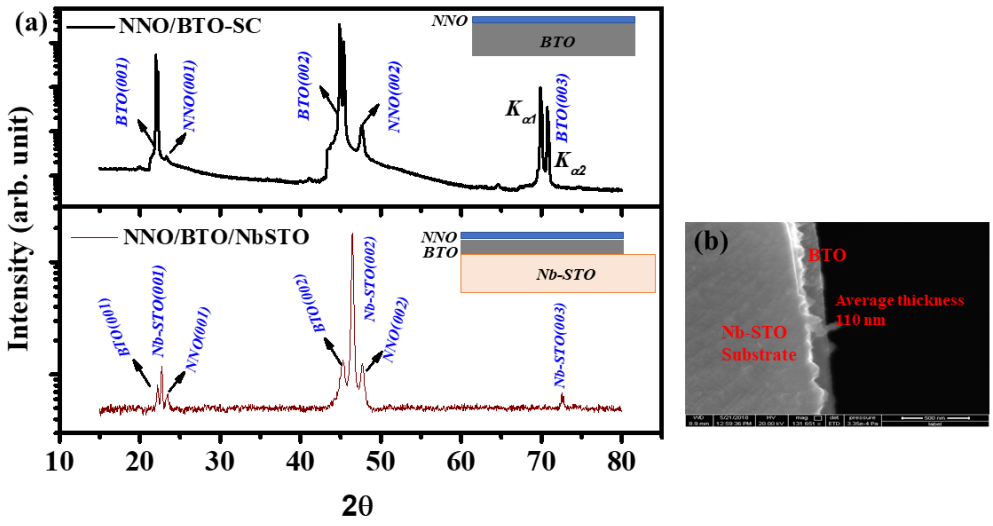

Figure 5.1. (a) The XRD data of NNO/BTO-SC and NNO/BTO/Nb: STO film along (002) crystallographic orientation. Inset: The schematic diagram of NNO based single and multi layer film. (b) The cross-sectional SEM image showing the average thickness of BTO layer grown on Nb: STO

5.4 XRD measurement with applied bias on the piezo-electric substrate

We have carried out bias dependent XRD measurement to measure the characteristics peak shift compared to the zero-bias data. In Fig. 2 (a, b), the schematic diagram of measurement set-up with wire connected films are shown. We have fixed the sample on the XRD stage with the help of GE-varnish and connected the voltage with top and bottom electrodes as shown in the schematic diagram. Before applying the bias, the zero-bias run has been taken place few times to check the reproducibility.

We have applied maximum bias of $\pm$ 0.5 kV for NNO/BTO-SC (corresponding to $E \approx 1 \times 10^6$ V/m) and a maximum bias of $\pm$ 1.5 V (corresponding to $E \approx 1.4 \times 10^7$ V/m).

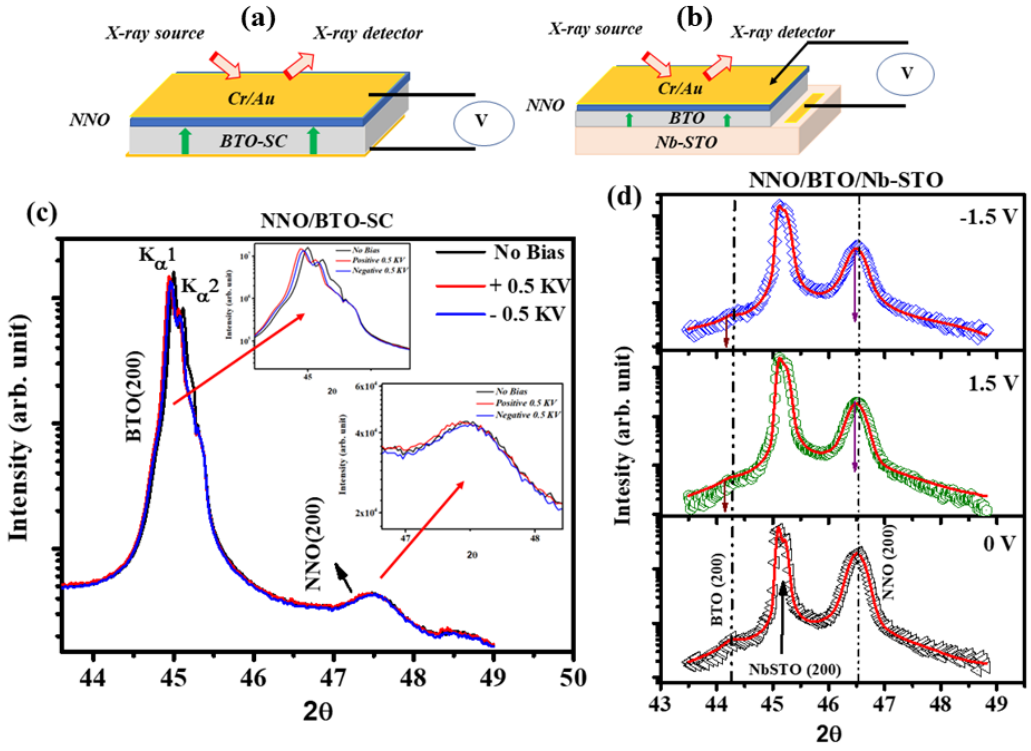

Figure 5.2. (a, b) The schematic diagram of voltage dependent XRD set up with the films and necessary circuit connection. (c) The peak (002) shifting with applied piezo-bias for NNO/BTO-SC. Inset: Zoom view of the peak left shifting. (d) The BTO (002) and NNO (002) peak shifting with bias for NNO/BTO/Nb: STO

In Fig. 2(c) and 2(d) XRD data for the two samples are shown. The data are shown for the (002) peaks for both substrates and NNO films. The exact peak shift was measured by fitting the lines to locate the peak position. For both the films the peaks shift to left (lowering of 2θ values) implying stretching of the out-of-plane lattice for both biases. This results in a out-of-plane $\epsilon_{\perp}^{film}$ which is tensile. This shows that the in-plane strain $\epsilon_{\parallel}^{film}$ is

compressive for both films. Exact values of strains are summarized in Table 2.Importantly, Nb-STO (002) peak shows negligible peakshift on application of bias, which is expected because the bias is applied on the top surface of Nb-STO.

These data establish that BTO-SC and BTO layer are getting strained with bias and they also transfer sufficient fraction to the top NNO layer. The value of strain transfer coefficient γ are also shown in Table 2. The table also shows the asymmetry in strain ($A_{\epsilon_\perp} = \frac{\epsilon_\perp^+}{\epsilon_\perp^-}$) as well as asymmetry in strain transfer coefficents ($A_\gamma = \frac{\gamma^+}{\gamma^-}$) .The asyemmetry is larger in the BTO-SC sample (S1) compared to that in the BTO-film sample (S2). We will see that it gets reflected in the change in the resistivity when bias is applied on the substrate. If we define an average strain $\epsilon = \frac{\epsilon^+ + \epsilon^-}{2}$ then the ratio $\delta = \frac{\epsilon_\perp}{E_\perp}$ can be obtained from the data . For sample S1, $\delta \approx 8.6 \times 10^{-8} \frac{\%}{V/m}$ and for sample S2 that has the BTO film $\delta \approx 4.5 \times 10^{-9} \frac{\%}{V/m}$. The lower value of δ in the film of BTO is related to weaker d_{33} in the film sample. The weaker d_{33} is due to weaker Piezo-electricity in the film. This issue will raised again in the next section.

Table 2. Calculation of piezo-strain and γ

NNO/BTO-SC (S1) (Bias=± 0.5kV)						
Layer/substrate	$\epsilon_\perp^+(\%)$	$\gamma^+(\%)$	$\epsilon_\perp^-(\%)$	$\gamma^-(\%)$	$A_{\epsilon_\perp}$	A_γ
BTO-SC	-0.106	...	-0.066	...	1.6	...
NNO	-0.048	45.28	-0.018	27.27	2.7	1.6
NNO/BTO/Nb:STO (S2) (Bias=± 1.5V)						
Layer/substrate	$\epsilon_\perp^+(\%)$	$\gamma^+(\%)$	$\epsilon_\perp^-(\%)$	$\gamma^-(\%)$	$A_{\epsilon_\perp}$	A_γ
BTO	-0.069	...	-0.056	...	1.23	...
NNO	-0.041	59.42	-0.028	50.02	1.46	1.19

In the table above the superscipts +(-) refer to positive (negative) bias.

5.5 Bias controlled in-plane resistivity

5.5.1 Single Crystal $BaTiO_3$ as substrate : Sample S1

The relative change in the in-plane resistivity (ρ) of the NNO film grown on the susbtrate by the bias induced piezo-strain arising from the BTO -SC is shown in Fig 5.3(a).The relative change in resistivity has been defined by the relation:

$$\frac{\Delta\rho_\parallel}{\rho}(E_\perp) = \frac{\rho_\parallel(E) - \rho_\parallel(0)}{\rho(0)} \tag{6}$$

The data has been taken at room temperature.The inset shows the electrode configuration, where the bias is applied perpendicular to the crystal face. The maximum bias used is ±150V corresponding to a Field if $E_\perp = 3 \times 10^5 V/m$. The data shows clear butterfly behavior and

strong asymmetry which follows the asymmetry of the strain as shown in Table 2. The relative change is negative for either bias and reflects the strain behavior of the substrate. The negative relative change is due to in-plane strain being compressive for either bias direction. The bias dependence of $\frac{\Delta\rho_{\|}}{\rho}$ is almost linear in the limited range of strain with a parabolic smoothing near the peak.

The obsereved resistivity change of the NNO film can be linked to the Piezo-electric behavior of the BTO single crystal. The Polarization-applied bias $(P-E)$ curve in the single crystal obtained with a Hysteresis loop tracer is shown in Fig. 5.3 (b). The $(P-E)$ curve is that of a conventional Piezo-electric crystal with a Coercive field $E_C \approx$ corresponding to an applied bias of 50V. The peak in the resistivity (Fig 5.3 (a)) occurs at applied bias which ic close to the measured E_C. This particular observation links the strain in the crystal by inverse Piezo-electric effect and in turn relates it with the change in resistivity in the NNO film. For a bias of +150V on the substrate the strain on the film $\epsilon_{\perp}^{film} \approx .0144\%$. Using a value of Poisson ratio ν =0.33 , we get in-plane biaxial strain of $\epsilon_{\|}^{film} \approx 0.044\%$. Often the change in resistance of films by a strain is characterized by a Gauge factor defined as $G = \frac{\Delta\rho_{\|}/\rho_{\|}}{\epsilon_{\|}^{film}}$. Strictly speaking the Gauge factor is defined as $G = \frac{\Delta R/R}{\epsilon_{\|}}$, since resistance (R) and resistance change ΔR are measured directly. Taking care of the directional changes in the film on strain one obtains:

$$\frac{\Delta R/R}{\epsilon_{\|}} = 1 + 2\nu + \frac{\Delta\rho_{\|}/\rho_{\|}}{\epsilon_{\|}} \tag{7}$$

In the Eqn. above the first two terms arise from change in dimension and the last term arises from change in the material under straining like band structure related effects.For metal strain gauges the factor is close to 2 because negligible effects of strain on resistivity ρ. For the NNO film on BTO-Sc $G \geq 100$ This is also comparable to larger than Gauge factors seen in Manganites films at their MI transition. Thus in our evaluation of the gauge factor we have neglected the term $1+2\nu$ that does bot contribute more than 2. As mentioned before, the proper Piezo-electric property of BTO-SC gave us a calibrated system for the estimation of effect of strain. However, due to its mechanical instability on cooling we did not take data using the BTO-SC to lower temperatures.

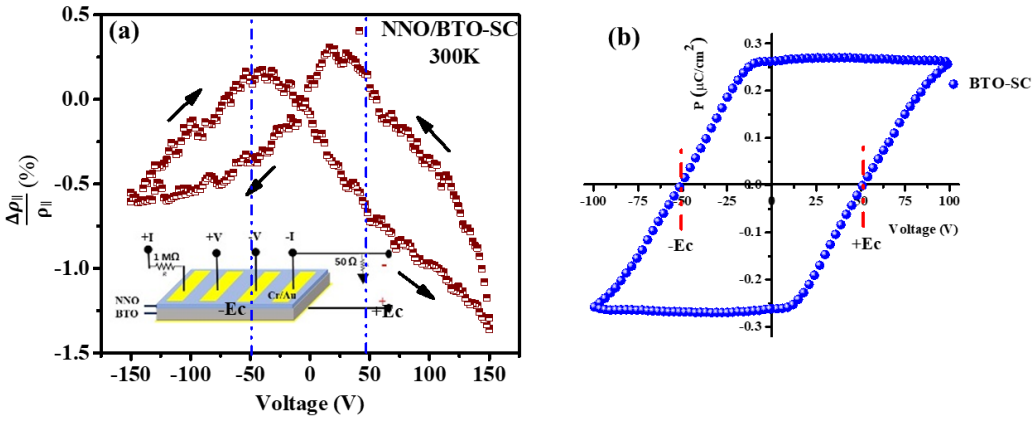

Figure 5.3. (a) The variation of ($\frac{\Delta\rho_{\parallel}}{\rho}$) with bi-polar bias voltage showing the butterfly like hysteresis for $NNO/BTO-SC$ (b) P-E loop data for $BTO-SC$ showing the coercive field ($\pm E_C$) value.

5.5.2 Film of $BaTiO_3$ as substrate : Sample S2

A film of BTO grown on a Nb:STO substrate has been investigated structurally as for its Piezo-electric property by previous investigators from our group [11]. It has been found that such a film shows Ferro-electric transition and all the variety of low temperature phase transitions as it happens in a single crystal. However, it has a finite d_{33} although it is smaller than that seen on a BTO-SC. The $P-E$ loop also shows suppressed Polarization and a Coercive Field $E_C \to 0$. The $P-E$ of the film is shown in Fig. 5.4 (b). This particular background gives us some basic information needed to understand the data on the bias strained NNO film grown on the BTO layer.

In NNO film on BTO film, the relative resistivity change with applied bias shows interesting and new features compared to that seen in $NNO/BTO-SC$ mentioned above and also in comprison to similar experiments reported before [6]. The relative change in resistivity for the NNO on BTO film for applied bias on the BTO film is shown in Fig. 5.4(a). The data have been taken from 300K down to 9K. The resistivity does decrease on enhancing the strain (that occurs for both signs of the bias) similar to that found in the film grown on $BTO-SC$. However, there are major qualitative differences in resistivity change in response to the applied bias. There is no butterfly type of behavior that have been seen in Fig. 5.3(a) with peaks occurring at finite bias filed close to E_C. As can be seen the change is centred around zero bias which is expected because in the BTO film $E_C \to 0$.

The effect of strain is enhanced significantly on cooling, and it increases by a factor of 4 when T is changed from 300K to 9K. The approximate gauge factor of the NNO film on the BTO at room temperature $G \approx 180$. This is larger than that seen in the sample S1 by a factor of ≈ 2. At 10K $G \approx 750$, which is quite large. This implies that the in-plane strain enhances the band width significantly and this has more relative effect on the insulating state. There are not too many available/published data of G factor on ABO_3 type oxides

undergoing MI transition. From the limited data set available we find that the NNO film shows one of the highest response to strain.

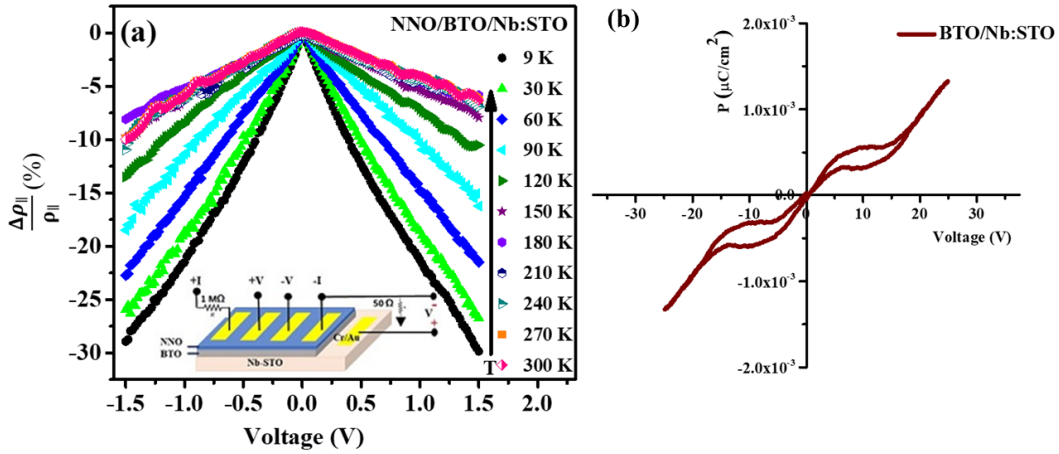

Figure 5.4. (a) The variation of ($\frac{\Delta\rho_\parallel}{\rho}$) with bi-polar bias voltage for NNO/BTO/Nb: STO (b) P-E loop data for BTO film grown Nb: STO showing the aged ferroelectric nature with coercive field ($\pm E_C$) close to Zero V.

The exact strain (applied bias) dependence of $\frac{\Delta\rho_\parallel}{\rho_\parallel}$ evolves as a function of temperature and the asymmetry in the data changes as well. To separate out the symmetric as well as the asymmetric part of $\frac{\Delta\rho_\parallel}{\rho_\parallel}$ we use the following definition :

$$\frac{\Delta\rho_\parallel^S}{\rho_\parallel}(V) = \frac{1}{2}\{\frac{\Delta\rho_\parallel}{\rho_\parallel}(V^+) + \frac{\Delta\rho^\parallel}{\rho_\parallel}(V^-)\} \tag{8}$$

$$\frac{\Delta\rho_\parallel^A}{\rho_\parallel}(V) = \{\frac{\Delta\rho_\parallel}{\rho_\parallel}(V^+) - \frac{\Delta\rho^\parallel}{\rho_\parallel}(V^-)\} \tag{9}$$

The superscript S and A refer to the symmetric and asymmetric parts respectively and the superscript + and - refer to the positive bias and negative bias respectively. A plot of $\frac{\Delta\rho_\parallel^S}{\rho_\parallel}(V)$ and $\frac{\Delta\rho_\parallel^A}{\rho_\parallel}(V)$ for different T from 300K down to 9K are shown in Fig. 5.5 (a) and (b).

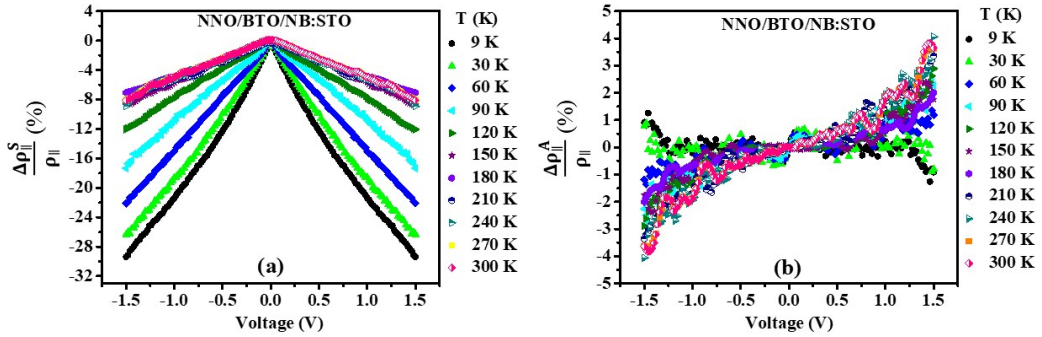

Figure 5.5. The varition of (a) $\frac{\Delta\rho_{\parallel}^{S}}{\rho_{\parallel}}(V)$ and (b) $\frac{\Delta\rho_{\parallel}^{A}}{\rho_{\parallel}}(V)$ with applied bias voltage for all the temperature for NNO/BTO/NB:STO sample

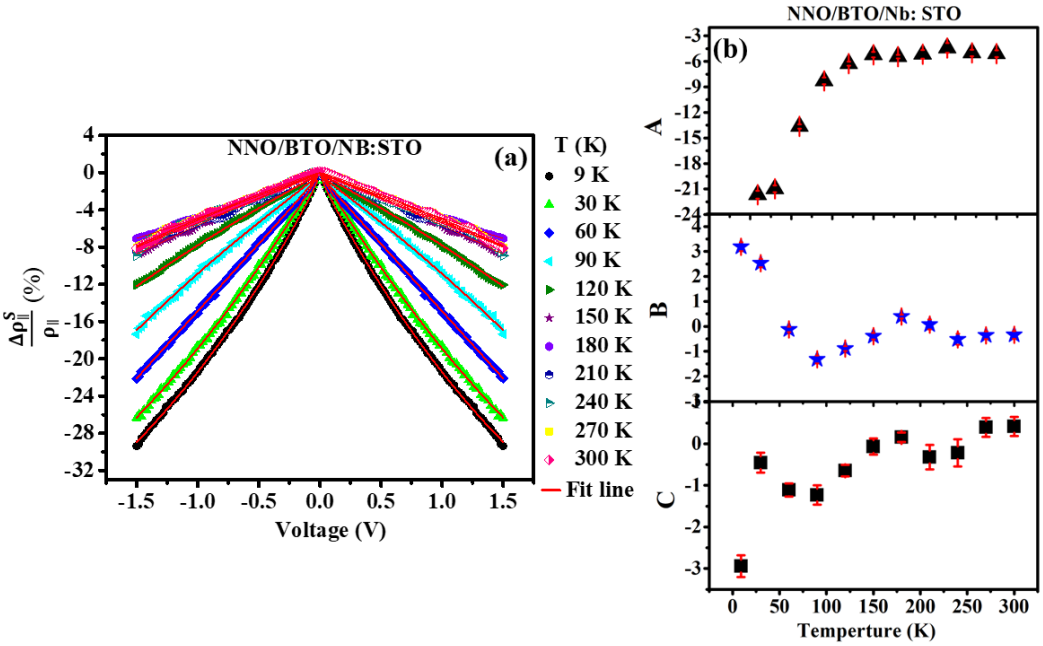

Figure 5.6. (a) The relative resistivity (symmetric) $\frac{\Delta\rho_S}{\rho}(V)$ and fitting with the Eqn. (10) for all the temperature for $NNO/BTO/Nb:STO$ (b) The evolution of fitted parameters A, B, C with temperature

The symmetric part of the change is much larger than the asymmetric part. This asymmetry is related to the asymmetry in straining in the substrate as shown in Table 2. We find that the symmetric part $\frac{\Delta\rho_{\parallel}^{S}}{\rho_{\parallel}}(V)$ is non-linear and the bias (and hence the strain dependence) evolves with temperature. From observation of the shape of the curve we used

the following empirical relation to fit the data and find that an excellent fit can be obtained :

$$\frac{\Delta\rho_{\parallel}^{S}}{\rho_{\parallel}}(V,T) = A(T)|V| + B(T)V^2 + C(T)|V|^{\frac{1}{2}} \tag{10}$$

The temperature dependent variation is quantified through temperature dependent coefficients A(T),B(T) and C(T). The temperature variation are shown in Fig. 5.6. The large temperature dependence indeed arises from linear term where the coefficient A shows a large change in its value for $T < 100$K. Similar changes although small are seen for the other two coefficients.

5.6 Temperature dependent resistivity data

The temperature driven transport measurement has been carried out with several bias voltage to study the straining effect on M-I phase transition with the multilayered sample. In Fig. 5.7 the temperature evolution of resistivity and (inset: conductivity ($= \frac{1}{resistivity}$)) is shown for several bi-polar bias voltages where diffused or broad type M-I transition observed from insulator to bad metallic phase.

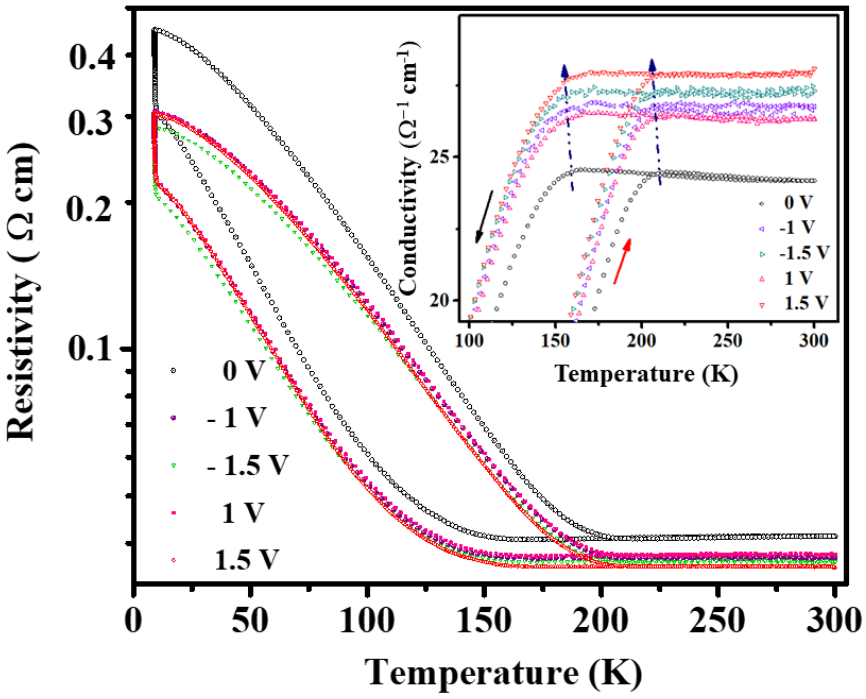

Figure 5.7. Temperature dependence of the in-plane Resistivity for NNO/BTO/NB: STO multilayer for zero and several bi-polar bias voltages. Inset: Zoom view of Conductivity vs T close to the transition regions showing the shifting of T_{MI} with bias voltages.

The zero bias conductivity data close to the tarnsition region shows that metallic phase signature is abolishing gradually with applied bipolar bias voltages. With the application of bias, the transition becomes broader or diffused. The conductivity value has been increased with the bi-polar biases throughout the temperature range. The sufficient tuning of transition temperature (T_{MI}) due to straining effect has been observed. We have used two positive and two negative biases i.e., -1.5 V, -1 V, 0 V, 1 V, 1.5 V for these experiments. The time dependent resistivity observed at lowest T at isothermal annealing. This is signature of supercooling metallic state below T_{MI} where the metastable metallic state exists in insulating phase matrix as discussed in Chapter-4 before.

The shif of transition temperature (T_{MI}) with the bias voltage has been shown in zoom view of the transition region in fig 5.7 (inset). The left shift of T_{MI} value with increase of bias voltage is observed which indicates the appearance of in plane compressive strain due to piezo bias that stabilizes the high tempertaure metallic phase. In the hysteresis curve , the T_{MI} shifted towards lower T for both the heating and heating cycle.

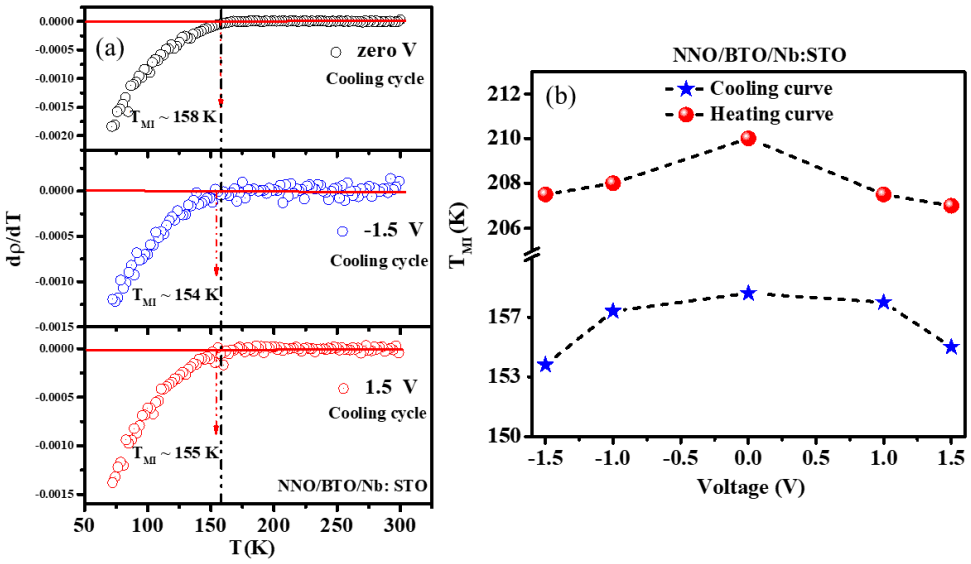

Figure 5.8. (a) The variation of $\frac{d\rho}{dT}$ with temperature for NNO/BTO/NB: STO multilayer for zero and ± 1.5 V. (b) The shifting of T_{MI} with bias for heating and cooling cycle.

The quantitative change in the value of T_{MI} at several bias voltage has been estimated by comparions of conductivity data taken at different applied bias. The temperature derivative of resistivity i.e., $\frac{d\rho}{dT}$ has been calculated from the raw data of resistivity for each set of bias voltage and plotted with temperature(T) in Fig 5.8(a). The variation of resistivity derivative has a clear slope change near the transition region. The slope-change-point shifting is indicated with a red arrow on the biased $\frac{d\rho}{dT}$ with zero biased data. The individual transition temperature is identified from the variation of $\frac{d\rho}{dT}$ and plotted with the bias voltage in Fig

5.8 (b). The T_{MI} is shifted to 154 K (for -1.5 V) and 155 K (for +1.5 V) from 158K (Zero V) with an average shift of ≈ 2.5 K.

5.7 Discussion

5.7.1 Evolution of $\frac{\Delta\rho_{\parallel}^{S}}{\rho_{\parallel}}(V)$ with T

The temperature evolution of $\frac{\Delta\rho_{\parallel}^{S}}{\rho_{\parallel}}(V)$ with T has been shown in Fig. 5.9 for $NNO/BTO/Nb:STO$. The lowest value of $\frac{\Delta\rho}{\rho}$ has been observed at the M-I transition borderline which gradually increases on cooling and heating accordingly. The presence of high T metallic and low T insulating phases causes the tuning of resistivity to be at its lowest near the transition boundary. When the temperature is low, monoclinic crystal symmetry is shown to exist in NNO, where the Ni-O bond is tuned and the Ni-O-Ni angle decreases, reducing the overlap between the Ni 3d and O 2p bands. The system behaves as an insulator and aids in localising the electronic wave-function which enhances polarization.On the other habnd, the rhombohedral symmetry of BTO takes hold in the low T region below ≈ 190K, providing significant ferro- and piezo-electricity that transmit onto the top NNO layer which have an impact on lowering the in-plane resistivity. It is a fresh experiment to look at how these temperature-driven structural changes in BTO layer affect the physical characteristics of the strained NNO film grown on BTO.

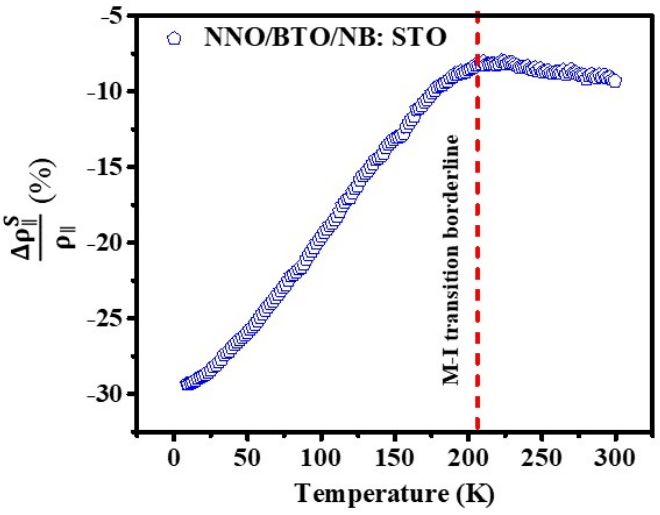

Figure 5.9. The variation of $\frac{\Delta\rho_{\parallel}^{S}}{\rho_{\parallel}}(V)$ with T obtained from bias dependent hysteresis Fig. 5.7 for NNO/BTO/NB: STO multilayer showing the T_{MI} borderline.

The in-plane resistivity tuning of NNO is at its smallest near and about T_{MI}, which has seen $\approx$ 2.5 K shifted towards lower T at $\pm$ 1.5 V for both heating and cooling cycles.

5.8 Conclusion

In summary, we successfully grew high-quality $NdNiO_3$ (NNO) thin films on BTO (001) single crystalline substrate and on pre-deposited BTO/Nb: STO (001) film. The samples were characterized using XRD, SEM, AFM techniques. The electrical transport characteristics of NNO films were modified by the field-controlled piezoelectric strain which is induced and transported by the opposite piezoelectric effect of BTO-SC and as grown BTO layer. The metal-insulator transition temperature in NNO has been interestingly reduced by $\approx$ 3K in response to 0.04% in-plane compressive strain in NNO in multilayer, indicating effective M-I modulation with application on mild biasing $\pm$ 1.5 V.

References

[1] C. Thiele, K. Dörr, O. Bilani, J. Rödel, and L. Schultz, Phys. Rev. B, 75, 054408 (2007)

[2] R. K. Zheng, J. Wang, X. Y. Zhou, Y. Wang, H. L. W. Chan, and C. L. Choy J. Appl. phys. 99, 123714 (2006)

[3] R. K. Zheng, Y. Wang, H. L. Chan, C. L. Choy, and H. S. Luo Journal of Appl Phys lett. 92, 082908 (2008).

[4] R. K.Zheng, H.U. Habermeier, H. L. W. Chan, C. L. Choy, and H. S. Luo, Phys. Rev. B, 81 104427 (2010)

[5] M. Zheng and R.K. Zheng, Phys. Rev. Applied.5, 044002 (2016).

[6] S. Heo, C. Oh, M. J. Eom, J. S. Kim, J. Ryu, J. Son and H. M. Jang, Sci Rep, 6, 22228 (2016).

[7] J.M. Yan, M. Xu, T.W. Chen, M.M. Yang, F. Liu, H. Wang, L. Guo, Z.X Xu, F. Y. Fan, G.Y. Gao, et al. Phys. Rev. Applied 11, 034037 (2019)

[8] L.Chen, X.K Ning, C. D. Reng, M.J, Phys.Lett A (2018).

[9] A. D. Rata, A. Herklotz, K. Nenkov, L. Schultz,and K. Dorr Phys. Rev.Lett. 100, 076401 (2008)

[10] P. Majhi, S. Chatterjee, R.S Bisht, R. Reddy. B. Ghosh, A.K. Raychaudhury, Phys. Rev. Materials 5, 085005 (2021)

[11] S. Sengupta, A. Ghatak, and A. K. Raychaudhuri, J. Phys.: Condens. Matter 33 465702 (2021)

.

Chapter 6

Conclusion and future directions

In this thesis, we have investigated the structure and physical properties of $NdNiO_3$ thin films and multilayers which shows temperature driven metal-Mott insulator transition. The occurrence of phase-coexistence around the M-I transition and the associated physics have been studied in NNO. The thesis deals with phenomena of phase co-existence of two phases namely high T metallic and low T insulating phase of NNO thin film which shows T driven M-I transition. The phase co-existence has an important consequence, in particular, when dynamic aspects and kinetics of co-existing phases are considered around T_{MI}.The major observations of the thesis are described as-

I In the presence of adequate crystal disorder, we have explored the NNO phase transition area. A new observation namely 'electronic Griffiths' like phase has been found near and above the metal-Mott insulator boundary in $NNO/BTO/STO$ multilayer which is a quenched disordered system.

II We looked at how the texture of NNO films with different grain sizes affected the consequences of carrier kinetics in low T supercooled metallic zones.The investigation of resistivity relaxation kinetics below T_{MI} (in supercooling regime) is carried out to study the phase conversion phenomena and the related things in the films of NNO having various grain size.

III We have used substrate induced strain generated by suitable piezo-substrate to tune the in-plane resistivity and T_{MI} in NNO. The in-plane resistivity and T_{MI} of single and bilayered based NNO film has been tuned using voltage controlled reversible strain.

6.1 Future directions

1. It is interested in comprehending how substrate orientation affects M-I phase coexistence and how it affects the para to antiferromagnetic transition (Neel transitionm, T_N) from the standpoint of phase transition order. We would like to understand the nature

of phase coexistence at the tri-critical point. Coexistence of the electrical and magnetic phases

2. Can the magnetic Griffiths phase exist in disordered NNO system like $NNO/BTO/STO$ along with the electronic Griffiths phase?

3. Additional theoretical investigations are required to comprehend phase coexistence in various doped and undoped $RNiO_3$ thin film samples.

Appendix 1 : Synthesis, characterization and transport measurement of $CaPd_3O_4$ material

Calcium palladates ($CaPd_3O_4$), a non-perovskite cubic $NaPt_3O_4$ type oxide material, has been synthesized using standard solid-state method. The crystallinity and structural analysis of $CaPd_3O_4$ was successfully observed in Xray diffraction pattern and Transmission Electron Microscopy (TEM) images which is further tested with Rietveld refinement technique. We did Raman spectroscopy measurement of $CaPd_3O_4$ which reveals the prominent peaks as active vibrational modes present in the system. Further we did low temperature transport measurement with $CaPd_3O_4$ sample.

1.1 Sample growth

We use standard solid state method to grow the $CaPd_3O_4$ and Li doped $CaPd_3O_4$ material. The precursor $CaCO_3$ and PdO are taken in stoichiometric amount. Then the $CaCO_3$ and PdO are ground separately and mix each other and grind again. Mixing of NaCl in ratio 2:1 and Grind. The NaCl acts as a kind of flux. It is effective to decrease the sintering temperature without reducing PdO. In next step, the mixture is Heated at 600^oC for 24 hrs. with halting 2 hours at 450^oC. The NaCl has been rinsed out from the mixture by using hot DI water and centrifuging. Next step, ground the powder and make a pellet.As a final step Heated the pellet at 750^oC for 24 hrs. with halting 2 hrs. at 450oC to get proper stoichimetry.

1.2 Characterization

The bulk sample has been characterized with the Thermo-gravimetric Analysis (TGA), X-ray Difraction (XRD)„ Scaning Electron Microscope (SEM), Transmission Electron Microscope(TEM) and Raman spectroscopy.The data are given in Fig. A1(a-d). The XRD data has been further fitted with Rietveld refinement technique to get the crystalline parameters which are enlisted in table -1 and 2.The SEM and TEM data is given in Fig. A2.

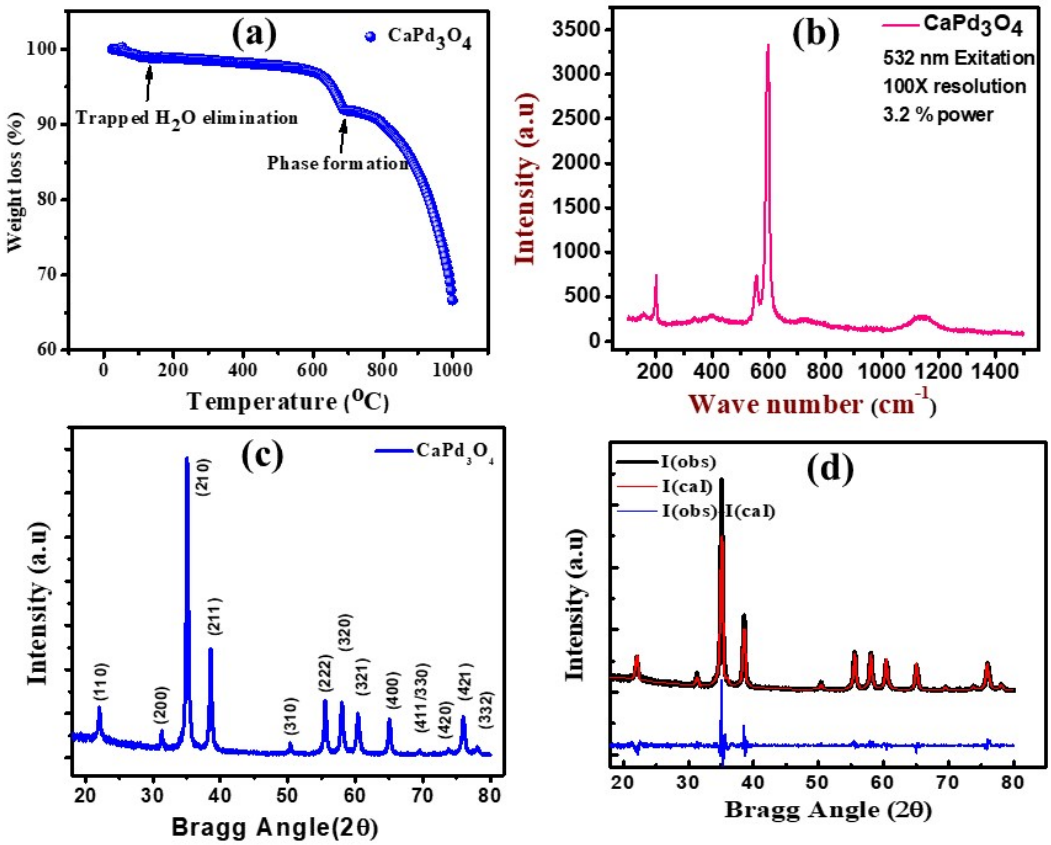

Figure A1. (a) TGA data: Weight loss vs Temperature showing the stoichimetric phase formation temperature. (b) The Raman spectroscopy showing the characteristic peaks which represents the vibrational mode (c) XRd data: Intensity vs Bragg angle imply the proper phase formation (d) The XRD data with fitted line and residual line by Rietveld Refinement

Table 1. Parameter details of Rietveld Refinement

Atom	N type	X	Y	Z	B	OCC	Nor. site OCC(%)
Ca	Ca	0	0	0	0.0649 (6)	0.12922	100
Pd	Pd	0.25	0	0.5	0.0221 (2)	0.38003	102.02
O	O	0.25	0.25	0.25	0.0805 (4)	0.52733	98.03

Table 2. Lattice constant and other parameters

a(Å)	b(Å)	c(Å)	$\alpha = \beta = \gamma = 90^o$	χ^2	R_{wp}	R_{exp}	R_p
5.771	5.771	5.771	90	3.34	13.96	25.5	26.5

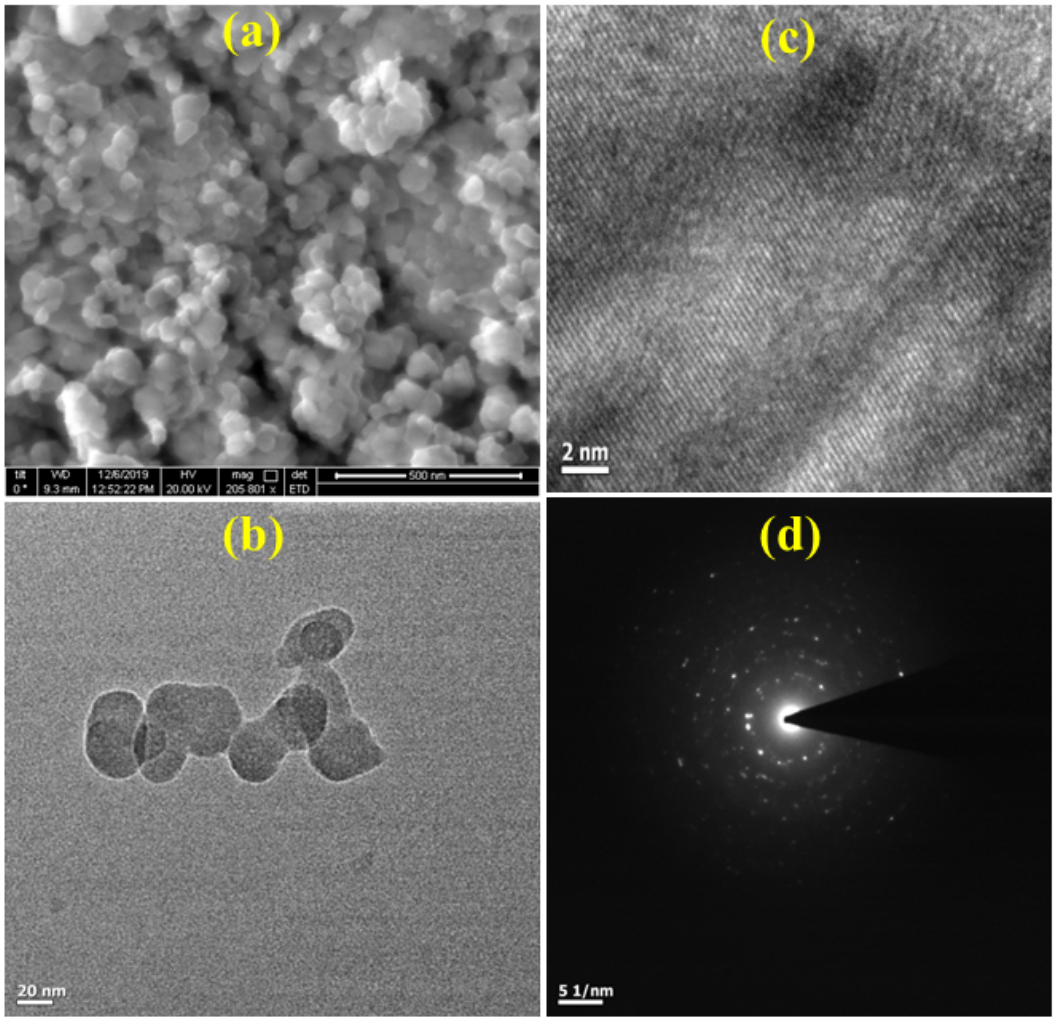

Figure A2. (a) SEM image of the morphology of CPO pellet (b)TEM image of CPO grain in 20 nm resolution (c) Fringe patter showing the high crystallinity in 2 nm resolution. (d) The SAED pattern showing the polycrystalline nature of CPO powder

1.3 Shifting of photoluminancence (PL) peak in varying exitation wavelength

The exclusive photoluminacence (PL) spectroscopy measurement have been carried with the CPO material in bulk form (pellet with diameter 7 mm , thickness $\approx$ 1.5 mm) and observed the nature of PL peak shifting with excitation wavelength (Fig. A3)

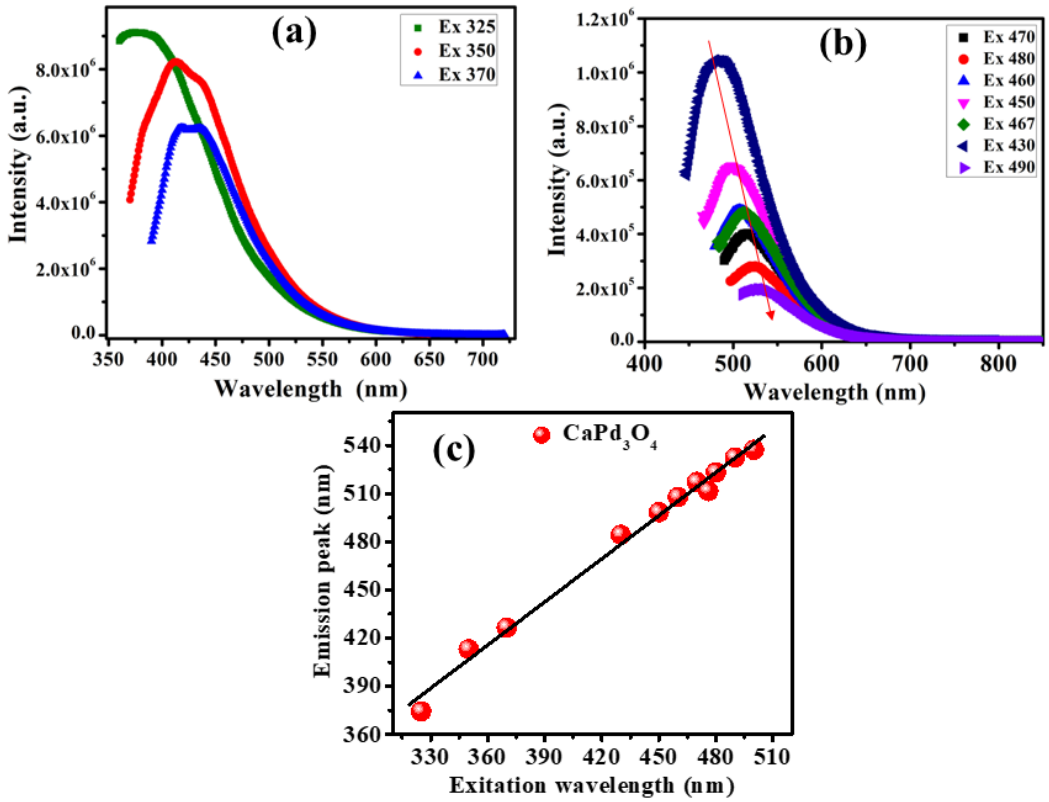

Figure A3. (a) PL intensity vs exitation wavelength for lower wavelength (b)PL intensity vs exitation wavelength for the wavelength 470nm to 490 nm showing right shift of the peak. (c) The evolution of PL peak position with Exitation wavelength varying with a straight line.

1.4 Low temperature transport measurement

In Fig. A4, (a) The conductivity data has been plotted with temperature in the range 3 to 300K.The data at lower temperatures can be fitted Fig. A4 (b) by the thermal-activation process expressed by Arrhenius plot -

$$\rho = \rho_0 exp \frac{E_g}{k_B T} \tag{1}$$

where, ρ_0, E_g, and k_B are the pre-exponential factor, activation energy, and Boltzmann constant, respectively. The $E_g = 1.39meV$ was obtained at $\approx$ 28K.

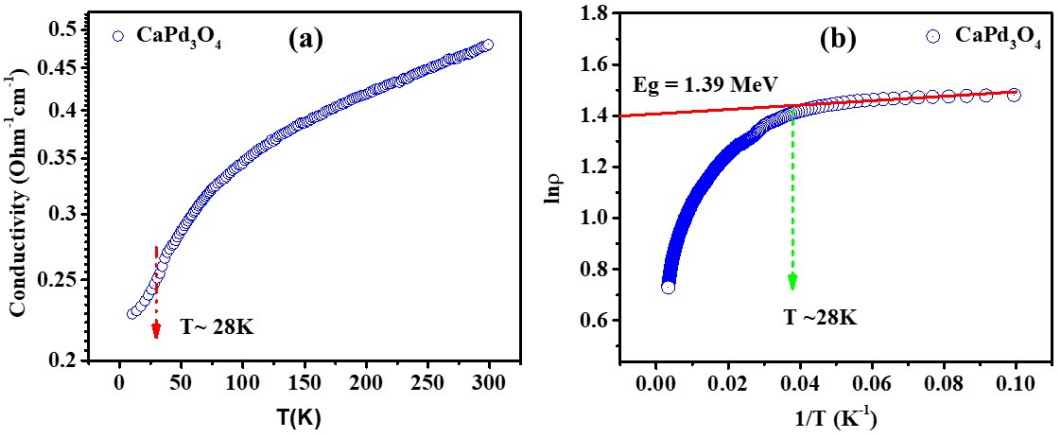

Figure A4. (a) The variation of Conductivity with temperature in the range 3 K to 300 K (b) The variation of ln ρ with 1/T showing the activation energy 1.39 MeV at $\approx$ 28 K

Appendix 2: LabView master code for time, temperature and voltage dependent resistance measurement

For this dissertation, we have developed two LabView program to operate the instruments in automatic mode via computer. We have developed the code in NI instruments, LabView Home and student edition which is subscribed by our centre.

2.1 LabView code for temperature dependent resistivity measurement

We have developed the code for temperature dependent resistivity measurement by interfacing major two instruments; SR-865A (4MHz lock in amplifier) and Lake shore-335 temperature controller. The front panel and block diagram are given in Fig. B1 and B2 below.

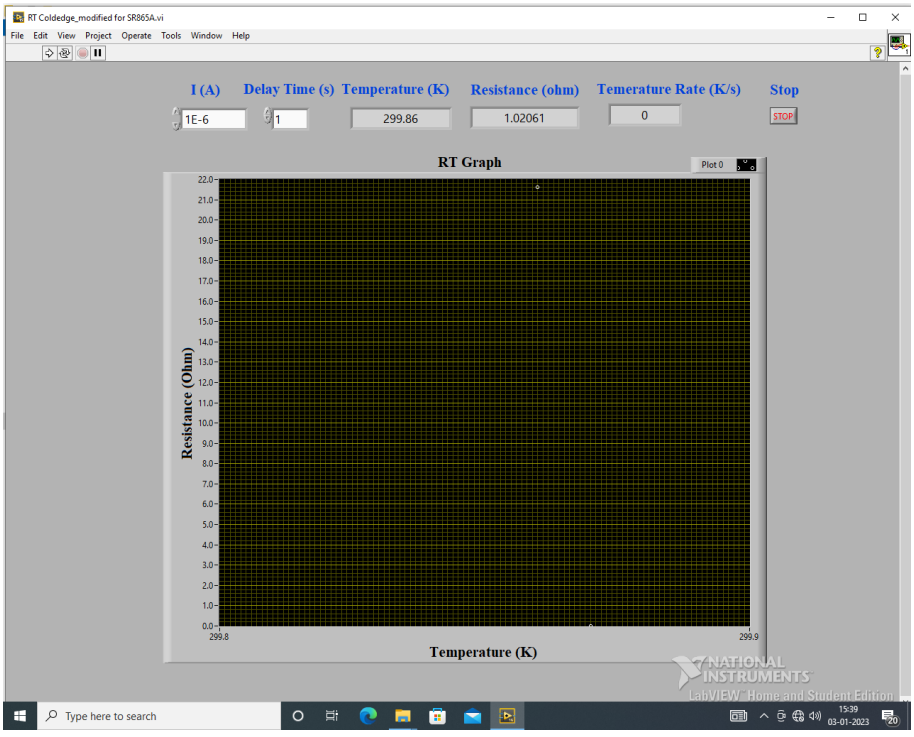

Figure B1. The front panel of code showing graph

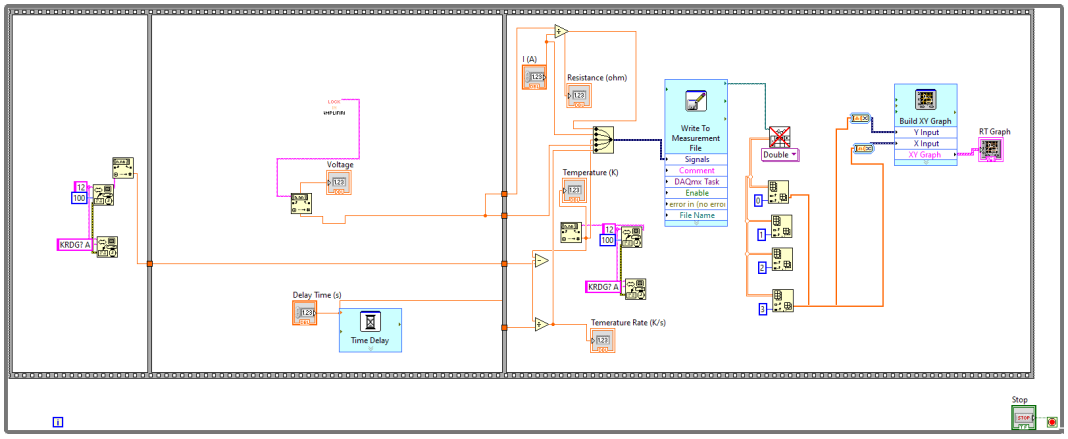

Figure B2. The complete block diagram of the code.

2.2 LabView code for voltage dependent resistivity measurement

This code has been written to control Sourcemeter (SM-Kethley 2410) and Lock-in amplifier (SR-865A) simultaneously at variously temperature. The SM has been used to apply the DC biasing in fully control manner using the code. In front panel, we can input the initial and final voltage, voltage step, current and voltage range, wait time, measure interval for better control the SM. The in-plane current has to be put to get the in-plane resistance from SR-865A with the out of plane biasing by SM-2410. A few steps of the block diagram are displayed in Fig. B3, B4, B5 below.

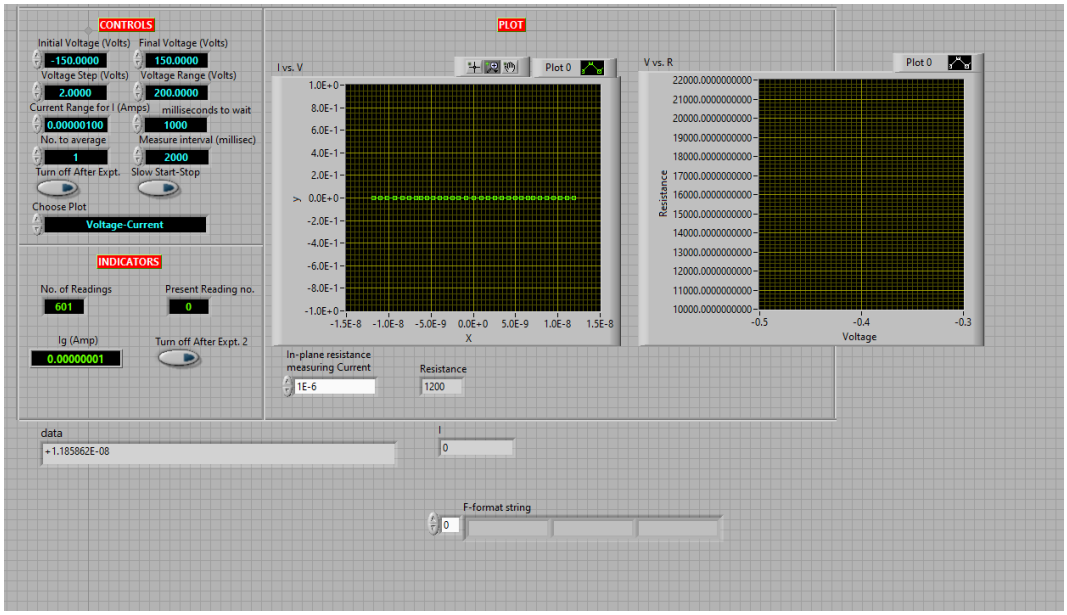

Figure B3. The front panel of code showing graph

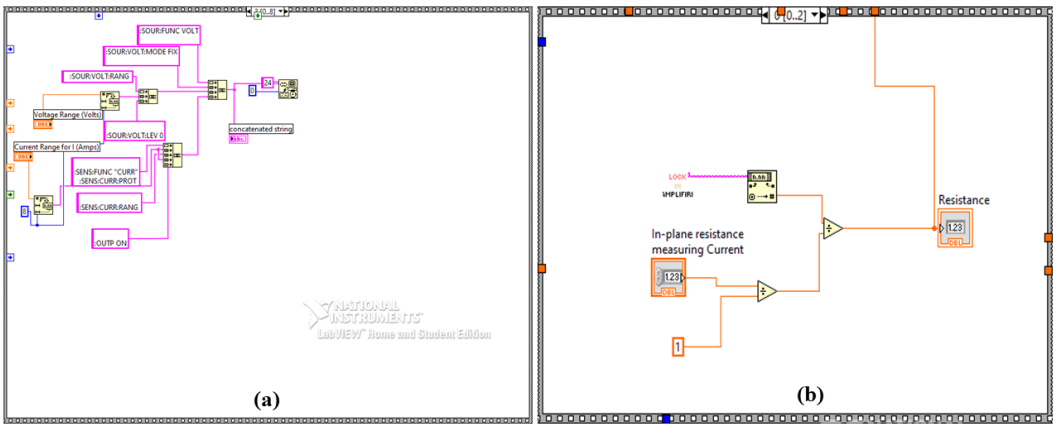

Figure B4. (a) The flat sequence structure in while loop showing all the required commands along with the primary address 24 for SM 2410. (b) flat sequence structure in While loop showing the lock-in amplifier (SR-865A) sub-VI insertion with primary address, proper commands for voltage value read, write, and print

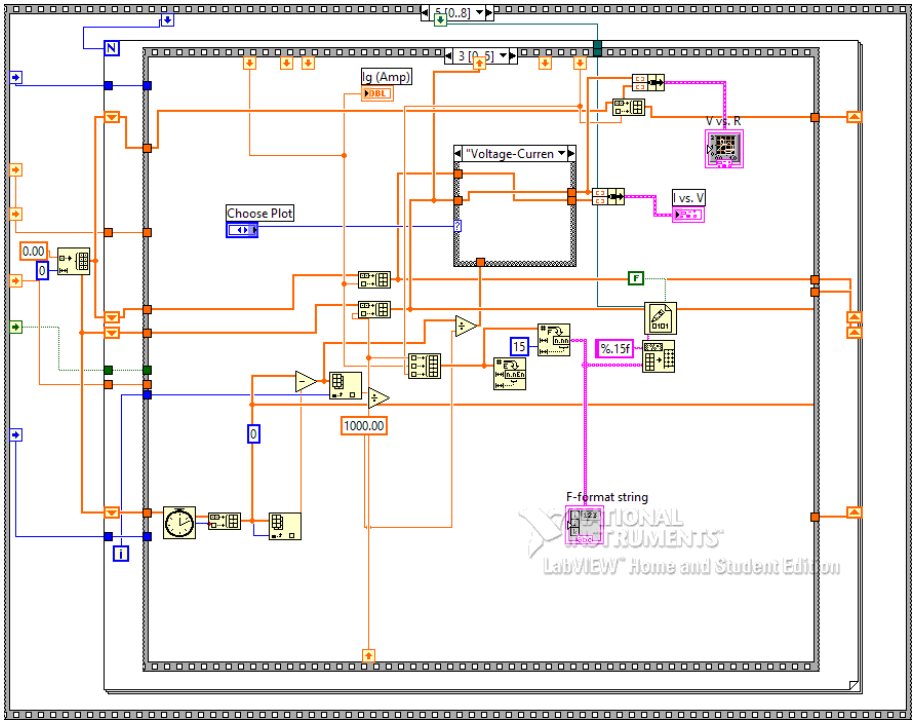

Figure B5. The flat sequence structure of the code showing the two final graph builder icon name V vs R and I vs V.

Appendix 3 : Low temperature transport and bias dependent resistivity tuning of $NNO/STO/PMN-PT$

We have carried out the low temperature transport measurement with PLD grown $NNO/STO/PMN-PT$ bilayer film in collinear four probe configuration down to liquid N_2 temperature with homemade set-up. Here the STO used as a $\approx 5nm$ buffer layer to reduce the lattice mismatch between NNO and PMN-PT. The highly oriented growth of both NNO and STO is observed in XRD and RSM measurement. The detail characterization of the film has been discussed in Chapter-2. In Fig. C1(a). The low T electrical transport data is plotted with function of T for both heating and cooling cycle. The inset of Fig.C1(a) represent the variation of $\frac{d\rho}{dT}$ as a function of T which show the M-I transition temperature at 165K and 179K for cooling and heating cycle respectively.

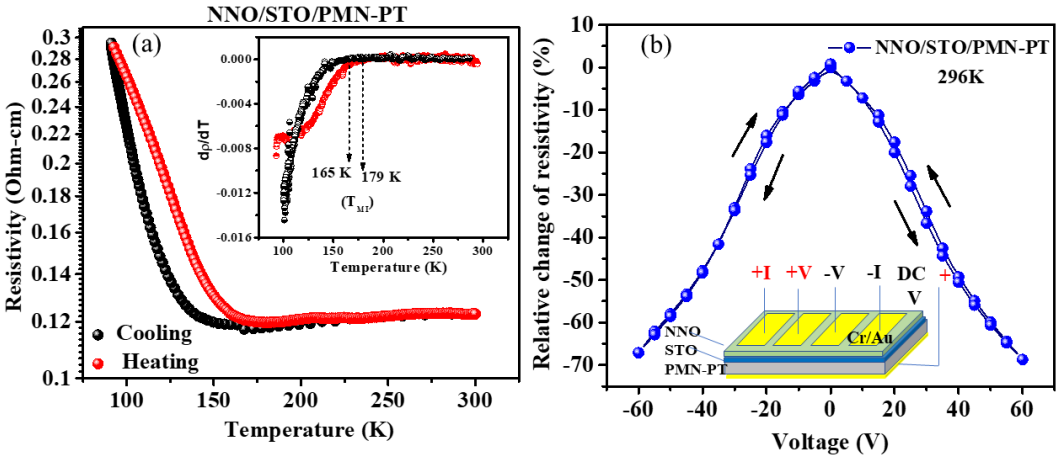

Figure C1. (a) Resistivity data down to liquid N_2 temperature Inset: $\frac{d\rho}{dT}$ as a function of T showing the M-I transition for heating and cooling cycle. (b) The relative resistivity tuning with applied bias voltage for $NNO/STO/PMN-PT$.Inset: The schematic diagram of film with circuit connection.

The resistivity tuning in application of bipolar piezo voltage has been observed in the $NNO/STO/PMN-PT$ film. The schematic diagram of the film with circuit connection has been depicted in inset of Fig. C1(b). The relative resistivity tuning response is bipolar. The maximum recorded tuning in planar resistivity is $\approx 70\%$ at $\pm$ 60V.